A General Purpose Large-Eddy Simulation/Probability Density Function Simulator on Block Structured Grids

by

Hasret Türkeri

A Dissertation Submitted to the
Graduate School of Sciences and Engineering
in Partial Fulfillment of the Requirements for
the Degree of

Doctor of Philosophy

in

Mechanical Engineering

KOÇ
UNIVERSITY

January, 2017

A General Purpose Large-Eddy Simulation/Probability Density Function Simulator on Block Structured Grids

Koç University

Graduate School of Sciences and Engineering

This is to certify that I have examined this copy of a doctoral dissertation by

Hasret Türkeri

and have found that it is complete and satisfactory in all respects,
and that any and all revisions required by the final
examining committee have been made.

Committee Members:

_____

Prof. Dr. Metin Muradoğlu

_____

Assoc. Prof. Dr. Mehmet Şahin

_____

Assist. Prof. Dr. Arif Karabeyoğlu

_____

Prof. Dr. İ. Bedii Özdemir

_____

Assist. Prof. Dr. Ayşe Gül Güngör

Date: _____

To my wife Sumeyye

and to our son Ahmet Hamza

ABSTRACT

A general-purpose large-eddy simulation (LES)/probability density function (PDF) methodology is developed for simulations of turbulent reacting flows. The LES/PDF solver is a hybrid solution methodology consisting of (i) a finite volume (FV) method for solving the filtered mass and momentum equations (LES solver), and (ii) the Lagrangian Monte Carlo based particle algorithm (PDF solver) for solving the modeled transport equation of the filtered joint PDF of compositions. Both the LES and PDF methods are developed and combined to form a hybrid LES/PDF simulator within the OpenFOAM framework. The in situ adaptive tabulation (ISAT) method developed by Pope [1] is incorporated into the new LES/PDF solver for efficient computations of combustion chemistry with detailed reaction kinetics. The method is designed to utilize a block structured mesh and can be readily extendible for the block unstructured grids. The three-stage velocity correction method of Zhang and Haworth [2] is also incorporated into the hybrid algorithm to interpolate the LES velocity field onto particle locations accurately and to enforce the consistency between the LES and PDF solvers at the numerical solution level. The hybrid algorithm is also fully parallelized using the conventional domain decomposition approach.

First, the consistency of the FV-LES solver and the Lagrangian-PDF solver is examined by using the one-way coupling methodology developed by Wang and Pope [3]. It is found that the LES and the PDF solvers exhibit very good consistency at the numerical solution level demonstrating accurate coupling of the LES and PDF algorithms. Then the performance of the three-stage velocity correction algorithm is investigated to determine effects of each stage on the consistency of the LES and PDF solvers and the computational cost required by each stage. The correction algorithm is found to be very effective in enforcing the consistency conditions at the numerical

solution level and first two stages are usually sufficient for simple reacting flows while the third stage is needed in the case of more complex flows involving recirculation regions. The predictive capability of the LES/PDF solver with the detailed chemistry representation is then examined by simulating a turbulent piloted methane/air jet diffusion flame (Sandia Flame-D). An augmented reduced mechanism (ARM1) [4] is used for the description of methane/air combustion. The results are found to be in very good agreement with the experimental measurements as well as with the earlier LES/PDF simulations. Finally, the new LES/PDF solver is applied to study a turbulent premixed flame from the Cambridge turbulent stratified flame series [5]. The results are found to be in reasonably good agreement with the experimental data.

ÖZET

Bu doktora tezinde, türbülanslı alevlerin sayısal modellenmesi için genel amaçlı büyük çalkantı simülasyonu (Large Eddy Simulation-LES)/olasılık yoğunluk fonksiyonu (Probability Density Function-PDF) simülatörü geliştirilmiştir. LES/PDF çözücüsü hibrit bir çözüm yöntemidir. Bu yöntemde, filtre edilmiş kütle ve momentum korunumu denklemlerinin çözümü için sonlu hacimler yöntemi (LES çözücüsü) kullanılmıştır. Türbülans-yanma etkileşimleri kimyasal bileşenlerin birleşik olasılık yoğunluk fonksiyonu yöntemiyle modellenmiş ve model denklemlerinin sayısal çözümü için Lagrangian Monte Carlo tabanlı bir partikül algoritması (PDF çözücüsü) kullanılmıştır. LES ve PDF çözücülerinin her ikisi de açık kaynaklı OpenFOAM yazılım paketi içerisinde geliştirilmiş ve pakete tümüyle entegre edilmiştir. Detaylı kimyasal yanma hesaplamalarının etkin bir şekilde yapılabilmesi için tablolama (the in situ adaptive tabulation (ISAT)) metodu yeni LES/PDF çözücüsü ile birleştirilmiştir. Bu çalışmada geliştirilen hibrit yöntem yapısal olmayan çözüm ağları esas alınarak geliştirilmiş ama bütün hesaplamalar blok-yapılı (block-structured) çözüm ağlarında yapılmıştır. Sayısal yöntem yapısal olmayan çözüm ağlarına kolaylıkla adapte edilebilir formdadır. Zhang ve Haworth (2004) tarafından geliştirilen üç aşamalı hız düzeltme algoritması mevcut LES/PDF yöntemine eklenmiş ve performansı gerçekçi türbülanslı alevlere uygulanarak gösterilmiştir. Yeni LES/PDF çözücüsü ayrıca geleneksel alt bölgeye ayırma (domain decomposition) yöntemi kullanılarak paralelleştirilmiştir. LES ve PDF çözücüleri arasındaki tutarlılık Wang ve Pope (2011) tarafından geliştirilen tek-yönlü birleştirme yöntemi kullanılarak test edilmiştir. Mevcut LES ve PDF çözücülerinin sayısal çözüm seviyesinde çok tutarlı sonuçlar verdiği gösterilmiştir. Bu LES ve PDF çözücülerinin doğru olarak birleştirildiklerine delalet etmektedir. Daha sonrasında ise, üç aşamalı hız düzeltme algoritmasının her bir aşaması, LES ve PDF

çözücülerinin tutarlılıkları üzerindeki etkilerini belirlemek ve hesaplama maliyetini tespit etmek için incelenmiştir. Düzeltme metodu sayısal çözüm seviyesinde tutarlılığın sağlanması açısından çok faydalı bulunmuştur. İlk iki aşama basit türbülans alevleri için yeterli olmakla birlikte özellikle geri çevrimli ve karmaşık yapılı akış durumlarında üçüncü aşama düzeltmeye ihtiyaç duyulduğu tespit edilmiştir. Daha sonrasında ise, yeni hibrit LES/PDF çözücüsü bir detaylı kimyasal kinetik model kullanılarak pilotlu bir jet difüzyon türbülanslı alevine (Sandia Flame-D) uygulanmıştır. Metan/hava yanması indirgenmiş bir kimyasal mekanizma (ARM1) ile temsil edilmiştir. Sonuçların deneysel veriler ve daha önceki LES/PDF simülasyon sonuçları ile çok uyumlu oldukları gösterilmiştir. Son olarak, yeni LES/PDF çözücüsü Cambridge seyrekleştirilmiş alev serisindeki ön-karışımlı türbülanslı bir aleve uygulanmıştır. Sonuçların deneysel sonuçlar ile makul seviyede uyumlu oldukları görülmüştür.

ACKNOWLEDGMENTS

First of all, I would like to thank my advisor Prof. Dr. Metin Muradoğlu for his guidance and support throughout my graduate study and during the completion of this thesis. Without his encouragement, knowledge and enthusiasm this thesis would have never be completed.

I am also grateful to Assoc. Prof. Dr. Mehmet Şahin, Assist. Prof. Dr. Arif Karabeyoğlu, Prof. Dr. İ. Bedii Özdemir and Assist. Prof. Dr. Ayşe Gül Güngör for participating in my thesis committee and for the critical reading of my thesis.

I would like to thank to Senol Piskin, Daulet Izbassarov, Beytullah Ozgur, Emel Kupcu and all my friends at Koc University. I particularly wish to thank Senol Piskin and Daulet Izbassarov for their friendship and also for the numerous enlightening discussions.

I would like to thank TUBITAK (Project no: 111M067 and 214M309) for providing scholarship during my PhD studies.

Last but not lest, special thanks go to my parents Hamdi and Imahan and my wife Sumeyye and my son Ahmet Hamza, my brothers Sabri and Sami, my sisters-in-law Sevil and Nazik, and their children Faruk, Elif, Kuzey Ata and Cemre Mina for their love and support throughout my life. Without their patience and support, I definitely could not be here.

TABLE OF CONTENTS

LIST OF TABLES

LIST OF FIGURES

Chapter 1

INTRODUCTION

More than 85% of the total energy production in the world still comes from burning fossil fuels, i.e., converting chemical energy stored in hydrocarbon fuels first into thermal energy and then into mechanical energy in energy conversion devices, e.g., gas turbines and reciprocating engines, and fossil-fuel power stations [11]. Nearly in all practical energy conversion devices combustion takes place in a turbulent environment mainly due to enhanced mixing [12]. Therefore understanding the fundamentals of the turbulent reacting flow is crucial for increasing the efficiency of the combustion devices, and decreasing the dangerous effects of combustion on the environment, e.g., formation of NO_x, soot, and unburnt hydrocarbons (HC), in addition to CO_2 that contributes to the global warming.

Experimental methods play a crucial and indispensable role in the investigation of turbulent combustion. The most advanced experimental methods are based on the optical diagnostics. However they suffer from the difficulties in measuring quantities in turbulent reacting flows due to limited optical access, soot, high temperature, etc., and high operating cost. On the other hand, the numerical investigations of turbulent reacting flows have proven to be a very effective and powerful technique in understanding the fundamentals of the turbulent combustion. The numerical methods are mainly based on the numerical solution of the conservation equations for mass, momentum, species mass fractions and energy. These equations provide a full description of the reacting flows. However, numerical solution of the conservation equations of turbulent reacting flows is notoriously difficult since the equations are highly non-linear and involve a wide range of length and time scales. Turbulent flows have different

sizes of motions (eddies). The range of eddy sizes mainly depends on the Reynolds number, Re, of the turbulent flow such that the ratio of the largest to the smallest eddies scales as $Re^{3/4}$ [12]. In direct numerical solution of the conservation equations without using any simplification (modeling), all the scales of a turbulent flow must be calculated explicitly, which demands a very high computational cost. Since number of floating-point operations required to complete a numerical simulation is typically proportional to number of spatial grid points and number of time steps, one can estimate that the number of operations grows as Re^3 [12]. Highly non-linear chemical reactions and their interactions with the turbulent flow add a further complexity to the problem and substantially increase the total computational cost. The method of solving the conservation equations directly is called the direct numerical simulation (DNS) method. Due to its high computational cost, the DNS method cannot be used in the practical engineering problems, thus it is restricted to the turbulent reacting flows with simple geometries and low Reynolds numbers.

In the most of the applications, predicting mean properties such as the mean reaction rates or the mean velocity is sufficient from the engineering point of view. Thus instead of resolving all the scales in a turbulent reacting flow, solving the equations only for the mean properties is usually preferred. The conservation equations for the mean properties are derived by taking an average of the instantaneous conservation equations. Thus the mean properties are obtained by solving the mean conservation equations. This class of methods is generally known as the Reynolds-averaged Navier-Stokes (RANS) methods. Since the RANS methods only calculate the mean properties, the computational cost is much lower than that in the DNS method. However, the averaging of the instantaneous conservation equations introduces new terms into the mean conservation equations, which cannot be generally expressed in terms of the mean properties, causing the well-known closure problem. In the RANS approach, the unclosed terms must be modelled. Various RANS models have been developed and widely used in the turbulent flow simulations but they are not always satisfactory. The practical combustion devices require rapid mixing of fuel and oxidizer and a short

combustion time, which leads to very complicated flow patterns, including swirling and recirculating regions. The RANS method is typically found to be insufficient to predict these complex flows. Additionally, since the RANS method only calculates the mean properties in turbulent reacting flows, it is typically not capable of predicting the instabilities and pollution formation in complex flows characterized by swirling and recirculating regions[13].

An advanced method that can predict the instabilities and pollution formation can be derived by filtering (instead of averaging) the instantaneous conservation equations. The solution of the filtered conservation equations gives the filtered (large scale) properties of turbulent reacting flows. This approach is known as the large-eddy simulation (LES) method. In the LES method, the turbulent flow is decomposed into large scale (resolved) motions and the small scale (unresolved) motions by a filtering operation. The large scale (energy containing and geometry dependent) motions are explicitly calculated whereas the small scale motions are assumed to be universal and geometry independent based on the Kolmogorov's hypothesis [14]. Filtering the instantaneous conservation equations also introduces unclosed terms in the filtered conservation equations as occurs in the RANS method and these unclosed terms need to be modelled. Thus both the RANS and the LES methods require modeling of the unclosed terms in the mean and the filtered conservation equations, respectively.

In the RANS method, the unclosed terms represent the entire turbulent motions. Therefore the turbulent motions are totally modelled in the RANS approach. On the other hand, in the LES method, the large-scales of the turbulent motions are explicitly calculated whereas the small-scales are modeled by the scale similarity assumption between the large and the small-scales. Thus, in the LES, instead of modeling all-scales as it is the case for the RANS method, only the small-scales which are assumed to have universal characteristics are modelled. The explicit solution of the large-scales has proven to make the LES method very successful in simulations of nonreacting turbulent flows [15, 16]. However, combustion requires fuel and oxidizer to be mixed at the molecular level, thus the chemical reactions take place entirely at the smallest

scales in the turbulent reacting flows. Consequently, the combustion does not have large-scales in the turbulent reacting flows, thus the scale-similarity assumption cannot be used for modeling the unclosed reaction terms [17]. Therefore, in the LES method the unclosed reaction terms have to be entirely modelled as in the RANS method [13]. Although the non-linear chemical reactions must be modelled in both the RANS and LES methods in a similar way, the LES potentially gives more accurate predictions than the RANS for the turbulent reacting flows than those given by the RANS method [13, 18, 19]. The primary reason is that the combustion is driven in great part by the rate of the mixing process largely driven by the large-scale turbulent motions and the large scale motions are explicitly resolved in the LES method. As a result, the predictive capability of the LES is expected to be better than that of the RANS method [13, 17].

To model the interactions between turbulence and chemistry, various models have been proposed in the literature [20, 21, 22, 23, 24]. According to Veynante and Vervisch [25], the models can be classified based on the three physical approaches: i) Geometric analysis, ii) turbulent mixing and iii) one-point statistics. The models from the geometric analysis approach consider the flame front as a geometric surface evolving with the underlying turbulent flow. Then the mean (or filtered) reaction rates are modelled based on the geometric feature of the flame front such as flame area. The geometric analysis approach typically assumes that the flame is thin compared to all other length scales in the turbulent reacting flow. The turbulent mixing-based models assume that the combustion is controlled by the mixing rate, thus they mainly focus on modelling the turbulent mixing rate usually in terms of the scalar dissipation rates. In this approach the combustion is assumed to be very fast, i.e., faster than any time scale in turbulent reacting flow. The geometric surface and the turbulent mixing-based approaches require strong assumption on time and length scales of the turbulent reacting flows. In the one-point statistics approach, the mean (or filtered) reaction rate can be obtained from the joint probability density function (PDF) of

the chemical compositions as

$$\overline{\dot{\omega}} = \int_{\boldsymbol{\psi}} \dot{\omega}\left(\boldsymbol{\psi}\right) P\left(\boldsymbol{\psi}\right) d\boldsymbol{\psi}, \tag{1.1}$$

where $\boldsymbol{\psi}$ is the sample-space variable of the chemical compositions (that will be explained in the next section) and $P\left(\boldsymbol{\psi}\right)$ is the joint probability density function of the chemical species. Typically, in a turbulent reacting flow, the joint probability density function varies from point to point and from time to time, thus it is a function of space and time. Once the probability density function (PDF) of the chemical compositions is known, the mean combustion rate can be evaluated without any assumption on both length and time scales. The transported probability density function (PDF) method evolves the joint-PDF of compositions in space and time according to a modelled transport equation. The PDF method can calculate the chemical reaction rates exactly without using any model, thus it has the ability of predicting the challenging processes such as local extinction and re-ignition [26, 27].

Initially, the PDF method was developed in the RANS context. In particular advanced velocity-frequency-composition joint PDF method has formed a complete model for turbulent reacting flows [28]. In the LES context, first proposed by Pope [24], the PDF method combines its superior features with the LES, which gives rise to the LES/PDF method. The LES/PDF method has been found to be highly effective in simulation of laboratory-scale flames [29, 30, 31, 32, 33]. The model equations of the LES/PDF method consist of the filtered mass and momentum equations, and the filtered transport equation for the joint-PDF of chemical species. The first two equations calculate the large-scale turbulent motions while modelling the effects of small-scale motions. The modelled transport equation for the joint-PDF of chemical compositions accounts for the evolution of the chemical species in both the physical and compositions spaces.

Special attention should be paid to the development of an efficient and accurate numerical algorithm for the solution of the LES/PDF model equations. Although the numerical solution of the filtered mass and momentum equations can be obtained by

the conventional methods such as finite volume or finite differences, the conventional numerical methods are not feasible to solve the joint-PDF transport equation due to its high dimensionality. The remaining alternative is the Monte Carlo method that has proven to be suitable for solving the high dimensional problems. The Monte Carlo based Lagrangian solution methods [9] are commonly used to solve the transport equation of joint-PDF. Therefore the preferred solution methodology for the LES/PDF model equations is a hybrid solver composed of an Eulerian finite volume (or difference) method for the filtered mass and momentum equations (referred as the LES solver), and a Monte Carlo based Lagrangian particle solver (referred as the PDF solver). The hybrid LES/PDF solver provides a complete numerical solution method for the LES/PDF model equations of the turbulent reacting flows.

In the Monte Carlo based Lagrangian solver (the PDF solver), the flow is represented by a large number of notional particles. Each particle evolves by a stochastic differential equation (SDE) in the physical space and an ordinary differential equation (ODE) in the composition space. The stochastic and ordinary differential equations are constructed such that the statistics obtained from the particles are identical to the statistics implied by the transport equation of the joint-PDF of compositions. In the finite volume method (the LES solver), the computational domain is decomposed into computational cells (Eulerian grid) and the numerical solutions are calculated at the cell centers. The hybrid nature of the LES/PDF solver results in some important numerical issues that need to be addressed. One of the most important issues is the consistency between the LES and PDF solvers, i.e., they should be initialized to be consistent with each other and the consistency should be preserved during the simulation. The other numerical issues include tracking the Lagrangian particles over the Eulerian grid, extracting the mean properties from the Lagrangian particles and interpolating the Eulerian fields onto the Lagrangian particle locations. The coupling of the Eulerian LES and Lagrangian PDF solvers constitutes an additional challenge for the numerical method.

In the literature various hybrid LES/PDF solvers have been developed for sim-

ulations of turbulent reacting flows. They have been mostly applied to laboratory scale turbulent flames with simple geometries [3, 30, 18, 34, 35]. The main reason is the limited capability of the existing LES/PDF solvers designed to work only on the structured Eulerian grids. Previously Ansari et al. [36] and Ankur [37] have addressed this issue and developed LES/PDF solvers that can employ unstructured grids and thus perform simulations in complex geometries. While the former one is developed within a commercial platform of ANSYS-FLUENT software, the latter is implemented by combining the LES solver in OpenFOAM [38] with an existing PDF solver written in FORTRAN.

In the present thesis, a new LES/PDF solver is developed in the OpenFOAM framework. The new solver uses block structured grids and can be readily extended to unstructured grids, and thus allows to perform LES/PDF simulations in complex geometries of practical interest. The method is designed to employ the most advanced physical models and numerical schemes available in the literature. Unlike the previous works we implement the new LES/PDF solver completely in the open-source and free platform of OpenFOAM. Additionally, the PDF and LES solvers are both built within OpenFOAM libraries, thus the same data structure can be used in both solvers, which makes the data transfer between them very efficient and flexible. The new solver is designed to have the capability of performing detailed chemistry simulations using the in situ adaptive tabulation (ISAT) method [1] . Another important contribution of the present work is the implementation and examination of the three stage velocity correction method [2] within the LES/PDF context using a block structured grid. The velocity correction method was initially developed for unsteady and steady RANS-PDF simulations, and then extended to the LES/PDF methods [39] but it has not been fully tested for the LES/PDF simulations of turbulent flames of practical importance. Celis and Silva [39] investigated the performance of the three stage velocity correction method in the LES/PDF context but they considered only a simple mixing layer flow and performed simulations only on a simple structured uniform Cartesian grid. Thus, the present thesis is the first study about the perfor-

mance of the method within the LES context using a complex block structured grid for the realistic turbulent flames. Here, we implement the three stage velocity correction within the new LES/PDF solver, and then examine the performance of each stage in terms of the mass consistency, accuracy and the computational cost. The open-source and free OpenFOAM framework [38] is prefered since it is widely used in both industry and academia, and includes a wide range of physical submodels.

In this thesis, the main contributions can be summarized as follows:

1. Development and validation of a new LES/PDF methodology entirely in the OpenFOAM framework.

2. Implementation and performance assessment of the three stage velocity correction algorithm.

3. Examination of the consistency between the LES and the PDF solvers.

4. Investigation of the predictive capability of the new LES/PDF solver with detailed chemistry representation for a piloted jet flame (Flame-D) and a bluff-body stabilized flame (Cambridge flame).

The rest of the thesis is organized as follows. In the next chapter, the governing equations of the reacting flows are briefly reviewed. The general characteristics of turbulent flows are explained in Chapter 3. In Chapter 4, the PDF modeling for the turbulent reacting flows is presented. In Chapter 5, the numerical methods used to solve the model equations of the LES/PDF method are discussed. In Chapter 6, the hybrid LES/PDF solver is applied to a methane/air jet diffusion flame and the performance of the new solver is demonstrated. In Chapter 7, the method is applied to a premixed turbulent flame from the Cambridge stratified turbulent flame series [5]. The conclusions and future directions are presented in Chapter 8.

Chapter 2

GOVERNING EQUATIONS

2.1 Conservation Equations

In a reacting flow, the principal variables are the density, ρ, the velocity, u_i, one variable for energy (e.g., enthalpy h) and the mass fractions Y_α for N chemical species. All the information about the reacting flows can be obtained by solving the conservation equations for the mass, momentum, energy and species mass fractions. The conservation equations are briefly decribed here for a Newtonian fluid. The flow is assumed to be incompressible, i.e., the density is independent of pressure. The equations are presented and solved in the conservative form as follows:

1. The conservation of mass:

$$\frac{\partial \rho}{\partial t} + \frac{\partial \rho u_i}{\partial x_i} = 0. \tag{2.1}$$

   As mentioned above, the flow is assumed to be incompressible so the density is solely determined by the compositions.

2. The conservation of momentum:

$$\frac{\partial \rho u_i}{\partial t} + \frac{\partial \rho u_i u_j}{\partial x_j} = -\frac{\partial p}{\partial x_i} + \frac{\partial \tau_{ij}}{\partial x_j} + \rho g_i, \tag{2.2}$$

   where the terms on the left-hand side represent the local rate of change and convection of momentum while the terms on the right-hand side are the pressure gradient, the molecular transport due to viscosity and the gravitational force,

respectively. In Eq. (2.2), τ_{ij} is the viscous stress tensor given by

$$\tau_{ij} = \mu \left(\frac{\partial u_i}{\partial x_j} + \frac{\partial u_j}{\partial x_i} \right) - \frac{2}{3} \mu \frac{\partial u_k}{\partial x_k} \delta_{ij}, \tag{2.3}$$

where μ is the coefficient of viscosity.

3. The conservation of species α:

$$\frac{\partial \rho Y_\alpha}{\partial t} + \frac{\partial \rho u_i Y_\alpha}{\partial x_i} = -\frac{\partial J_i^\alpha}{\partial x_i} + \dot{\omega}_\alpha, \ \alpha = 1, 2, ...N, \tag{2.4}$$

where Y_α is the mass fraction of the species α, and $\dot{\omega}_\alpha$ is the chemical source term representing the rate of production of species α by the chemical reactions. The term J_i^α on the right-hand side represents the diffusion flux modelled by the binary flux approximation as

$$J_i^\alpha = -\rho D_\alpha \frac{\partial Y_\alpha}{\partial x_i}, \tag{2.5}$$

where D_α is the mass diffusivity of species α. All the mass diffusivities D_α are usually assumed to be proportional to the thermal diffusivity D defined as

$$D = \frac{\lambda}{\rho c_p}. \tag{2.6}$$

where λ is the thermal conductivity and c_p is the heat capacity of the mixture at the constant pressure. The Lewis number is defined to be the ratio of the thermal diffusivity to the mass diffusivity of species α as

$$Le_\alpha = \frac{D}{D_\alpha}. \tag{2.7}$$

Assuming unity Lewis number for all the species provides significant simplifications in the conservation equations for species mass fraction and energy. By assuming unity Lewis number for all the species, the species mass conservation

equation simplifies to be

$$\frac{\partial \rho Y_\alpha}{\partial t} + \frac{\partial \rho u_j Y_\alpha}{\partial x_j} = \frac{\partial}{\partial x_j}\left(\rho D \frac{\partial Y_\alpha}{\partial x_j}\right) + \dot{\omega}_\alpha. \tag{2.8}$$

4. The conservation of energy: The energy conservation is usually expressed in terms of the enthalpy or temperature. In terms of enthalpy, it can be written as

$$\frac{\partial \rho h}{\partial t} + \frac{\partial \rho u_i h}{\partial x_i} = \frac{\partial p}{\partial t} + \frac{\partial u_i p}{\partial x_i} - \frac{\partial J_i^q}{\partial x_i} + \dot{q}_R \tag{2.9}$$

where J_i^q is the heat flux given by

$$J_i^q = -\lambda \frac{\partial T}{\partial x_i} + \sum_{\alpha=1}^{N} h_\alpha J_i^\alpha. \tag{2.10}$$

In Eq. (2.10), the first term represents the heat conduction while the last term is the enthalpy transport due to the diffusive fluxes J_i^α. The last term on the right-hand side of Eq. (2.9) is the heat source term due to external sources such as an electric spark or a laser but not due to heat release by combustion. The enthalpy of a mixture is the mass-weighted sum of the species enthalpies h_α, i.e.,

$$h = \sum_{\alpha=1}^{N} Y_\alpha h_\alpha. \tag{2.11}$$

For an ideal gas the species enthalpy h_α can be written as

$$h_\alpha = h_{\alpha,ref} + \int_{T_{ref}}^{T} c_{p_\alpha}(T) dT, \tag{2.12}$$

where c_{p_α} is the specific heat of species α at constant pressure and T is the

temperature in Kelvins. Differentiating Eq. (2.11) gives

$$dh = c_p dT + \sum_{\alpha=1}^{N} h_\alpha dY_\alpha, \tag{2.13}$$

where c_p is the heat capacity of the mixture at constant pressure calculated as

$$c_p = \sum_{\alpha=1}^{N} c_{p_\alpha} Y_\alpha. \tag{2.14}$$

Considering a low Mach number flow, the pressure convection term can be eliminated in Eq. (2.9), then inserting Eqs. (2.5), (2.10) and (2.13) into Eq. (2.9), Eq. (2.9) can be written as

$$\begin{aligned} \frac{\partial \rho h}{\partial t} + \frac{\partial \rho u_i h}{\partial x_i} =& \frac{\partial p}{\partial t} + \frac{\partial}{\partial x_i}\left(\frac{\lambda}{c_p}\frac{\partial h}{\partial x_i}\right) + \dot{q}_R \\ & - \sum_{\alpha=1}^{n} h_\alpha \frac{\partial}{\partial x_i}\left[\left(\frac{\lambda}{c_p} - \rho D_\alpha\right)\frac{\partial Y_\alpha}{\partial x_i}\right]. \end{aligned} \tag{2.15}$$

For the simplicity, assuming that the Lewis number is unity for all the species, the pressure is constant, and neglecting any external source term for enthalpy, $\dot{q}_R = 0$, and using Eq. (2.6), the enthalpy equation becomes

$$\frac{\partial \rho h}{\partial t} + \frac{\partial \rho u_i h}{\partial x_i} = \frac{\partial}{\partial x_i}\left(\rho D \frac{\partial h}{\partial x_i}\right). \tag{2.16}$$

Note that the enthalpy equation contains no source term so it is a conserved quantity.

Inserting Eqs. (2.4), (2.10) and (2.13) into Eq. (2.9), and assuming all specific heat capasities $c_{p,i}$ to be constant, neglecting the heat source term $\dot{q}_R$ and assuming the pressure to be constant, the conservation of energy can be also expressed in terms of temperature as

$$\frac{\partial \rho T}{\partial t} + \frac{\partial \rho u_i T}{\partial x_i} = \frac{\partial p}{\partial t} + \frac{\partial}{\partial x_i}\left(\rho D \frac{\partial T}{\partial x_i}\right) + \dot{\omega}_T, \tag{2.17}$$

where the source term is given by

$$\dot{\omega}_T = -\frac{1}{c_p}\sum_{\alpha=1}^{n} h_\alpha \dot{\omega}_\alpha. \tag{2.18}$$

2.2 Chemical Reaction Rates

Chemical reactions usually take place through a series of elementary reactions known as a chemical mechanism. In combustion, accurte description of chemical mechanism is challenging but of crucial importance. Therefore a lot of research has been conducted for accurate nodeling of the elementary reactions and the reaction rates. For example, a chemical mechanism for the methane oxidation consisting of 277 reactions and 49 species (GRI-Mech 2.11) [40] is commonly and successfully used to describe the methane/air combustion. A sample chemical mechanism for $H_2 - O_2$ combustion is given in Table 2.1 in the standard CHEMKIN format [6] in order to show general features of a typical chemical mechanism.

A chemical mechanism consisting of N species and M reactions can be written as:

$$\sum_{\alpha=1}^{N} \nu_{\alpha j}^{f} \mathcal{M}_\alpha \leftrightharpoons \sum_{\alpha=1}^{N} \nu_{\alpha j}^{b} \mathcal{M}_\alpha \text{ for } j = 1, M, \tag{2.19}$$

where $\mathcal{M}_\alpha$ is the chemical symbol of α^{th} species, $\nu_{\alpha j}^{f}$ and $\nu_{\alpha j}^{b}$ are the forward and backward stoichiometric coefficients of α^{th} species in the j^{th} reaction, respectively. Mass conservation of species implies that

$$\sum_{\alpha=1}^{N} \nu_{\alpha j}^{f} W_\alpha = \sum_{\alpha=1}^{N} \nu_{\alpha j}^{b} W_\alpha \quad \text{or} \quad \sum_{\alpha=1}^{N} \nu_{\alpha j} W_\alpha = 0 \text{ for } j = 1, M, \tag{2.20}$$

where W_α is the molecular weight of species α and $\nu_{\alpha j} = \nu_{\alpha j}^{f} - \nu_{\alpha k}^{b}$.

For species α, the rate of mass produced by all M reactions, $\dot{\omega}_\alpha$, is

$$\dot{\omega}_\alpha = \sum_{k=1}^{M} \dot{\omega}_{\alpha,k} = W_\alpha \sum_{k=1}^{M} \nu_{\alpha k} \dot{\mathcal{G}}_k. \tag{2.21}$$

Here $\dot{\mathcal{G}}_k$ is the process rate of k^{th} elementary reaction and it can be written as

$$\dot{\mathcal{G}}_k = K_{fk} \prod_{\alpha=1}^{N} [X_\alpha]^{\nu'^{f}_{\alpha k}} - K_{bk} \prod_{\alpha=1}^{N} [X_\alpha]^{\nu'^{b}_{\alpha k}} \tag{2.22}$$

where K_{fk} and K_{bk} are the forward and backward rates of k^{th} reaction and $[X_\alpha]$ is molar concentrations of species α defined as

$$[X_\alpha] = \frac{\rho Y_\alpha}{W_\alpha}. \tag{2.23}$$

The rates K_{fk} and K_{bk} are generally modelled using the Arrhenius law as

$$K_{fk} = A_{fk} T^{\beta_k} exp\left(-\frac{E_k}{RT}\right), \tag{2.24}$$

and

$$K_{bk} = \frac{K_{fk}}{\left(\frac{p_a}{RT}\right)^{\sum_{\alpha=1}^{N} \nu_{\alpha k}} exp\left(\frac{\Delta S_j^0}{R} - \frac{\Delta H_j^0}{RT}\right)}, \tag{2.25}$$

where A_{fk}, β_k and E_k are called pre-exponential constant, the temperature exponent and the activation energy, respectively, and are provided as part of the chemical mechanisms. In Table 2.1, the chemical mechanism consisting of 9 species and 19 reactions describes the $H_2 - O_2$ combustion and is shown here as an example. The first column of the table contains the elementary reactions whereas the next columns contain the data for A_{fk}, β_k and E_k, respectively.

Table 2.1: A sample 9 species - 19 reactions chemical mechanism for H_2 - O_2 combustion [6]. The columns contain the elementary reactions, and the data for A_{fk}, β_k and E_k, from left to right.

ELEMENTS				
H O N				
SPECIES				
H_2 O_2 OH O H H_2O HO_2 H_2O_2 N_2				
END				
REACTIONS				
1	$H_2+O_2=OH+OH$	1.700E13	0.00	47780.
2	$H_2+OH=H_2O+H$	1.170E09	1.30	3626.
3	$H+O_2=OH+O$	5.130E16	-0.81	16507.
4	$O+H_2=OH+H$	1.800E10	1.00	8826.
5	$H+O_2+M=HO_2+M$	2.100E18	-1.00	0.
	third-body efficiencies	/H_2 3.3/	/O_2 0./ /N_2 0./ /H_2O/21.0/	
6	$H+O_2+O_2=HO_2+O_2$	6.700E19	-1.42	0.
7	$H+O_2+N_2=HO_2+N_2$	6.700E19	-1.42	0.
8	$OH+HO_2=H_2O+O_2$	5.000E13	0.00	1000.
9	$H+HO_2=OH+OH$	2.500E14	0.00	1900.
10	$O+HO_2=O_2+OH$	4.800E13	0.00	1000.
11	$OH+OH=O+H_2O$	6.000E08	1.30	0.
12	$H_2+M=H+H+M$	2.230E12	0.50	92600.
	third-body efficiencies	/H2 3./ /H 2./ /H2O 6.0/		
13	$O_2+M=O+O+M$	1.850E11	0.50	95560.
14	$H+OH+M=H_2O+M$	7.500E23	-2.60	0.
	third-body efficiencies	/H2O 20.0/		
15	$HO_2+H=H_2+O_2$	2.500E13	0.00	700.
16	$HO_2+HO_2=H_2O_2+O_2$	2.000E12	0.00	0.
17	$H_2O_2+M=OH+OH+M$	1.300E17	0.00	45500.
18	$H_2O_2+H=H_2+HO_2$	1.600E12	0.00	3800.
19	$H_2O_2+OH=H_2O+HO_2$	1.000E13	0.00	1800.
END				

Chapter 3

TURBULENCE AND COMBUSTION MODELING

3.1 Characteristics of Turbulence

The most engineering flows are turbulent and many involve chemical reactions. The origin of turbulence is instability of flow caused by growth of perturbations at a high Reynolds number. For example, a laminar pipe flow becomes turbulent at the Reynolds number of about 2000. In contrary to common occurrence in the practical applications, an exact definition of turbulence is very difficult. However, general characteristics of turbulent flows can be listed as: (1) Randomness - all flow properties have random fluctuations. (2) Diffusivity - Turbulence significantly increases the mixing of scalars and the rate of momentum, heat and mass transfer. (3) Large Reynolds numbers - Turbulence occurs at large Reynolds numbers. (4) Three-dimensional vorticity fluctuations - Turbulent flow is three dimensional and rotational. If a flow has random motions with zero-vorticity, then it is not a turbulent flow. (5) Dissipation - Turbulent flows are dissipative. The turbulent kinetic energy is always transferred from the large scales to the small scales. At the smallest scale, the turbulent kinetic energy is converted into the internal energy through the viscous dissipation. (6) Continuum - The smallest scale occurring in a turbulent flow is sufficiently larger than the mean free path so the flow can be safely assumed to be continuum. (7) Property of flow - Turbulence is not a property of fluid but a property of flow.

3.2 Statistical Description of Turbulence

Due to the random nature of turbulence, the main aim is to characterize the flow fields in terms of their statistical distributions. To statistically describe a turbulent flow, the

cumulative distribution and the associated probability density functions of any scalar (for example the velocity component u_i) are commonly used. Figure 3.1 shows two different series of x-component of velocity u and the corresponding probability density functions. The statistical moments and the correlations between two scalar fields play an important role in the statistical description of the turbulent flow. The detailed mathematical definitions of the cumulative distribution function and the probability density function, and the statistical moments will be given in Chapter 4.

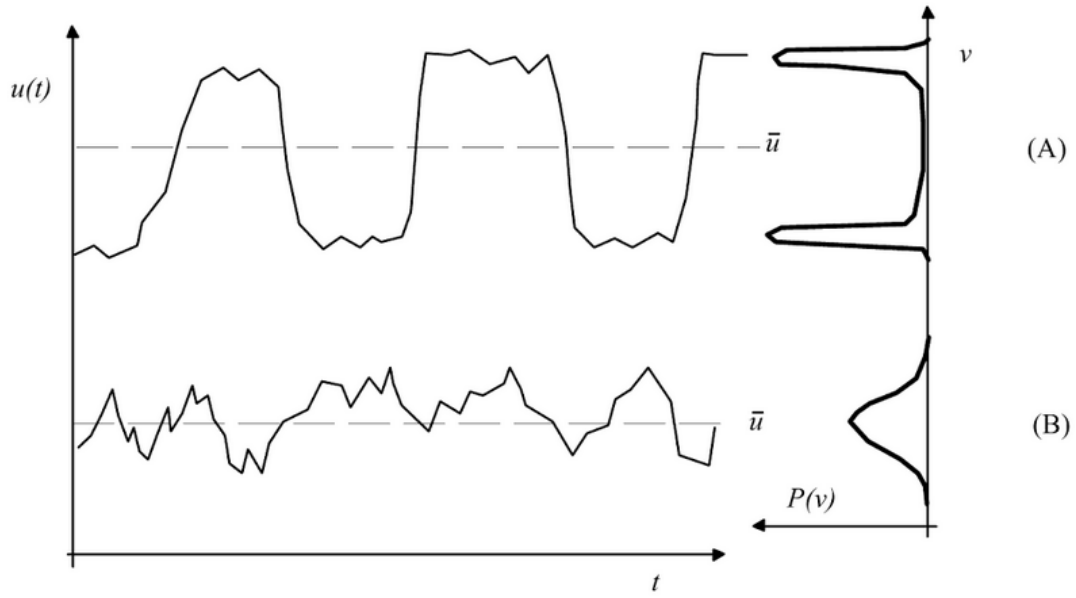

Figure 3.1: Two different series of x-component of the velocity vector u and the corresponding probability density functions [7].

3.3 Turbulent Scales

A turbulent flow has a large range of time and length scales. The Richardson's energy cascade idea [41] provides a useful definition for the turbulent motions. The first concept in Richardson's energy cascade is that a turbulent flow consists of different size of eddies that are defined as a correlated turbulent motion within a region of size l. Figure 3.2 shows a schematic representation of different size of eddies in a turbulent jet flow. Eddies of size l can be characterized by velocity $u(l)$ and a time scale

$\tau(l) \equiv l/u(l)$. A region of a small-scale eddy can be contained by a large-scale eddy as demonstrated in Fig. 3.2. The interaction between different size of eddies has been

Figure 3.2: Schematic representation of different size of eddies in a turbulent jet flow.

well explained by Richardson's idea of energy cascade [41]. Richardson stated that the large eddies are unstable and break up to transfer their energy into the smaller eddies [41]. And then these smaller eddies further break up into even smaller eddies until the smallest size of eddies have a Reynolds number $Re(l) = u(l)/l$ that is sufficiently small so that the molecular viscosity dissipates the kinetic energy contained in these eddies. The energy dissipation process is placed at the end of the energy cascade of the eddies. Consequently, the rate of dissipation ε at the small scales can be determined by the rate of energy transfer at the largest eddies, $u_0^2/\tau_0 = u_0^3/l_0$ where l_0, u_0 and τ_0 are the length, velocity and time scales of the largest eddies in the turbulent motion.

Although, Richardson's cascade idea enlightens how the kinetic energy is transferred within the different sizes of eddies, it does not state any idea about the size of the smallest eddies which are responsible for the dissipation of the kinetic energy. The Kolmogorv hypotheses [14, 42] characterize the scales in the smallest eddies in turbulent flows. Kolmogorov first stated that the directional information imposed by flow geometry and boundary conditions is lost once the large eddies break up into small size eddies. Therefore the small-scale turbulent motions are statistically isotropic.

Additionally, Kolmogorov stated that the statistics of the small-scale motions have a universal form that is uniquely determined by kinematic viscosity ν and dissipation rate ε. Given these two parameters ν and ε, unique length, velocity, and time scales can be formed as

$$\eta \equiv \left(\frac{\nu^3}{\varepsilon}\right)^{1/4}, \tag{3.1}$$

$$u_\eta \equiv (\nu\varepsilon)^{1/4}, \tag{3.2}$$

$$\tau_\eta \equiv \left(\frac{\nu}{\varepsilon}\right)^{1/2}. \tag{3.3}$$

These are called the Kolmogorov scales (the smallest scales in a turbulent flow). Finally, the ratio of the smallest scale and the largest scale in a turbulent flow can be determined from the scaling $\varepsilon \sim u_0^3/l_0$ as

$$\frac{\eta}{l_0} \sim Re^{-3/4}, \tag{3.4}$$

$$\frac{u_\eta}{u_0} \sim Re^{-1/4}, \tag{3.5}$$

$$\frac{\tau_\eta}{\tau_0} \sim Re^{-1/2}. \tag{3.6}$$

The ratio of the smallest size to the largest size of eddies is very important in computational modeling of turbulent flows. In the numerical solution of the conservation equations of a reacting flow without using any model for the turbulence, the computational grid should be sufficiently fine to resolve the smallest scales and it should be sufficiently large to contain the largest scales. Therefore the grid size used in the DNS simulations should scale as $Re^{3/4}$. Also the time step should be smaller than the smallest time scale of the turbulent flow. Thus the computational cost scales as Re^3.

3.4 Modeling of Turbulent Flows

In the study of turbulent flows, there exist three main modeling approaches: the direct numerical simulation (DNS), the Reynolds averaged Navier-Stokes (RANS) and the large-eddy simulation (LES) methods. In the DNS method, the instantaneous conservation equations, Eqs. (2.1), (2.2), (2.4), (2.9) and (2.17), are directly solved without using any model and resolving all the length and time scales in the turbulent motion. Thus the DNS resolves all turbulent scales from the largest to the Kolmogorov scales.

In the RANS method, any field, ϕ, in a turbulent flow is decomposed into its mean and fluctuating parts as

$$\phi = \langle\phi\rangle + \phi'. \tag{3.7}$$

The solution for the mean fields, $\langle\phi\rangle$, is obtained by solving the mean conservation equations that are derived by taking an average of the instantaneous conservation equation. In the RANS, the turbulence is totally modelled.

In the LES method, a filtering operation is applied to the turbulent motion to obtain filtered fields by removing the small-scales. Mathematically the filtering operation can be expressed as

$$\phi_f = \int \phi \boldsymbol{G}(\boldsymbol{x} - \boldsymbol{x'}) \boldsymbol{dx'}, \tag{3.8}$$

where ϕ_f denotes the filtered field and $\boldsymbol{G}$ is the LES filter. In the LES, the governing equations for the filtered fields are derived by applying the filtering operation to the instantaneous conservation equations, Eqs. (2.1), (2.2), (2.4), (2.9) and (2.17). In this approach, the large scale motions that are directly affected by boundary conditions are explicitly calculated whereas the effects of small-scale motions are modelled. Figure 3.3 shows a sketch for a variation of a scalar field (e.g., temperature) calculated by the DNS, the LES and the RANS methods.

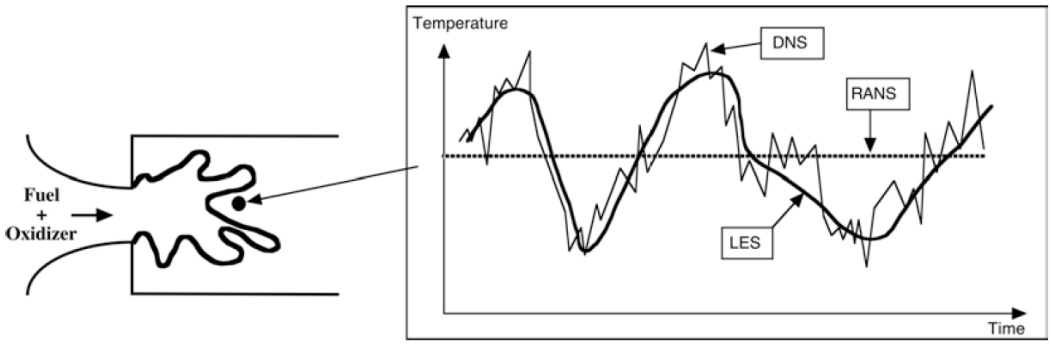

Figure 3.3: Typical time series of instantaneous, filtered and mean temperatures computed at a point with DNS, LES and RANS methods, respectively [8].

Comparing the computational cost of the three approaches, the DNS method is the most accurate but computationally the most expensive method since it must resolve all turbulent scales. As mentioned before, the size of the computational grid scales as $Re^{3/4}$ and the total computational cost as Re^3 in a DNS simulation. For example, in a typical turbulent flow with a moderate level of Reynolds number, i.e., $Re = 5000$, considering the 3-dimensionality of turbulence, the computational grid size must be at least order of millions because the grid should be sufficiently fine to resolve the small-scale motions and the computational domain should be sufficiently large to cover the large-scale motions. The computational cost required in a typical DNS simulation is the order of million CPU hours [43, 44, 45]. Thus the DNS is not a feasible method to be used in practical engineering problems. The DNS is mostly used for academic purposes. On the other hand, the computational cost of the RANS method is very low compared to that of the DNS since only the mean fields are calculated in the RANS approach. Additionally, the computational cost in RANS simulations can be made even smaller when the flow is statistically two dimensional. Because of its low computational cost, the RANS method is used as a standard method in practical engineering problems. In terms of computational cost, the LES method lies between the DNS and the RANS approaches. The LES requires much less computational cost than that of the DNS since the small-scale motions are

modelled. However, the cost in the LES is often 100 to 1000 times higher than that in the RANS methods since the large-scale motions are explicitly resolved [8] in the LES. Inspite of relatively high cost of the LES, it has very important advantages over the RANS method. Since the RANS method calculates only the mean fields, it is not sufficient to precisely model the important processes of ignition and quenching as well as the complex flows involveing swirling, unsteady features, whereas the LES has proven to show good performance for accurate modeling of these events.

3.5 Modeling of Turbulence and Combustion

In many engineering problems, the main interest is to compute only the mean fields in turbulent flows. The governing equations for the mean quantities can be derived by taking the average of the instantaneous conservation equations for mass, momentum, species and energy. As mentioned before, this approach is known as the Reynolds averaged Navier-Stokes (RANS). Although the main focus is not on the RANS based models in this study, the RANS method is first briefly discussed because of its historical importance and simplicity in representing the modeling concepts for turbulent combustion.

In the RANS approach, any flow quantity ϕ can be split into its mean and fluctuation components as

$$\phi = \langle\phi\rangle_{mass} + \phi', \tag{3.9}$$

where $\langle\phi\rangle_{mass}$ and ϕ' denote the mass-weighted mean (the Favre-average mean) and fluctuating components of ϕ. We note that $\langle\phi'\rangle_{mass} = 0$ by definition. The mass-weighted average is defined as

$$\langle\phi\rangle_{mass} = \frac{\langle\rho\phi\rangle}{\langle\rho\rangle}, \tag{3.10}$$

where $\langle . \rangle$ denotes a volume or Reynolds averaged quantity. Using this decomposition for all the flow quantities, the mean conservation equation can be obtained by tak-

ing average of the instantaneous conservation equations. Details of derivations can be found in standard textbooks, e.g., Pope [12]. The resulting mean conservation equations can be written as

$$\frac{\partial \langle\rho\rangle}{\partial t} + \frac{\partial \langle\rho\rangle \langle u_i\rangle_{mass}}{\partial x_i} = 0, \tag{3.11}$$

$$\frac{\partial \langle\rho\rangle \langle u_i\rangle_{mass}}{\partial t} + \frac{\partial \langle\rho\rangle \langle u_i\rangle_{mass} \langle u_j\rangle_{mass}}{\partial x_j} = -\frac{\partial \langle p\rangle}{\partial x_i} + \frac{\partial \langle\tau_{ij}\rangle}{\partial x_j} - \frac{\partial \langle\rho\rangle \left\langle u_i' u_j'\right\rangle_{mass}}{\partial x_j}, \tag{3.12}$$

$$\frac{\partial \langle\rho\rangle \langle h\rangle_{mass}}{\partial t} + \frac{\partial \langle\rho\rangle \langle u_i\rangle_{mass} \langle h\rangle_{mass}}{\partial x_i} = -\frac{\partial}{\partial x_i}\left(\left\langle \rho D \frac{\partial h}{\partial x_i} \right\rangle\right) - \frac{\partial \langle\rho\rangle \langle u_i' h\rangle_{mass}}{\partial x_i}. \tag{3.13}$$

$$\frac{\partial \langle\rho\rangle \langle Y_\alpha\rangle_{mass}}{\partial t} + \frac{\partial \langle\rho\rangle \langle u_i\rangle_{mass} \langle Y_\alpha\rangle_{mass}}{\partial x_i} = -\frac{\partial}{\partial x_i}\left(\left\langle \rho D \frac{\partial Y_\alpha}{\partial x_i} \right\rangle\right) - \frac{\partial \langle\rho\rangle \langle u_i' Y_\alpha\rangle_{mass}}{\partial x_i} + \langle\dot{\omega}_\alpha\rangle\,. \tag{3.14}$$

As can be seen in Eqs. (3.11)-(3.14), the averaging of the instantaneous equations gives rise to the new terms in the mean conservation equations. The new terms cannot be generally expressed in terms of the known fields (the mean of density, velocity, mass fractions or enthalpty). Therefore they are in the unclosed form and responsible for the closure problem in turbulent (reacting) flows. The solution of the mean conservation equations requires to close or model these terms. The unclosed terms, $\langle\rho\rangle \left\langle u_i' u_j'\right\rangle_{mass}$ in Eq. (2.2) known as the Reynolds stresses, are often modelled by the turbulent viscosity assumption as

$$\langle\rho\rangle \left\langle u_i' u_j'\right\rangle_{mass} = \mu_t \left(\frac{\partial \langle u_i\rangle_{mass}}{\partial x_j} + \frac{\partial \langle u_j\rangle_{mass}}{\partial x_i} - \frac{2}{3}\delta_{ij} \frac{\partial \langle u_k\rangle_{mass}}{\partial x_k} \right) + \frac{2}{3} \langle\rho\rangle k, \tag{3.15}$$

where μ_t is the turbulent dynamic viscosity, δ_{ij} is the Kronecker delta and k is turbulent kinetic energy defined as

$$k = \frac{1}{2} \langle u_m' u_m'\rangle_{mass}\,. \tag{3.16}$$

In the literature, various models have been proposed to model the turbulent viscosity μ_t [46, 47, 48, 49].

The other unclosed term is the species turbulent fluxes $\langle\rho\rangle \langle u_i' Y_\alpha\rangle_{mass}$ appering in Eq. (3.14). This term is usually modelled by the classical gradient diffusion assumption as

$$\langle\rho\rangle \langle u_i' Y_\alpha\rangle_{mass} = -\frac{\mu_t}{Sc_\alpha} \frac{\partial \langle Y_\alpha\rangle_{mass}}{\partial x_i}, \tag{3.17}$$

where Sc_α is the turbulent Schmidt number for species α. In Eq. (3.14), the term for laminar diffusive fluxes for species, $\left\langle \rho D \frac{Y_\alpha}{\partial x_i} \right\rangle$, is usually modelled as

$$-\left\langle \rho D \frac{Y_\alpha}{\partial x_i} \right\rangle = -\langle\rho\rangle \langle D\rangle_{mass} \frac{\partial \langle Y_\alpha\rangle_{mass}}{\partial x_i}. \tag{3.18}$$

Following the same procedures, the unclosed terms in the conservation of enthalpy are modelled as

$$\langle\rho\rangle \langle u_i' h\rangle_{mass} = -\frac{\mu_t}{Sc_\alpha} \frac{\partial \langle h\rangle_{mass}}{\partial x_i}, \tag{3.19}$$

and

$$-\left\langle \rho D \frac{h}{\partial x_i} \right\rangle = -\langle\rho\rangle \langle D\rangle_{mass} \frac{\partial \langle h\rangle_{mass}}{\partial x_i}. \tag{3.20}$$

The last but the most challenging unclosed term is the chemical reaction source term, $\langle\dot{\omega}_\alpha\rangle$. To demonstrate the degree of its complexity, let's consider a simple irreversible reaction between fuel (F) and oxidizer (O) as

$$mF + nO \rightarrow P, \tag{3.21}$$

where P denotes the product. Then the fuel mass reaction rate $\dot{\omega}_F$ is typically ex-

pressed as

$$\dot{\omega}_F = -W_F A_1 T^{\beta_1} exp\left(-\frac{E_1}{T}\right)[X_F]^m[X_O]^n, \tag{3.22}$$

where A_1, β_1 and E_1 are pre-exponential constant, the temperature exponent and the activation energy, respectively. In Eq. (3.22), W_F is the molecular weight of the fuel, T is temperature, and $[X_F]$ and $[X_O]$ are the molar concentrations of fuel and oxygen, respectively. The reaction rate $\dot{\omega}_F$ is highly non-linear as seen in Eq. (3.22), thus the average reaction rate, $\langle\dot{\omega}_F\rangle$ cannot be easily written as a function of mean fields of mass fractions, density and mean temperature. Therefore the modelling the average reaction rate gives rise to the most challenging task in turbulent combustion modelling.

Since it is not possible to express the mean reaction rates in terms of mean quantities, the models to close the mean reaction rate term are generally derived from a physical analysis. As mentioned before, Veynante and Vervisch [25] classified the physical approaches into three groups: Geometric analysis, turbulent mixing based approach and one-point statistics approach. These approaches are depicted schematically in Fig. 3.4. In the geometrical analysis, the flame front that is generally represented as iso-surface of a mass fraction is described as a geometrical surface evolving with the turbulent flow. In this approach, the flame is assumed to be very thin compared to all scales in the turbulent flame, and the mean reaction rate is calculated based on the geometric feature of the flame front such as flame surface density. The level set model [50] is commonly used to determine the location of the flame front. In the turbulent mixing based approach, the models are developed by assuming that the chemical time scales are much shorter than the turbulent time scales such that the chemical reactions occur much faster than the turbulent mixing. Therefore the reaction rates are mainly controlled by the rate of turbulent mixing. The eddy break up (EBU) model [51] and eddy dissipation concept (EDC) [52] are commonly used models based on the very fast chemistry assumption. In the one-point statistics approach, the mean reaction rates are computed naturally from the joint

PDF as

$$\bar{\dot{\omega}}_\alpha = \int_{\psi_1,\psi_2,...\psi_N} \dot{\omega}_\alpha(\psi_1,\psi_2,...\psi_N) p(\psi_1,\psi_2,...\psi_N) d\psi_1, d\psi_2, ...d\psi_N, \tag{3.23}$$

where $\dot{\omega}_\alpha$ is the instantaneous reaction rate of species α calculated by the Arrhenius law, ψ_i $(i = 1, 2, ..., N)$ are the sample space variables for compositions, and $p(\psi_1, \psi_2, ...\psi_N)$ is the joint probability density function of the compositions. The models in the one-point statistics approach does not depend on the flame structure, thus they can calculate the mean reaction rates for premixed (fuel and oxidizer are mixed before reactions), non-premixed and partially premixed flames as well as fast and slow chemistry without requiring any modeling assumption. In the transported PDF, a transport equation is solved to calculate the joint PDF of chemical species. The mean reaction rate is then calculated via Eq. (3.23) without using any model since it is in the closed form. However, in the transport equation, the molecular diffusion term is in unclosed form and should be modelled as will be discussed in the next chapter. In this thesis, the transported PDF model is employed to model the mean reaction rates. The detail of the method will be provided in the next chapter.

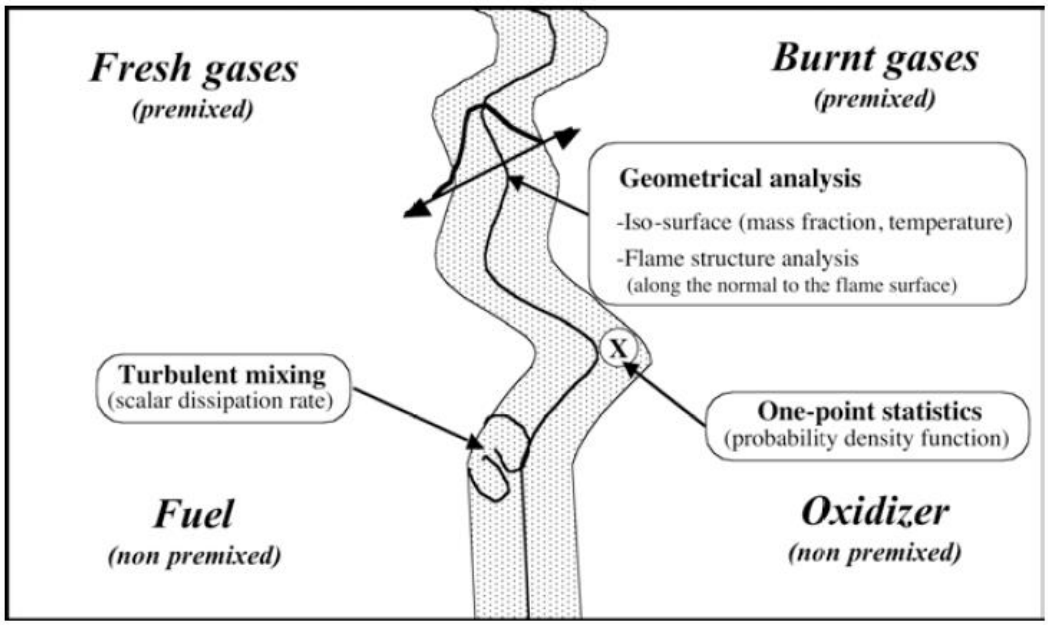

Figure 3.4: Three different modeling approaches: The geometric analysis, the turbulent mixing based approach, and the probability density function approach [8].

Chapter 4

THE PDF MODELING OF TURBULENT REACTING FLOWS

In the turbulent reacting flows, any field ϕ (e.g., the mass fraction of a species, a velocity component of the flow) at a particular position $\boldsymbol{x}_0$ and time t_0 takes different values in each realization. This is due to the chaotic nature of the turbulent flows. Therefore, the value of ϕ cannot be determined at a given position and time beforehand from the values of given realizations. However, we can attribute a value for its probability of being in a given interval. The PDF methods calculate the probabilities of the fields in turbulent reacting flows for being in a given interval by solving modelled transport equations. In this section, before explaining the modelled transport equations for the PDF, we first introduce the basic statistical concepts used in the PDF methods. Then the joint PDF methods in both RANS and LES contexts are presented. After that, the hybrid solution method is represented for the numerical solution of the LES/PDF model equations. Finally, the in situ adaptive tabulation (ISAT) method [1] is describe for the calculations of combustion chemistry.

4.1 The Basic Statistical Concepts

In a typical experiment for a turbulent mixing-layer as sketched in Fig. 4.1, the measured quantities at a particular position $\boldsymbol{x}_0$ and time t_0 will be different in each realization of the experiments. Although the flow is governed by the same deterministic equations with nominally the same initial and boundary conditions, any slight difference in flow conditions (i.e., small change in air movement in the environment) can lead to totally different flow characteristics. In an experiment, the small changes in boundary or initial conditions cannot be controlled (or measured) thus the result-

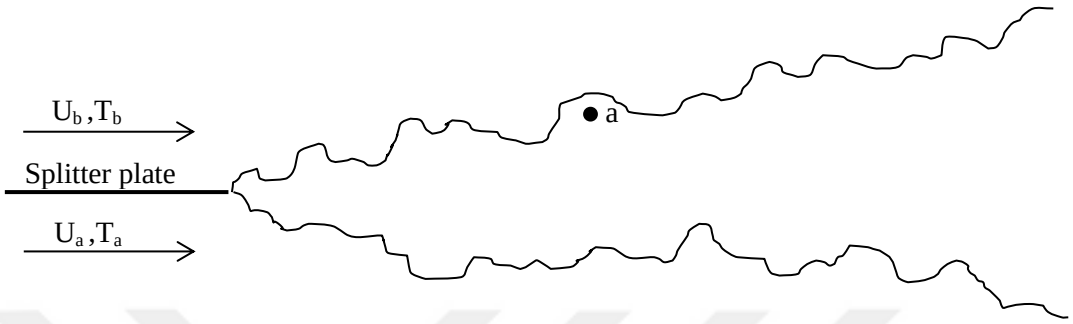

Figure 4.1: A sketch of a planar turbulent mixing layer

ing flow properties cannot be determined beforehand. Therefore the flow properties in the turbulent flows are treated as random variables. For example, the velocity and temperature fields at the position a in Fig. 4.1 are random variables. A sample space of random variable is defined as the space from which the random variable can take values. An event of a random variable is then defined as a subset (region) of the sample space. Figure 4.2 depics a sample space and a region corresponding to an event $A \equiv 1/3 \leq \phi < 2/3$. The probability of the occurrence of the event A is denoted by

$$\boldsymbol{P}(A) \equiv \boldsymbol{P}(1/3 \leq \phi < 2/3). \tag{4.1}$$

The probability of any event is a real number between zero and one. If the occurrence of the event A is impossible then $\boldsymbol{P}(A) = 0$. If the occurrence of the event A is certain then $\boldsymbol{P}(A) = 1$.

To describe the characteristics of a random variable, the convenient way is to define the distribution function of the random variable. A distribution function gives the probability of a region for a random variable as

$$F_\phi(\psi) \equiv \boldsymbol{P}(\phi < \psi), \tag{4.2}$$

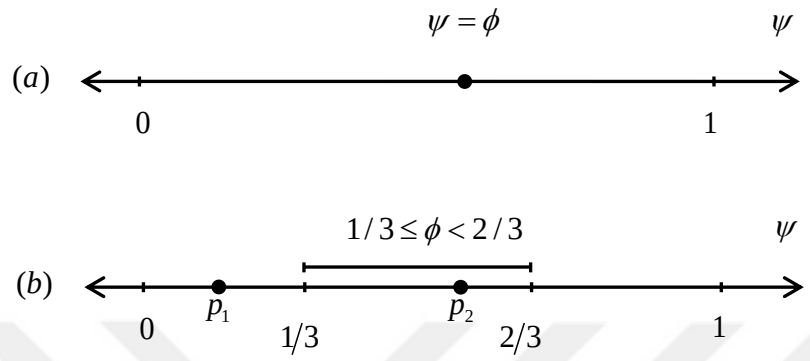

Figure 4.2: (a) Sample space (ψ-space) for a random variable ϕ, with the sample point $\psi = \phi$. (b) Sample space showing the region corresponding to the event $A \equiv 1/3 \leq \phi < 2/3$ where p_1 sample point for which A occurs and p_2 is the sample point for which A does not occur.

where ψ is sample space variable of the random varible of ϕ. Then from the definition, the probability of event in Fig. 4.2 is computed as

$$\begin{aligned} \boldsymbol{P}(A) &= \boldsymbol{P}(1/3 \leq \phi < 2/3), \\ &= \boldsymbol{P}(\phi < 2/3) - \boldsymbol{P}(\phi < 1/3), \\ &= F_\phi(2/3) - F_\phi(1/3), \end{aligned} \tag{4.3}$$

which is sketched in Fig. 4.3 . The probability of any region smaller than $-\infty$ is zero and smaller than ∞ is one, i.e.,

$$\boldsymbol{P}(\phi < -\infty) = F_\phi(-\infty) = 0, \ \boldsymbol{P}(\phi < \infty) = F_\phi(\infty) = 1. \tag{4.4}$$

The distribution function F_ϕ is a non-decreasing function taking values from zero to one as ϕ increases from $-\infty$ to ∞.

The probability density function (PDF) of the random variable ϕ is then defined

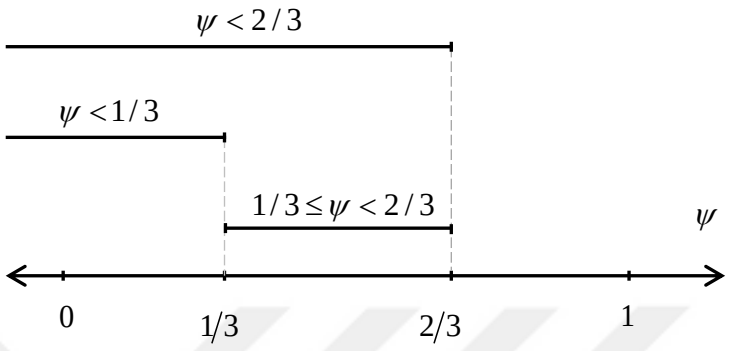

Figure 4.3: Sample space showing the region $1/3 \leq \phi < 2/3$ as the difference between the regions $\phi < 1/3$ and $\phi < 2/3$.

by

$$f_\phi(\psi) \equiv \frac{d}{d\psi} F_\psi(\psi). \tag{4.5}$$

The PDF, $f_\phi(\psi)$, is the probability per unit ψ. Then $f_\phi(\psi)d\psi$ gives the probability of ϕ being in an infinitesimal interval of $\psi \leq \phi < \psi + d\psi$. Figure 4.4 schematically shows the distribution function $F_\phi(\psi)$ and the corresponding probability density function $f_\phi(\psi)$ of a random variable ϕ. The PDF is a non-negative function, i.e.,

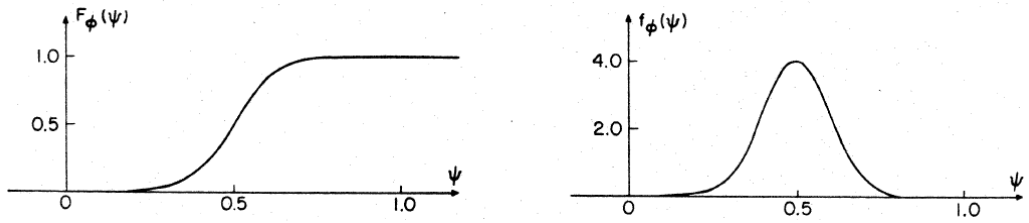

Figure 4.4: The distribution function $F_\phi(\psi)$ (left) and the corresponding probability density function $f_\phi(\psi)$ (right) [9].

$$f_\phi(\psi) \geq 0. \tag{4.6}$$

The normalization condition requires that,

$$\int_{-\infty}^{\infty} f_\phi(\psi) d\psi = 1. \tag{4.7}$$

Its values at the positive and negative infinities are zero, i.e.,

$$f_\phi(-\infty) = f_\phi(\infty) = 0. \tag{4.8}$$

For any function $K(\phi)$, the mean is then defined as the expectation of K as

$$\langle K \rangle = \int_{-\infty}^{\infty} f_\phi(\psi) K(\psi) d\psi. \tag{4.9}$$

Any random variable can be decomposed into its mean and fluctuating parts as

$$K \equiv \langle K \rangle + K'. \tag{4.10}$$

The central moments are then defined as

$$\left\langle K'^m \right\rangle = \int_{-\infty}^{\infty} f_\phi(\psi) \left(K(\psi) - \langle K(\psi) \rangle \right)^m d\psi, \tag{4.11}$$

where m is a positive number. For instance, the second central moment

$$\left\langle K'^2 \right\rangle = \int_{-\infty}^{\infty} f_\phi(\psi) \left(K(\psi) - \langle K(\psi) \rangle \right)^2 d\psi, \tag{4.12}$$

is called the variance, $var(K)$, and its standard deviation is defined as squared-root of the variance as

$$sdev(K) = \sqrt{var(K)} = \left(\left\langle K'^2 \right\rangle \right)^{1/2}. \tag{4.13}$$

Typically in a turbulent reacting flow, a large number of species, N, are used to represent the combustion chemistry. Consequently, instead of a single random variable, jointly distributed random variables of $\boldsymbol{\phi} = \{\phi_1, \phi_2, ..., \phi_N\}$ should be considered to

describe turbulent reacting flows. The properties of the distribution function and the probability density function can be straightforwardly extended from those of the single random variable. For example, the probability of an event $A \equiv \{\phi_1 < \psi_1 \text{ and } \phi_2 < \psi_2\}$ is written as

$$P(A) = P(\phi_1 < \psi_1, \phi_2 < \psi_2) = F_{\phi_1\phi_2}(\psi_1, \psi_2), \tag{4.14}$$

which gives the probability of ϕ_1 being smaller than ψ_1 and ϕ_2 being smaller than ψ_2. Then the joint probability density function $f_{\phi_1\phi_2}$ can be defined as

$$f_{\phi_1\phi_2}(\psi_1, \psi_2) = \frac{\partial^2 F_{\phi_1\phi_2}(\psi_1, \psi_2)}{\partial\psi_1\partial\psi_2}. \tag{4.15}$$

By definition, the PDF of ϕ_1 (as also called the marginal PDF) can be obtained from the joint PDF $f_{\phi_1\phi_2}$ by integration over all possible realizations of ϕ_2 as

$$f_{\phi_1}(\psi_1) = \int_{-\infty}^{+\infty} f_{\phi_1\phi_2}(\psi_1, \psi_2)d\psi_2. \tag{4.16}$$

The covariance of ϕ_1 and ϕ_2 is defined as

$$\langle\phi_1'\phi_2'\rangle = \int_{-\infty}^{+\infty}\int_{-\infty}^{+\infty}(\psi_1 - \langle\phi_1\rangle)(\psi_2 - \langle\phi_2\rangle)f_{\phi_1\phi_2}(\psi_1, \psi_2)d\psi_1 d\psi_2. \tag{4.17}$$

In general case, the probability of an event $A \equiv \{\phi_1 < \psi_1, \phi_2 < \psi_2, \ ... \ , \phi_N < \psi_N\}$ for jointly distributed random variables of $\boldsymbol{\phi} = \{\phi_1, \phi_2, ..., \phi_N\}$ is written as

$$P(A) = P(\phi_1 < \psi_1, \phi_2 < \psi_2, ..., \phi_N < \psi_N) = F_{\phi_1\phi_2...\phi_N}(\psi_1, \psi_2, ..., , \psi_N), \tag{4.18}$$

then the joint probability density function $f_{\phi_1\phi_2...\phi_N}$ can be defined as

$$f_{\phi_1\phi_2.....\phi_N}(\psi_1, \psi_2, ..., \psi_N) = \frac{\partial^N F_{\phi_1\phi_2...\phi_N}(\psi_1, \psi_2, ..., \psi_N)}{\partial\psi_1\partial\psi_2...\partial\psi_N}. \tag{4.19}$$

Finally, the covariance of ϕ_1, ϕ_2,...,ϕ_N is defined as

$$\langle \phi_1' \phi_2' ... \phi_N' \rangle = \int_{-\infty}^{+\infty} \int_{-\infty}^{+\infty} ... \int_{-\infty}^{+\infty} (\psi_1 - \langle \phi_1 \rangle)(\psi_2 - \langle \phi_2 \rangle)...(\psi_N - \langle \phi_N \rangle) \quad (4.20)$$
$$f_{\phi_1 \phi_2 ..... \phi_N} d\psi_1 d\psi_2 ... d\psi_N.$$

In the most of the turbulent reacting flows, the statistics of a random field $\boldsymbol{\phi}$ change in space and time thus the PDF of the field $\boldsymbol{\phi}$ is a function of space $\boldsymbol{x}$ and time t. Therefore writting the PDF of the field $\boldsymbol{\phi}$ as $f_\phi(\boldsymbol{\psi}; \boldsymbol{x}, t)$ is convenient. Note that the density function of ϕ has the dimensions of ϕ^{-1} [53].

4.2 PDF Modeling of Turbulent Reacting Flows

In a turbulent reacting flow, the main interest is to compute the mean and variance of any function $K(\boldsymbol{\phi}, \boldsymbol{x}, t)$. As presented in the previous section, knowing the joint PDF $f(\boldsymbol{\psi; x, t})$ of compositions at every point $\boldsymbol{x}$ and time t, the statistics of any function $K(\boldsymbol{\phi}, \boldsymbol{x}, t)$ in turbulent reacting flows can be calculated at any position and time. In the PDF modeling of turbulent reacting flows, a modelled transport equation for the joint PDF of (velocity and) compositions are solved to evolve the joint PDF in space and time. The transport equation of the joint PDF of compositions (and velocity) is directly derived from its definition and the conservation equations. The PDF modeling of the turbulent reacting flows was initially developed in the RANS context. Therefore the PDF models in the RANS context are briefly described first in this section. Then the joint PDF of compositions in the LES context is discussed.

4.2.1 The Joint Compositions PDF Method in the RANS Context

In the joint compositions PDF method, we consider the composition variables of mass fractions of chemical species and enthalpy as random variables and consider the transport of their joint PDF instead of their finite moments.

The one-point, one-time, mass-weighted joint PDF of compositions at location $\boldsymbol{x}$

and time t is defined as

$$\langle\rho\rangle\, f_\phi(\boldsymbol{\psi};\boldsymbol{x},t) \equiv \rho(\boldsymbol{\psi})\,\langle\delta(\boldsymbol{\psi}-\boldsymbol{\phi})\rangle\,, \tag{4.21}$$

where ρ is density, and $\boldsymbol{\psi} = (\psi_1, \psi_2, ...\psi_{n_\phi})$ is the sample space variable of the compositions. The delta function $\delta(\boldsymbol{\psi}-\boldsymbol{\phi})$ is called the fine-grained PDF. Note that, the joint PDF of compositions is defined by averaging the fine-grained PDF of the compositions. Then the transport equation for the mass-weighted joint PDF of the compositions can be derived from Eq. (4.21), and the conservation of mass fractions and enthalpy equations using the standard techniques and can be written as [53]

$$\begin{aligned}\frac{\partial\,\langle\rho\rangle\, f_{\boldsymbol{\phi}}}{\partial t} + \frac{\partial\,\langle\rho\rangle\,\langle u\rangle_i\, f_{\boldsymbol{\phi}}}{\partial x_i} + \frac{\partial}{\partial x_i}\left[\langle\rho\rangle\,\langle u_i'|\boldsymbol{\psi}\rangle\, f_{\boldsymbol{\phi}}\right] = \\ \frac{\partial}{\partial\psi_j}\left[\langle\rho\rangle\, f_{\boldsymbol{\phi}}\left\langle\frac{1}{\langle\rho\rangle}\frac{\partial J_i^j}{\partial x_i}\middle|\boldsymbol{\psi}\right\rangle\right] \\ -\frac{\partial}{\partial\psi_j}\left[\langle\rho\rangle\, f_{\boldsymbol{\phi}}\dot{\omega}_{\phi_j}\right],\end{aligned} \tag{4.22}$$

where J_i^α denotes the molecular diffusion fluxes of the composition j in direction x_i. The first two terms on the left-hand side represent the rate of change following the mean flow, the last term represents the transport of $f_{\boldsymbol{\phi}}$ in the physical space due to the fluctuating velocity $u_i' = u_i - \langle u\rangle_i$ and the term $\langle u_i'|\boldsymbol{\psi}\rangle$ is the mean of the fluctuating velocity conditional upon the event $\boldsymbol{\phi} = \boldsymbol{\psi}$. The conditional mean is in the unclosed form and thus should be modelled. It is usually modelled by the gradient diffusion assumption as

$$\langle\rho\rangle\,\langle u_i'|\boldsymbol{\psi}\rangle\, f_{\boldsymbol{\phi}} = -D_T\frac{\partial f_{\boldsymbol{\phi}}}{\partial x_i}, \tag{4.23}$$

where D_T is the turbulent diffusivity. The first term on the right-hand side of Eq. (4.22) represents the change of $f_{\boldsymbol{\phi}}$ in the composition space due to the molecular mixing, which is also in the unclosed form. Modeling this term is the challenging part of the PDF models since the joint PDF of compositions contains only the one-point

and one-time information. Therefore it does not contain the correlations between the two- or multi-points required to calculate the molecular mixing. Note that modeling the molecular mixing term is still an active research area. The models developed for this term are generally called the mixing models. There are several mixing models available in the literature [54, 55, 56]. The interaction by exchange with the mean (IEM) is the simplest mixing model widely used in the PDF simulations. In the IEM mixing model [57], the term $\left\langle \frac{1}{\langle\rho\rangle}\frac{\partial J_i^j}{\partial x_i}\middle|\boldsymbol{\psi}\right\rangle$ is modelled by

$$\left\langle \frac{1}{\langle\rho\rangle}\frac{\partial J_i^j}{\partial x_i}\middle|\boldsymbol{\psi}\right\rangle = -\frac{1}{2}C_\phi\Omega(\psi_j - \langle\phi_j\rangle), \tag{4.24}$$

where C_ϕ is model constant usually taken as $C_\phi = 2.0$ and Ω is the mixing frequency that needs to be modelled separately. Finally, the last term in Eq. (4.22) represents the change of f_ϕ in the composition space due to reaction. We note that this term is closed, thus it does not require any modeling. Being the reaction term in the closed form makes the PDF model superior over the other turbulent combustion models.

4.2.2 Joint Velocity and Compositions PDF Modeling in the RANS Context

In the joint PDF of compositions modeling, the term $\langle u'|\boldsymbol{\psi}\rangle$ has to be modelled separately, thus the chemical compositions and the flow velocity are treated by distinct models. However the velocity and compositions have strong correlations in the RANS context [53]. To overcome these shortcomings, the joint velocity and compositions PDF $f_{\boldsymbol{u\phi}}(\boldsymbol{u},\boldsymbol{\psi};\boldsymbol{x},t)$ model has been developed [58].

The one-point, one-time, mass-weighted Eulerian joint PDF of velocity and compositions at location $\boldsymbol{x}$ and time t is defined as

$$\langle\rho\rangle\, f_{\boldsymbol{u\phi}}(\boldsymbol{u},\boldsymbol{\psi};\boldsymbol{x},t) \equiv \rho(\boldsymbol{\psi})\,\langle\delta(\boldsymbol{v}-\boldsymbol{u})\delta(\boldsymbol{\psi}-\boldsymbol{\phi})\rangle\,, \tag{4.25}$$

where ρ is the density, and $\boldsymbol{\psi} = (\psi_1, \psi_2, ...\psi_{n_\phi},)$ and $\boldsymbol{v} = (v_1, v_2, v_3)$ are the sample space variables of the compositions and velocity, respectively. The delta functions

$\delta(\boldsymbol{\psi}-\boldsymbol{\phi})$ and $\delta(\boldsymbol{v}-\boldsymbol{u})$ are the fine-grained PDFs of the compositions and velocity, respectively. The exact transport equation of the mass-weighted joint PDF of velocity and compositions can be derived directly from the conservation equations using the standard techniques and given by [58]

$$\begin{aligned}\langle\rho\rangle \frac{\partial f_{\boldsymbol{u\phi}}}{\partial t}+\langle\rho\rangle V_i \frac{\partial f_{\boldsymbol{u\phi}}}{\partial x_i}-\frac{\partial\langle p\rangle}{\partial x_i}\frac{\partial f_{\boldsymbol{u\phi}}}{\partial V_i}=\frac{\partial}{\partial V_i}\left[\left\langle\left(-\frac{\tau_{ij}}{\partial x_j}+\frac{\partial p'}{\partial x_i}\right)\middle|\boldsymbol{V},\boldsymbol{\psi}\right\rangle f_{\boldsymbol{u\phi}}\right] \\ +\frac{\partial}{\partial\psi_j}\left[f_{\boldsymbol{u\phi}}\left\langle\frac{\partial J_i^j}{\partial x_i}\middle|\boldsymbol{V},\boldsymbol{\psi}\right\rangle\right]-\frac{\partial}{\partial\psi_j}\left(\langle\rho\rangle f_{\boldsymbol{u\phi}}\dot{\omega}_{\phi_j}\right).\end{aligned} \tag{4.26}$$

The terms on the left-hand side represent rate of change in time, transport in physical space by both mean and fluctuating components of velocity, transport in velocity space by the mean pressure gradient, respectively. All the terms on the left hand side appear to be in the closed form. The first term on the right-hand side represents transport in the velocity space due to the molecular viscosity and the gradient of the fluctuating pressure conditional upon the event $\boldsymbol{u}=\boldsymbol{v}$ and $\boldsymbol{\phi}=\boldsymbol{\psi}$. This term is in the unclosed form and needs to be modeled. The Langevin models are widely used for this purpose. For instance, the simplified Langevin model [59] is given as

$$\begin{aligned}\left\langle\left(-\frac{\tau_{ij}}{\partial x_j}+\frac{\partial p'}{\partial x_i}\right)\middle|\boldsymbol{V},\boldsymbol{\psi}\right\rangle f_{\boldsymbol{u\phi}}=\left(\frac{1}{2}+\frac{3}{4}C_0\right)\Omega\left(V_i-\langle U_i\rangle\right)f_{\boldsymbol{u\phi}} \\ +\frac{1}{2}C_0 k\Omega\frac{f_{\boldsymbol{u\phi}}}{\partial V_i},\end{aligned} \tag{4.27}$$

where C_0 is the model constant usually taken as $C_0=2.1$, Ω is the turbulent frequency that needs to be modeled separately, and k is the turbulent kinetic energy. The second term represents the change of $f_{\boldsymbol{u\phi}}$ in the compositions space due to molecular mixing conditional upon the event $\boldsymbol{u}=\boldsymbol{v}$ and $\boldsymbol{\phi}=\boldsymbol{\psi}$. This term is also unclosed and can be modeled by assuming that the mixing is independent of the velocity, i.e.,

$$f_{\boldsymbol{u\phi}}\left\langle\frac{\partial J_i^j}{\partial x_i}\middle|\boldsymbol{V},\boldsymbol{\psi}\right\rangle=f_{\boldsymbol{u\phi}}\left\langle\frac{\partial J_i^j}{\partial x_i}\middle|\boldsymbol{\psi}\right\rangle. \tag{4.28}$$

Then the molecular mixing are modelled using mixing models such as the IEM model as discussed in the previous section i.e., Eq. (4.24). Finally, the last term in Eq. (4.26) represents the change of $f_{\boldsymbol{u\phi}}$ in composition space due to the reaction and it is also in the closed form.

4.2.3 Joint Compositions PDF Modeling in the LES Context

The joint PDF of the compositions, $f(\boldsymbol{\psi; x, t})$, in the LES context is defined as the one-point, one-time mass density joint PDF of compositions conditioned on the resolved velocity field, $\tilde{\boldsymbol{u}}$, which can be defined as

$$f(\boldsymbol{\psi}; \boldsymbol{x}, t) \equiv \int_{-\infty}^{\infty} \rho(\boldsymbol{y, t}) \delta(\boldsymbol{\psi} - \boldsymbol{\phi}(\boldsymbol{y}, t)) G(\boldsymbol{y} - \boldsymbol{x}) d\boldsymbol{y}, \tag{4.29}$$

where δ is an N-dimensional delta function of components, and $\boldsymbol{\psi}$ is the sample space variable for the compositions. G is high-pass filter satisfying the condition

$$\int G(\boldsymbol{y} - \boldsymbol{x}) d\boldsymbol{y} = 1, \ \forall \boldsymbol{x}. \tag{4.30}$$

Applying the filter to the density field results in

$$\bar{\rho} = \int \rho G(\boldsymbol{y} - \boldsymbol{x}) d\boldsymbol{y}, \tag{4.31}$$

where ρ and $\bar{\rho}$ are the instantaneous and the filtered (resolved) density fields, respectively. Note that, the joint PDF of compositions in the LES context is obtained by filtering the fine-grained PDF of the compositions. The mass density function f has the following properties [53]

$$f(\boldsymbol{\psi}; \boldsymbol{x}, t) \geq 0, \tag{4.32}$$

$$\int f(\boldsymbol{\psi}; \boldsymbol{x}, t) d\boldsymbol{\psi} = \bar{\rho}, \tag{4.33}$$

and for any flow properties ϕ,

$$\int \phi(\boldsymbol{\psi}, \boldsymbol{x}, t) f(\boldsymbol{\psi}; \boldsymbol{x}, t) d\boldsymbol{\psi} = \overline{\rho\phi(\boldsymbol{x}, t)} = \bar{\rho}\tilde{\phi}(\boldsymbol{x}, t), \tag{4.34}$$

where $\tilde{\phi}$ is the Favre-filtered (resolved) property. Then the transport equation for the compositions joint PDF in the LES context can be derived from the definition of the joint PDF, Eq. (4.29), and the conservation equations using the standard techniques [34, 29], and is given by

$$\frac{\partial f}{\partial t} + \frac{\partial \tilde{u}_i f}{\partial x_i} + \frac{\partial \left(\widetilde{u''|\boldsymbol{\psi}}\right) f}{\partial x_i} = \frac{\partial}{\partial \psi_j}\left[\frac{f}{\bar{\rho}}\left(\overline{\left.\frac{\partial J_i^j}{\partial x_i}\right| \boldsymbol{\psi}}\right)\right] + \frac{\partial}{\partial \psi_j}\left[f S_j(\boldsymbol{\psi})\right]. \tag{4.35}$$

The last term in Eq. (4.35) represents the change of f in the compositions space due to the reaction, and it is in the closed form. The first two terms on the left-hand side represent the rate of change following the filtered (resolved) flow. The last term on the left-hand side represents the transport of f in the physical space due to the small-scale (unresolved) velocity $u'' = u - \tilde{u}$ where the term of $\widetilde{u''|\boldsymbol{\psi}}$ is the mean of unresolved velocity conditional upon the event $\boldsymbol{\phi} = \boldsymbol{\psi}$ and appears to be unclosed. This term is usually modelled by the gradient diffusion assumption as

$$\bar{\rho}\left(\widetilde{u_i''|\boldsymbol{\psi}}\right) f = -\tilde{D}_T \frac{\partial f}{\partial x_i}. \tag{4.36}$$

The first term on the right-hand side of Eq. (4.35) represents the change of f in the compositions space due to the molecular mixing and J_i^j is the molecular diffusion term. First using the binary flux approximation for the molecular diffusion flux, J_i^j can be approximated as

$$J_i^j = -\rho D \frac{\partial \phi_j}{\partial x_i}. \tag{4.37}$$

Then the conditional diffusion term is modelled as [60]

$$\frac{1}{\bar{\rho}}\overline{\frac{\partial}{\partial x_i}\left(\rho D\frac{\partial \phi_j}{\partial x_i}\right)\Bigg|\boldsymbol{\psi}} = -\Omega\left(\psi_j - \tilde{\phi}_j\right) + \frac{1}{\bar{\rho}}\frac{\partial}{\partial x_i}\left(\bar{\rho}\tilde{D}\frac{\partial \tilde{\phi}_j}{\partial x_i}\right), \tag{4.38}$$

where the first term on the right hand side represents the interaction by exchange with the mean (IEM) mixing model [57] and the second term is the mean drift term [60]. In Eq. (4.38), Ω denotes the scalar mixing frequency and it can be modelled as

$$\Omega = C_\phi \frac{\widetilde{D} + \widetilde{D}_T}{\Delta^2}, \tag{4.39}$$

where C_ϕ is a model constant determined by the sensitivity study on the statistics obtained by the simulations, and Δ is the LES filter size. We note that, in the RANS context, the joint PDF of compositions is defined as the mean of the fine-grained PDF of composition whereas the joint PDF of compositions is defined as the filtered fine-grained PDF of compositions in the LES context.

4.3 LES/PDF Modeling of Turbulent Reacting Flows

In the LES context, the fields in the turbulent reacting flows are separated into the large (resolved) and small (unresolved) scales by applying a high band-pass filtering operation. For example, the density field ρ in a turbulent flow is decomposed as

$$\rho = \bar{\rho} + \rho'', \tag{4.40}$$

where $\bar{\rho}$ and ρ'' are the filtered (resolved) and the subgrid (unresolved) parts of the density field, respectively. For a given field ϕ in a turbulent flow, the Favre-filtered field $\tilde{\phi}$ can be defined as

$$\tilde{\phi} = \frac{1}{\bar{\rho}}\int \rho\phi G(\boldsymbol{y} - \boldsymbol{x})d\boldsymbol{y}. \tag{4.41}$$

As introduced in Section 4.2.3, the Favre-filtered fields can be obtained from the

PDF as

$$\tilde{\boldsymbol{\phi}}(\boldsymbol{x},t) = \frac{1}{\bar{\rho}} \int \boldsymbol{\phi}(\boldsymbol{\psi},\boldsymbol{x},t) f(\boldsymbol{\psi};\boldsymbol{x},t) d\boldsymbol{\psi}, \tag{4.42}$$

where $\boldsymbol{\phi} = \{Y_1, Y_2, ..., Y_N, h\}$ where Y_i is the mass fraction of i^{th} composition, h is the enthaply and N is the number of species, $f(\boldsymbol{\psi};\boldsymbol{x},t)$ is the one-point, one-time mass density joint PDF of compositions conditioned on the resolved velocity field, $\tilde{\boldsymbol{u}}$, as discussed in Section 4.2.3. Additionally, the resolved density field $\bar{\rho}$ is obtained as

$$\bar{\rho} = \int f(\boldsymbol{\psi};\boldsymbol{x},t) d\boldsymbol{\psi}. \tag{4.43}$$

Then, the governing equations for the filtered mass and momentum can be directly derived by applying filtering operations to the instantaneous equations of mass and momentum, i.e., Eqs. (2.1) and (2.2). The resulting evolution equations for the filtered mass and momentum are summarized here and details can be found in the standard textbooks such as [12], and are written as

$$\frac{\partial \bar{\rho}}{\partial t} + \frac{\partial \bar{\rho}\tilde{u}_i}{\partial x_i} = 0, \tag{4.44}$$

$$\frac{\partial \bar{\rho}\tilde{u}_i}{\partial t} + \frac{\partial \bar{\rho}\tilde{u}_i\tilde{u}_j}{\partial x_j} = -\frac{\partial \bar{p}}{\partial x_i} + \frac{\partial \tau_{ij}}{\partial x_j} + \frac{\partial T_{ij}}{\partial x_j}, \tag{4.45}$$

where τ_{ij} is the resolved viscous stress tensor given by

$$\tau_{ij} = \tilde{\mu}\left(\frac{\partial \tilde{u}_i}{\partial x_j} + \frac{\partial \tilde{u}_j}{\partial x_i} - \frac{2}{3}\frac{\partial \tilde{u}_k}{\partial x_k}\delta_{ij}\right) = 2\tilde{\mu}\tilde{S}_{ij}, \tag{4.46}$$

and $T_{ij} = \bar{\rho}\tilde{u}_i\tilde{u}_j - \bar{\rho}\widetilde{u_i u_j}$ is the subfilter stresses, and is often modelled by the Boussinesq eddy viscosity assumption [61], i.e.,

$$T_{ij} = \bar{\rho}\tilde{u}_i\tilde{u}_j - \bar{\rho}\widetilde{u_i u_j} = 2\tilde{\mu}_t\tilde{S}_{ij} - \frac{2}{3}\bar{\rho}q^2\delta_{ij}, \tag{4.47}$$

where $\tilde{S}_{ij}$ is the resolved strain rate defined as

$$\tilde{S}_{ij} = \frac{1}{2}\left(\frac{\partial \tilde{u}_i}{\partial x_j} + \frac{\partial \tilde{u}_j}{\partial x_i} - \frac{2}{3}\delta_{ij}\frac{\partial \tilde{u}_k}{\partial x_k}\right). \tag{4.48}$$

In Eq. (4.47), q^2 is the subgrid kinetic energy defined

$$q^2 = \frac{1}{2}\left(\tilde{u}_k\tilde{u}_k - \widetilde{u_k^2}\right). \tag{4.49}$$

Note that the subgrid kinetic energy, q^2, is the isotropic part of the residual stress, and it can be absorbed in the pressure and thus needs not to be modelled in low Mach number flows [62]. In Eq. (4.47), $\tilde{\mu}_t$ is the turbulent eddy viscosity. Using the Smagorinsky model [63], it is given by

$$\tilde{\mu}_t = C_\mu \bar{\rho}\Delta^2|\tilde{S}|, \text{ where } |\tilde{S}| = \sqrt{\tilde{S}_{ij}\tilde{S}_{ij}}, \tag{4.50}$$

where Δ is the filter width. The model coefficient C_μ is computed using the dynamic Smagorinsky model proposed by Moin et al. [62] as

$$C_\mu = \frac{\langle \mathcal{L}_{ij}\mathcal{M}_{ij}\rangle_{sgs}}{\langle \mathcal{M}_{kl}\mathcal{M}_{kl}\rangle_{sgs}}, \tag{4.51}$$

where $\mathcal{L}$ is called the Leonard term [64] and is defined as

$$\mathcal{L}_{ij} = (\widehat{\bar{\rho}\tilde{u}_i\tilde{u}_j}) - \frac{1}{\hat{\bar{\rho}}}(\widehat{\bar{\rho}\tilde{u}_i}\widehat{\bar{\rho}\tilde{u}_j}). \tag{4.52}$$

$\mathcal{M}$ is a model term given by

$$\mathcal{M}_{ij} = 2\hat{\bar{\rho}}\hat{\Delta}^2|\hat{\tilde{S}}|^2 - 2\Delta^2\widehat{\bar{\rho}|\tilde{S}|^2}. \tag{4.53}$$

In Eqs. (4.52) and (4.53), the terms with caret ($\widehat{\cdot}$) are the test-filtered quantities, and $\hat{\Delta}$ denotes the test-filter width typically taken as double the size of the LES filter, Δ, i.e., $\hat{\Delta} = 2\Delta$. In Eq. (4.51), the operator $\langle\cdot\rangle_{sgs}$ is an averaging operator

over $\mathcal{L}_{ij}\mathcal{M}_{ij}$ and $\mathcal{M}_{kl}\mathcal{M}_{kl}$, and is used to ensure the numerical stability. The average could be taken over the whole computational domain or over a small vicinity. In this work, we use the Lagrangian averaging method proposed by Meneveau [65]. In this method, two transport equations are solved to evolve the Lagrangian averages, $\mathcal{F}_{LM} = \langle \mathcal{L}_{ij}\mathcal{M}_{ij} \rangle_{Lagrangian}$ and $\mathcal{F}_{MM} = \langle \mathcal{M}_{kl}\mathcal{M}_{kl} \rangle_{Lagrangian}$. The transport equations for $\mathcal{F}_{LM}$ and $\mathcal{F}_{MM}$ are are given by

$$\frac{\partial(\bar{\rho}\mathcal{F}_{LM})}{\partial t} + \frac{\partial(\bar{\rho}\tilde{u}_i\mathcal{F}_{LM})}{\partial x_i} = \frac{\bar{\rho}}{T_{relax}} \left(\mathcal{L}_{ij}\mathcal{M}_{ij} - \mathcal{F}_{LM} \right), \tag{4.54}$$

and

$$\frac{\partial(\bar{\rho}\mathcal{F}_{MM})}{\partial t} + \frac{\partial(\bar{\rho}\tilde{u}_i\mathcal{F}_{MM})}{\partial x_i} = \frac{\bar{\rho}}{T_{relax}} \left(\mathcal{M}_{ij}\mathcal{M}_{ij} - \mathcal{F}_{MM} \right), \tag{4.55}$$

where T_{relax} is the relaxation time scale evaluated as

$$T_{relax} = \theta \ \Delta \ (\bar{\rho})^{1/2} \left(\mathcal{F}_{LM}\mathcal{F}_{MM} \right)^{-1/8}, \text{ where } \theta = 1.5. \tag{4.56}$$

The model coefficient C_μ is then obtained as

$$C_\mu = \frac{\mathcal{F}_{LM}}{\mathcal{F}_{MM}}. \tag{4.57}$$

The turbulent diffusivity, $\widetilde{D}_T$, is calculated from the turbulent eddy viscosity as

$$\bar{\rho}\widetilde{D}_T = \frac{\widetilde{\mu}_T}{Sc_T}, \tag{4.58}$$

where Sc_T is the turbulent Schmidt number taken as $S_c = 0.4$ [66]. The molecular viscosity, $\tilde{\mu}$, and the molecular diffusivity, $\widetilde{D}$, are approximated by an empirical fit to the laminar flame calculations as $\widetilde{\mu}/\bar{\rho} = a_0(\tilde{T}/T_0)^{b_1}$ and $\widetilde{D} = a_0 c_0 (\tilde{T}/T_0)^{b_2}$ where $\tilde{T}$ is the resolved temperature. In this study we select the coefficients as $a_0 = 2.22 \times 10^{-5}$ m^2/s, $b_1 = 1.658$, $b_2 = 1.77$, $c_0 = 1.22$ and $T_0 = 300\mathrm{K}$ based on a laminar flame calculation performed using the CHEMKIN library for a methane/air combustion

with the GRI 2.11 mechanism [40].

4.4 Solution Methodology for the LES/PDF Model Equations

In the LES/PDF modeling of the turbulent reacting flows, the complete set of the modelled filtered conservation and joint PDF equations can be written as

$$\frac{\partial \bar{\rho}}{\partial t} + \frac{\partial \bar{\rho}\tilde{u}_i}{\partial x_i} = 0, \tag{4.59}$$

$$\frac{\partial \bar{\rho}\tilde{u}_i}{\partial t} + \frac{\partial \bar{\rho}\tilde{u}_i\tilde{u}_j}{\partial x_j} = -\frac{\partial \bar{p}}{\partial x_i} + 2\frac{\partial}{\partial x_j}\left(\tilde{\mu}_{eff}\tilde{S}_{ij}\right), \tag{4.60}$$

$$\begin{aligned}\frac{\partial f}{\partial t} + \frac{\partial \tilde{u}_i f}{\partial x_i} =& -\frac{\partial}{\partial x_i}\left(\frac{\tilde{D}_T}{\bar{\rho}}\frac{\partial f}{\partial x_i}\right) + \frac{\partial}{\partial \psi_\alpha}(f\Omega(\psi_\alpha - \widetilde{\phi}_\alpha)) \\ & - \frac{\partial}{\partial \psi_\alpha}\left(f\frac{1}{\bar{\rho}}\frac{\partial}{\partial x_i}\left(\bar{\rho}\tilde{D}\frac{\partial \tilde{\phi}_\alpha}{\partial x_i}\right)\right) + \frac{\partial}{\partial \psi_\alpha}\left(fS_\alpha(\boldsymbol{\psi})\right).\end{aligned} \tag{4.61}$$

where $\tilde{\mu}_{eff} = \tilde{\mu} + \tilde{\mu}_T$. The filtered density used in Eqs. (4.59) and (4.60) is obtained from the joint PDF of compositions as

$$\bar{\rho}(\boldsymbol{x}, t) = \int f(\boldsymbol{\psi}; \boldsymbol{x}, \boldsymbol{t}) d\boldsymbol{\psi}. \tag{4.62}$$

The filtered pressure field can be computed from the Poisson equation in the form

$$\frac{\partial^2 \bar{p}}{\partial x_i x_i} = \frac{\partial^2 \bar{\rho}}{\partial t^2} - \frac{\partial^2 \bar{\rho}\tilde{u}_i\tilde{u}_j}{\partial x_i \partial x_j} + 2\frac{\partial^2 \tilde{\mu}_{eff}\tilde{S}_{ij}}{\partial x_i \partial x_j}, \tag{4.63}$$

which is obtained by taking divergence of the filtered momentum equations and using the filtered mass conservation equation.

The filtered conservation of mass and momentum equations, Eqs. (4.59) and (4.60), and the Poisson equation for the pressure can be solved numerically by conventional methods such as finite volume or finite difference techniques. However, the transport equation for the joint PDF of compositions requires a special treatment due

to its high dimensionality. The dimensions of Eq. (4.61) is the sum of the number of species and enthalpy and three-dimensions for physical space and one-dimension for time, i.e., Eq. (4.61) evolves in $N_s + 4$ dimensional space where N_s is the number of species plus enthalpy. Considering the large number of species involved in a typical combustion problem, the transport equation of the joint PDF (Eq. (4.61)) cannot be solved using the conventional techniques such as finite volume or finite difference because the computational cost increases exponentially with the number of dimensions in these methods.

Pope proposed [9] an alternative solution methodology based on the Monte Carlo method in the Lagrangian point of view for the joint PDF equation. In this approach, the flow is represented by a large number of notional Lagrangian particles. Then a set of stochastic differential equations are constructed that govern the evaluation of particle properties in such a way that the particles exhibit the same joint PDF as the one obtained from the solution of the modeled joint PDF transport equation. The models for the particle position and compositions are given by [9]

$$dX_j^* = \left[\tilde{u}_j + \frac{1}{\bar{\rho}}\frac{\partial(\bar{\rho}\widetilde{D}_T)}{\partial x_j}\right]^* dt + \left[2\widetilde{D}_T^*\right]^{1/2} dW_j^*, \tag{4.64}$$

$$d\phi_\alpha^* = -\Omega^*(\phi_\alpha^* - \tilde{\phi}_\alpha^*)dt + \left[\frac{1}{\bar{\rho}}\frac{\partial}{\partial x_j}\left(\bar{\rho}\widetilde{D}\frac{\partial\tilde{\phi}_\alpha}{\partial x_j}\right)\right]^* dt + S_\alpha(\boldsymbol{\phi}^*)dt, \tag{4.65}$$

where the term $d\boldsymbol{W}^*$ denotes the Wiener increment. Equation (4.64) evolves the particles in the physical space while Eq. (4.65) evolves the particles in the composition space. The terms on the right-hand side of Eq.(4.65) represent the evolution of compositions due to turbulent and molecular diffusions, and chemical reactions, respectively. The superscript "*" denotes the Lagrangian particle properties or the LES fields evaluated at the particle locations. Here, we note that the statistics obtained from the particle equations, Eqs. (4.64, 4.65), are identical to those obtained from the modeled joint PDF equation, i.e., Eq. (4.61). The mean field can be obtained

from the particle properties. For instance,

$$\tilde{\phi} = \frac{\langle m^* \phi^* \rangle}{\langle m^* \rangle}, \tag{4.66}$$

which approximates

$$\tilde{\phi} = \frac{1}{\bar{\rho}} \int_{\psi} \phi d\psi, \tag{4.67}$$

where $\langle \cdot \rangle$ denotes a summation over the particles in a given cell.

The resulting solution methodology is composed of two main components: (i) An Eulerian numerical method for solving the filtered conservation equations for the mass and momentum (from now on we refer it as the LES solver). (ii) A Lagrangian Monte Carlo method for the transport equation for the joint PDF of compositions (from now on we refer it as the PDF solver). The LES and the PDF solvers together form the hybrid LES/PDF solver to be used for the simulations of the turbulent reacting flows.

4.4.1 The Hybrid LES/PDF solver

The main roles of the LES and PDF components can be summarized as:

1. The LES solver explicitly calculates the large-scale turbulent motions and provides the filtered velocity and pressure fields to the PDF solver.

2. The PDF algorithm solves the modeled evolution equation of the joint compositions PDF and provides the filtered density field (or quantities needed to compute the filtered density field) to the LES solver.

The LES solver calculates the velocity, $\tilde{u}_i$, and pressure, $\bar{p}$, fields by solving Eqs. (4.59), (4.60) and (4.63). In addition, the LES method also calculates the turbulent viscosity $\tilde{\mu}_T$ and diffusivity $\tilde{D}_T$ as well as the mixing frequency Ω. The PDF solver evolves the particles in the physical and compositions spaces and calculates the filtered density $\bar{\rho}$, the Favre-filtered temperature $\tilde{T}$ and mass fractions $\tilde{Y}_i$.

In the LES solver, the filtered density, $\bar{\rho}$, is required to solve Eqs. (4.59), (4.60) and (4.63). Moreover, the Favre-filtered temperature, $\tilde{T}$, is required to obtain the molecular viscosity $\tilde{\mu}$, and diffusivity $\tilde{D}$ according to the empirical fit to laminar flame calculations. On the other hand, the PDF solver requires the fields of Favre-filtered velocity, $\tilde{u}_i$, the molecular and turbulent diffusivity, ($\tilde{D}$ and $\tilde{D}_T$), and the mixing frequency Ω in the particle equations, i.e., Eqs. (4.64) and (4.65). Therefore, the LES supplies the Favre-filtered velocity, $\tilde{u}_i$, the molecular and turbulent diffusivity, ($\tilde{D}$ and $\tilde{D}_T$), and the mixing frequency, Ω, fields to the PDF solver in each time step. In turns, the LES solver gets the filtered density $\bar{\rho}$ and the Favre-filtered temperature $\tilde{T}$ from the PDF solver. Figure 4.5 shows a schematic representation of the data transfer between the LES and PDF solvers in the hybrid method.

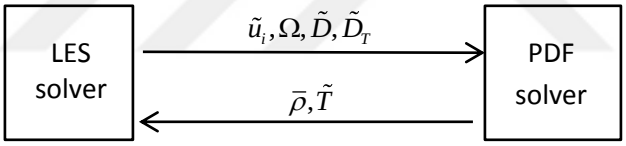

Figure 4.5: The schematic representation of the data transfer between the LES and PDF solvers.

While the data transfer from the LES solver to the PDF solver is usually performed by a trilinear interpolation, the filtered density feedback from the PDF solver to the LES solver is a challenging task due to the stochastic nature of the particle fields. The filtered fields obtained by the PDF solver contain the stochastic noise, thus using the noisy filtered density field directly in the LES solver is prone to cause a significant numerical instability problem. Note that this numerical instability is mainly caused by the term containing time derivative of the filtered density in the pressure equation.

To overcome this difficulty, we employ the transported specific volume (TSV) method developed by Popov et al. [67]. In the TSV method, the change in the resolved specific volume due to transport in the physical space (Eq. (4.64)) is calculated by the LES solver and the change due to turbulent mixing, molecular diffusion, and chemical reactions (the terms on the right hand side of Eq. (4.65), respectively) is calculated by

the PDF solver. For this purpose, the evolution equation for the specific volume, $\tilde{v}$, is derived from the modeled filtered joint PDF equation and augmented by a relaxation term, and the resulting equation can be written as

$$\bar{\rho}\frac{\partial\tilde{v}}{\partial t}+\bar{\rho}\frac{\partial\left(\tilde{u}_j\tilde{v}\right)}{\partial x_j}=\bar{\rho}\frac{\partial}{\partial x_j}\left(\widetilde{D}_T\frac{\partial\tilde{v}}{\partial x_j}\right)+S_v+\dot{\omega}_v, \tag{4.68}$$

where S_v is the source term defined as

$$S_v\equiv\left\{\frac{\langle\dot{v}^*\rangle}{\langle v^*\rangle}\right\}, \tag{4.69}$$

where $\langle\dot{v}\rangle$ is the weighted sum of the rate of change of particle specific volume in a given cell due to mixing, molecular diffusion, and chemical reaction, while $\langle v\rangle$ is the weighted sum of particle specific volume in the same cell. The last term on the right hand side of Eq. (4.68) is the relaxation term of the form

$$\dot{\omega}_v=\bar{\rho}\frac{\tilde{v}_{PDF}-\tilde{v}}{\tau}, \tag{4.70}$$

where $\tilde{v}_{PDF}$ is the specific volume obtained from the particles in the PDF method as follows

$$\tilde{v}_{PDF}=\left\{\frac{\langle m^*v^*\rangle}{\langle m^*\rangle}\right\}. \tag{4.71}$$

Here m^* and v^* are the mass and specific volume of particles, and τ is the relaxation time taken as $\tau=4\Delta t$ in this work. The resulting hybrid LES/PDF solver is schematically shown in Fig. 4.6. After successfully solving the transport equation for

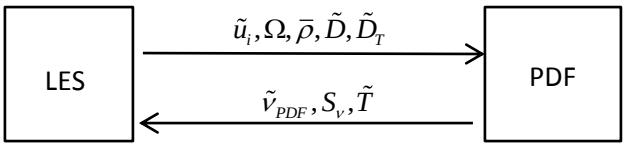

Figure 4.6: The TSV coupling of the LES and PDF algorithms in the hybrid LES/PDF method.

the specific volume, $\tilde{v}$, the filtered density field $\bar{\rho}$ used in the solution of the equation in the LES solver is obtained as

$$\bar{\rho} = \frac{1}{\tilde{v}}. \tag{4.72}$$

4.5 Calculation of Combustion Chemistry: In Situ Adaptive Tabulation Method

In the PDF method, the compositions of particles are advanced in the composition space by taking the turbulent mixing, molecular diffusion and chemical reactions into account. This can be written compactly as

$$\frac{d\phi(t)}{dt} = M(t) + S(\phi[t]), \tag{4.73}$$

where $M(t)$ denotes the rate of change due to mixing and molecular diffusion while $S(\phi[t])$ denotes the rate of change due to the chemical reactions. Equation (4.73) is solved by using a fractional time step method. In this approach, time integration is performed for the mixing and molecular diffusion as

$$\frac{d\phi(t)}{dt} = M(t), \tag{4.74}$$

then the integration is carried out for the change due to the chemical reaction as

$$\frac{d\phi(t)}{dt} = S(\phi[t]). \tag{4.75}$$

The details of the fractional time stepping method will be provided in the next section. In this section we only focus on the solution of Eq. (4.75).

Equation (4.75) is a system of highly non-linear stiff ordinary differential equations (ODEs) with a dimension of number of species plus enthalpy. The ODE system is stiff because of the wide disparity of the timescales of the chemical reactions that range from 10^{-9} s to 1 s in a typical combustion process [1]. The solution of Eq. (4.75) takes

the particle composition from $\phi^n = \phi(t_n)$ to $\phi^{n+1} = \phi(t_n + \Delta t)$ in the composition space, which is called the reaction mapping, $R(\phi^n)$ as schematically shown in Fig. 4.7.

Figure 4.7: The sketch of the reaction mapping $R(\phi^n)$ in composition space.

In calculation of the combustion chemistry with a detailed representation, the main task is to calculate the reaction mapping $R(\phi^n)$ for every Lagrangian particle at each time step where the sum of the particles is order of millions and the number of time steps is order of tens of thousands in a typical LES/PDF simulation. Therefore, considering the stiffness of the ODE system and the large number of particles, the calculations of the reaction mapping requires a huge computational cost making the simulations infeasible for practical engineering problems. To overcome this difficulty, Pope [1] has proposed a tabulation method in which the tabulation tables are created and grown during the simulation. The method is called In Situ Adaptive Tabulation (ISAT). In the ISAT method, a reaction mapping of a query point, $R(\phi^q)$, is approximated by a linearized mapping based on a tabulation point (ϕ^n) as

$$R(\phi^q) \approx R^l(\phi^q) \equiv R(\phi^n) + \delta R^l. \tag{4.76}$$

In Eq. (4.76), δR^l is defined as

$$\delta R^l \equiv A\delta\phi = \delta R + O(|\delta\phi|^2), \tag{4.77}$$

where A is the mapping gradient matrix given by

$$A_{ij}(\phi) \equiv \frac{\partial R_i(\phi)}{\partial \phi_j}, \tag{4.78}$$

and $\delta\phi$ is the displacement between tabulation point ϕ^n and the query point ϕ^q while δR is the displacement between the tabulation reacting mapping $R(\phi^n)$ and the mapping for the query point $R(\phi^q)$. Figure 4.8 shows a sketch for the mapping of a query point. For a query point ϕ^q close to the tabulation point ϕ^n, the local error is

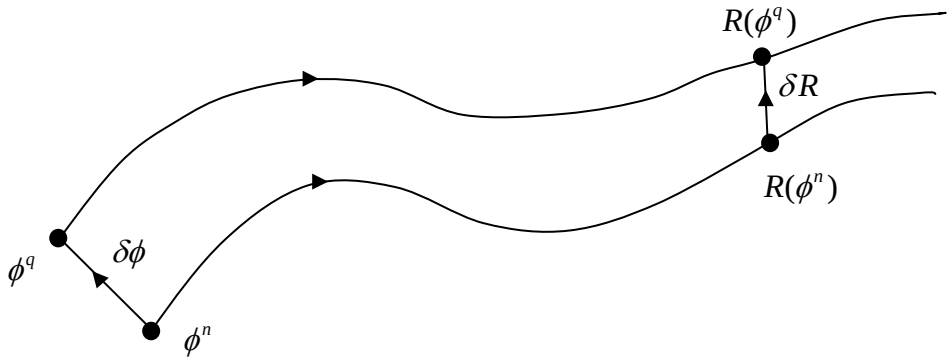

Figure 4.8: The sketch for the reaction mappings, $R(\phi^n)$ and $R(\phi^q)$, and the definitions of the displacements $\delta\phi$ and δR.

defined as

$$\varepsilon \equiv \left| B\left(R\left[\phi^q\right] - R^l\left[\phi^q\right]\right)\right| = \left| B\left(\delta R - \delta R^l\right)\right|, \tag{4.79}$$

where $\boldsymbol{B}$ is a scaling matrix. The local error defined by Eq. (4.79) is the exact local error introduced by the linearized mapping. The calculation of the local error in Eq. (4.79) requires the calculation of the reaction mapping of the query point. However,

the calculation of the reaction mapping for each query point eliminates the advantage of tabulation methods. Thus, the local error can be approximated by considering a constant approximation instead of linear approximation for the mapping. Considering a constant approximation, the reaction mapping for a query point can be written as

$$R(\phi^q) \approx R^c(\phi^q) \equiv R(\phi^n). \tag{4.80}$$

Consequently the corresponding local error is

$$\varepsilon_c \equiv |B\left(R\left[\phi^q\right] - R^c\left[\phi^q\right]\right)| = |B\left(R\left[\phi^q\right] - R\left[\phi^n\right]\right)|. \tag{4.81}$$

From Eqs. (i.e., 4.76), (4.77) and (4.81), the corresponding local error can be written as

$$\varepsilon_c = |BA\delta\phi|. \tag{4.82}$$

The region of accuracy of a tabulation point ϕ^n consists of the query points whose local errors are smaller than a given error tolerance ε_{tol}. The region of accuracy is chosen to be a hyper-ellipsoid, called as the ellipsoid of accuracy (EOA) which is schematically shown in Fig. 4.9.

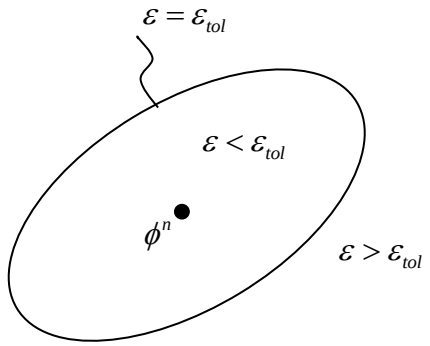

Figure 4.9: The sketch of the ellipsoid of accuracy of the query point ϕ^n.

For a given query point ϕ^q, ISAT performs the following operations to evaluate the reaction mapping for ϕ^q:

1. Estimate the local error of ϕ^q, ε_c, using Eq. (4.82).

2. If the local error ε_c is smaller than the speficied error tolerans ε_{tot}, i.e., ϕ^q is within the EOA. Then the reaction mapping is approximated as

$$R^l(\phi^q) = R(\phi^n) + A(\phi^n)(\phi^q - \phi^n). \tag{4.83}$$

   Returning $R^l(\phi^q)$ completes the ISAT algorithm. This is called as *retrieving* (R).

3. If the local error ε_c is greater than the speficied error tolerans ε_{tot}, then perform direct integration and evaluate the reaction mapping $R(\phi^q)$.

4. The local error is measured by Eq. (4.77) ($\varepsilon = |B\left(R\left[\phi^q\right] - R\left[\phi^n\right]\right)|$). If the measured local error is smaller than the specified error tolerance, than the EOA is grown to include the query point ϕ^q. The growth of the EOA is represented in Fig. 4.10. This process is called as *growth* (G).

5. If the local error calculated at the previous step is greater than the specified error tolerance, ISAT adds $\{\phi^q, R(\phi^q)$ and $A(\phi^q)\}$ as a new record to the tabulation tables. This process is called as *addition* (A).

6. After the growth and addition steps (steps 4 and 5), ISAT returns $R(\phi^q)$.

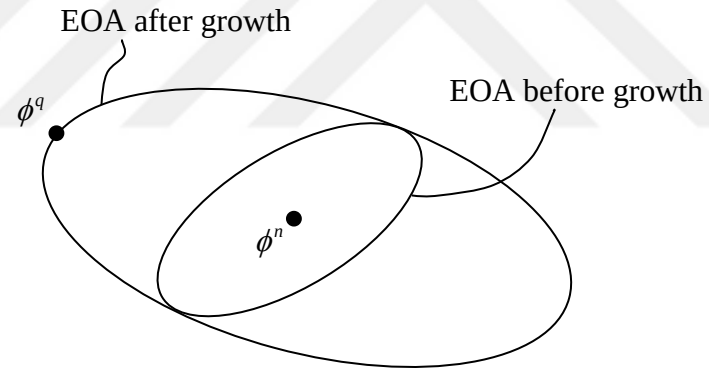

Figure 4.10: The sketch of the growth of the ellipsoid of accuracy to include ϕ^q.

Chapter 5

NUMERICAL METHOD

The numerical methods used to solve the governing equations in the LES/PDF method are discussed in this chapter. First we present the methods used in the LES solver. The spatial discretization of the transport equations, the time integration, and the velocity-pressure coupling are described. In the Lagrangian Monte Carlo particle method, the fractional time integration algorithm and the numerical methods for the particle tracking, mean estimation from the particles, and interpolation back on the particles are discussed. Finally, the three-stage velocity correction method for the Lagrangian particles is presented.

5.1 The LES solver

The LES method solvers the filtered conservation equations for the mass and momentum by using a finite volume method. In this section, we present the discretization of the mass and momentum equations in space and time. Then, the iterative solution procedure and velocity-pressure coupling method are discussed.

5.1.1 The Finite Volume Method

In the finite volume method, the computational domain is discretized by control volumes (CV) which do not overlap and completely fill the computational domain. All vector and scalar fields are located at the cell centers. In this approach, the numerical solution for the conservation equations is seeked at the computational points $\boldsymbol{P}$ located at the center of the control volume as sketched in Fig. 5.1. The cell center point $\boldsymbol{x_P}$ of a control volume V_P is defined as the center of the mass of the cell and

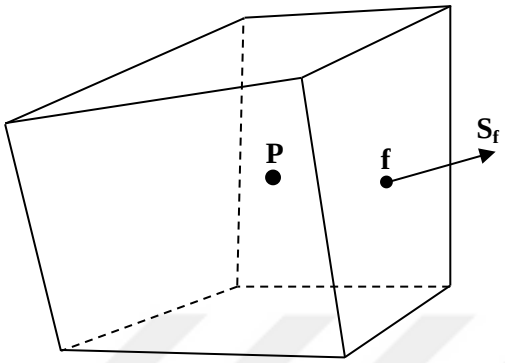

Figure 5.1: A typical computational cell used in the FV method. $\boldsymbol{P}$ denotes the cell center, i.e., the center of mass while $\boldsymbol{f}$ is the center of the face. $\boldsymbol{S_f}$ is the outward pointing face area vector defined as $\boldsymbol{S_f} = S_f \boldsymbol{n}$ where S_f is the surface area of the face and $\boldsymbol{n}$ is the unit vector.

is given by

$$\int_{V_p} (\boldsymbol{x} - \boldsymbol{x_P})\, dV = 0. \tag{5.1}$$

Each control volume is surrounded by flat faces such that each face is shared only by two control volumes. The filtered equation can be written in the general form of a transport equation as

$$\frac{\partial \rho\phi}{\partial t} + \frac{\partial \rho u_i \phi}{\partial x_i} - \frac{\partial}{\partial x_i}\left(\rho D \frac{\partial \phi}{\partial x_i}\right) = S_\phi, \tag{5.2}$$

where ϕ is a flow property, D is diffusion coefficient and S_ϕ is the source term. In the finite volume method, Eq. (5.2) is satisfied in a control volume V_P around the point $\boldsymbol{P}$ as

$$\int_t^{t+\Delta t} \left[\frac{\partial}{\partial t}\int_{V_P} \rho\phi dV + \int_{V_P} \frac{\partial \rho u_i \phi}{\partial x_i} dV - \int_{V_P} \frac{\partial}{\partial x_i}\left(\rho D \frac{\partial \phi}{\partial x_i}\right) dV\right] dt = \int_t^{t+\Delta t} \left[\int_{V_P} S_\phi dV\right] dt \tag{5.3}$$

Using the Gauss' theorem, the convective terms (i.e., the second term on the left-hand side) can be written as

$$\int_{V_P} \frac{\partial \rho u_i \phi}{\partial x_i} dV = \int_S (\rho u_i \phi)\, n_i dS = \sum_f S_{fi} \left(\rho u_i \phi\right)_f$$
$$\cong \sum_f S_{fi} \left(\rho u_i\right)_f \phi_f = \sum_f F \phi_f \tag{5.4}$$

where the index f denotes the index of the face of the control volume, S_i is the i^{th} component of the surface area vector of the face f, and $F = S_i \left(\rho u_i\right)_f$ represents the mass flux through the face f, and ϕ_f is the value of ϕ at the cell face f. In Eq. (5.4), the fields are required to be evaluated on the cell faces. The values on the faces are calculated by interpolating the values from the cells sharing the face f as schematically shown in Fig. 5.2 using the basis function as

$$\phi_f = w_P \phi_P + w_N \phi_N, \tag{5.5}$$

where P and N are the indices of the cells sharing the face f. In Eq. (5.5), w_P and w_N are the basis functions of the cells calculated as

$$w_P = \frac{|\boldsymbol{fN}|}{|\boldsymbol{PN}|}, \tag{5.6}$$

and

$$w_N = 1 - w_P, \tag{5.7}$$

where $|\boldsymbol{PN}|$ and $|\boldsymbol{fN}|$ are the distance between the cell center locations, and the distance between $\boldsymbol{N}^{nd}$ cell center location and the face center location $\boldsymbol{f}$.

Using the same procedure as the for the convective term, the diffusion term (the

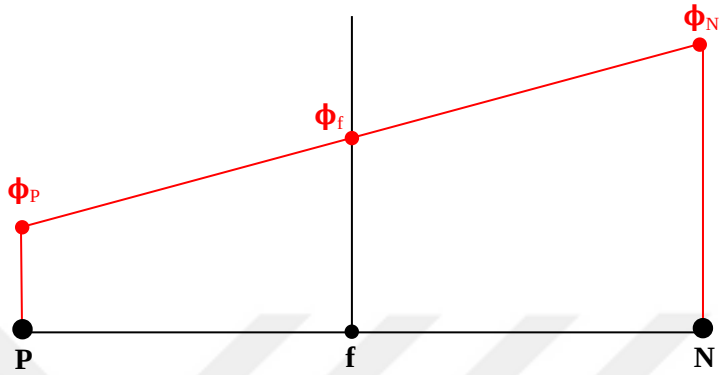

Figure 5.2: Face Interpolation. $\boldsymbol{P}$ and $\boldsymbol{N}$ are the cell center locations. $\boldsymbol{f}$ is the face center location.

third term on the left-hand side) can be approximated as

$$\int_{V_P} \frac{\partial}{\partial x_i}\left(\rho D \frac{\partial \phi}{\partial x_i}\right) dV = \sum_f S_i \left(\rho D \frac{\partial \phi}{\partial x_i}\right)_f = \sum_f (\rho D)_f \, S_i \left(\frac{\partial \phi}{\partial x_i}\right)_f . \tag{5.8}$$

We need to evaluate the gradient term $\frac{\partial \phi}{\partial x_i}$ on the cell faces. The simplest way is to first evaluate the gradient vectors at the cell centers and then interpolate to find the values at cell faces using the same basis functions as in Eq. (5.5). Thus we get

$$\left(\frac{\partial \phi}{\partial x_i}\right)_f = w_P \left(\frac{\partial \phi}{\partial x_i}\right)_P + w_N \left(\frac{\partial \phi}{\partial x_i}\right)_N , \tag{5.9}$$

where the gradient terms at the cell centers can be approximated as the volume averaged values, i.e.,

$$\begin{aligned} \left(\frac{\partial \phi}{\partial x_i}\right)_P &\cong \frac{1}{V_P}\int_{V_P} \frac{\partial \phi}{\partial x_i} dV \\ &= \frac{1}{V_P}\int_S \phi dS_i \cong \frac{\partial \phi}{\partial x_i}\sum_f S_i \phi_f, \end{aligned} \tag{5.10}$$

where the divergence theorem has been used to convert the volume integral into the

surface integral. An alternative way of computing the gradient term at cell faces is

$$\left(\frac{\partial \phi}{\partial x_i}\right)_f \cong |\boldsymbol{S}| \frac{\phi_N - \phi_P}{|\boldsymbol{d}|}, \tag{5.11}$$

where $\boldsymbol{d}$ is the displacement vector between the cell centers $\boldsymbol{P}$ and $\boldsymbol{N}$ as shown in Fig. 5.3. Although both of the method Eq. (5.9) and Eq. (5.11) are second-order

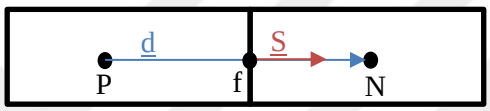

Figure 5.3: $\boldsymbol{d}$ denotes the displacement vector between cell center $\boldsymbol{P}$ and $\boldsymbol{N}$, $\boldsymbol{S}$ is the surface are vector.

accurate the first method uses larger computational molecule, thus the first term of the truncation error is bigger than that of the latter method. However, the second method cannot be used in non-orthogonal grids [68]. In this study, the first method is employed.

The term on the right-hand side of Eq. (5.2) is a source term which can be a general function of ϕ. The source term can be approximated by linearizing it as follows:

$$S_\phi(\phi) \cong S_u + S_p \phi, \tag{5.12}$$

where S_u and S_p are the linearization coefficients. Then the integral over the compu-

tational domain can then be written as

$$\begin{aligned}\int_{V_P} S_\phi(\phi)dV &\cong \int_{V_P} (S_u + S_p\phi)\, dV \\ &= \int_{V_P} S_u dV + \int_{V_P} S_p\phi dV \\ &= S_u V_P + S_p \int_{V_P} [\phi_P + (\boldsymbol{x} - \boldsymbol{x_P}) \cdot (\nabla\phi)_P]\, dV \\ &= S_u V_P + S_p\phi_P V_P + \underbrace{\left[\int_{V_P} (\boldsymbol{x} - \boldsymbol{x_P})dV\right]}_{=0} \cdot (\nabla\phi)_P \\ &= S_u V_P + S_p\phi_P V_P. \end{aligned} \tag{5.13}$$

By inserting the spatially discretized terms into Eq. (5.3), the semi-discrete equation can be written as

$$\begin{aligned}\int_t^{t+\Delta t} \left[\left(\frac{\partial\rho\phi}{\partial t}\right)_P V_P + \sum_f F\phi_f - \sum_f (\rho D)_f S_i \left(\frac{\partial\phi}{\partial x_i}\right)_f\right] dt \\ = \int_t^{t+\Delta t} [S_u V_P + S_P V_P \phi_P]\, dt. \end{aligned} \tag{5.14}$$

The time integration is performed using a second-order time discretization method. The first approach is the Crank-Nicholson scheme in which the time derivative is approximated as

$$\left(\frac{\partial\rho\phi}{\partial t}\right)_P \cong \frac{\rho_P^{n+1}\phi_P^{n+1} - \rho_P^n\phi_P^n}{\Delta t}, \tag{5.15}$$

and

$$\int_t^{t+\Delta t} \phi(t)dt \cong \frac{1}{2}\left(\phi^n + \phi^{n+1}\right), \tag{5.16}$$

where

$$\phi^{n+1} = \phi(t_n + \Delta t) \text{ and } \phi^n = \phi(t_n). \tag{5.17}$$

Then Eqs. (5.2), (5.3) and (5.14) can be combined to get

$$\begin{aligned}\frac{\rho_P^{n+1}\phi_P^{n+1}-\rho_P^n\phi_P^n}{\Delta t}V_P &+ \frac{1}{2}\left(\sum_f F^{n+1}\phi_f^{n+1} - \sum_f (\rho D)_f^{n+1} S_i \left(\frac{\partial\phi}{\partial x_i}\right)_f^{n+1}\right) \\ &+ \frac{1}{2}\left(\sum_f F^{n}\phi_f^{n} - \sum_f (\rho D)_f^{n} S_i \left(\frac{\partial\phi}{\partial x_i}\right)_f^{n}\right) \\ &= S_u V_P + \frac{1}{2} S_p V_P \left(\phi_P^{n+1} + \phi_P^n\right). \end{aligned} \tag{5.18}$$

This equation requires value of ϕ at cell centers as well as at cell faces. Since all the quantities are stored at cell centers, we need to evaluate values at cell faces using values at cell centers. Values at faces are interpolated from the two cells sharing the face by using the linear basis function (Eq. (5.5)). Therefore for a control volume, Eq. (5.18) can be rearranged to have a system of algebraic equations in the form

$$a_P\phi_P^{n+1} + \sum_N a_N\phi_N^{n+1} = R_P, \tag{5.19}$$

where the summation is done over all N neighboring cells. Equation (5.19) can be written compactly as

$$[A][\phi] = [R], \tag{5.20}$$

where $[A]$ is a sparse matrix with a_P being on the diagonal and a_N being off the diagonal, $[\phi]$ is the solution vector, and $[R]$ is the residual vector.

A second way of the time discretization of the transport equation is a three time level method known as the backward differencing scheme which is a fully implicit scheme with a second order of accuracy [69]. Using the backward differencing scheme,

the transport equation can be written as

$$\frac{\frac{3}{2}\rho_P^{n+1}\phi_P^{n+1} - 2\rho_P^n\phi_P^n + \frac{1}{2}\rho_P^o\phi_P^o}{\Delta t}V_P + \sum_f F^{n+1}\phi_f^{n+1} - \sum_f (\rho D)_f^{n+1} S_i \left(\frac{\partial\phi}{\partial x_i}\right)_f^{n+1} = S_u V_P + S_p V_P \phi_P^{n+1}. \tag{5.21}$$

where

$$\phi^o = \phi(t_n - \Delta t). \tag{5.22}$$

It has been found that the backward differencing scheme is more robust than the Crack-Nicholson scheme [38]. Therefore, the backward differencing scheme is used in this study for the time discretization of the transport equations.

5.1.2 Finite Volume Discretization of Filtered Flow Equations

The discretization of the filtered momentum equations using the finite volume method described in the previous section results in an algebraic equation in the form

$$a_P \tilde{u}_{i,P}^{n+1} + \sum_N a_N \tilde{u}_{i,N}^{n+1} = Q_{\tilde{u}_i}^{n+1} - \left(\frac{\delta \bar{p}^{n+1}}{\delta x_i}\right)_P, \tag{5.23}$$

where P denotes the quantities evaluated at cell center of the control volume while N denotes the quantities evaluated at the cell center of the neighboring control volumes. Equation (5.23) is a non-linear equation since the coefficients of a_P and a_N depend on $\tilde{u}_i^{n+1}$. The linearization of Eq. (5.23) is performed by evaluating the coefficients of a_P and a_N by using the velocity fields that are known from previous time steps. The filtered continuity equation can be written in discrete form as

$$\left(\frac{\partial\bar{\rho}}{\partial t}\right)_P^{n+1} + \left[\frac{\delta\left(\bar{\rho}\tilde{u}_i^{n+1}\right)}{\delta x_i}\right]_P = 0. \tag{5.24}$$

where the second term on the left hand side is evaluated using the finite volume method.

5.1.3 The Pressure-Velocity Coupling

In a low Mach number turbulent reacting flows, density is solely determined from the compositions and independent of the pressure field. In this case, the mass conservation equation decouples from the momentum equation and the pressure field acts to modify the velocity field such that the mass conservation is satisfied. In this work, the pressure-velocity coupling is achieved by the PISO method [70]. In the PISO method, the velocity field is first predicted by using the known pressure field. For this purpose, the discretized momentum equation is written as [69]

$$a_P \tilde{u}_{i,P}^{n+1,*} + \sum_N a_N \tilde{u}_{i,N}^{n+1,*} = Q_{\tilde{u}_i}^n - \left(\frac{\delta \bar{p}^n}{\delta x_i}\right)_P. \tag{5.25}$$

Then the predicted velocity field $\tilde{u}_{i,P}^{n+1,*}$ can be calculated as

$$\tilde{u}_{i,P}^{n+1,*} = H(\tilde{u}_i^*) - \frac{1}{a_P}\left(\frac{\delta \bar{p}^n}{\delta x_i}\right)_P, \tag{5.26}$$

where

$$H(\tilde{u}_i^*) = \frac{Q_{\tilde{u}_i}^n - \sum_N a_N \tilde{u}_{i,N}^{n+1,*}}{a_P}. \tag{5.27}$$

Equation (5.25) is a non-symmetric linear systems solved iteratively using the pre-conditioned bi-conjugate gradients method [71]. The predicted velocity field $\tilde{u}_{i,P}^{n+1,*}$ does not generally satisfy the continuity equation since the pressure field used is taken from the previous time step. The velocity field is corrected by

$$\tilde{u}_{i,P}^{n+1} = H(\tilde{u}_i^*) - \frac{1}{a_P}\left(\frac{\delta \bar{p}^{n+1}}{\delta x_i}\right)_P. \tag{5.28}$$

Multiplying both sides of Eq. (5.28) by the filtered density field $\bar{\rho}$, taking discrete divergence and using Eq. (5.24), we get a Poisson equation for $\bar{p}^{n+1}$ in the form

$$\frac{\delta}{\delta x_i}\left[\frac{\bar{\rho}}{a_P}\left(\frac{\delta \bar{p}^{n+1}}{\delta x_i}\right)\right]_P = \left[\frac{\delta\left(\bar{\rho}H(\tilde{u}_i^*)\right)}{\delta x_i}\right]_P + \left(\frac{\partial \bar{\rho}}{\partial t}\right)_P^{n+1} \tag{5.29}$$

which is solved iteratively using the preconditioned conjugate gradients method [71]. Note that $\left(\frac{\partial \bar{\rho}}{\partial t}\right)_P^{n+1}$ is discretized using backward scheme. Using the solution of the Poisson equation, the velocity field can be corrected through Eq. (5.28). This is called as the first correction of the PISO method. The second correction can be performed by calculating $H(\tilde{u}_i^*)$ using the corrected velocity through Eq. (5.27). Then the second pressure equation using the new $H(\tilde{u}_i^*)$ is solved for the second correction velocity. The details of the PISO algorithm can be found in the original paper by Issa [70] and in the standard textbooks such as Peric and Ferziger [69]. The PISO algorithm used in the present study can be summarized as follows:

1. Calculate the coefficients of a_P and a_N, and the source term of Q in Eq. (5.25) using the values from the preceding iteration. If this is the first outer iteration, use the values from the previous time step.

2. Calculate the predicted velocity field from Eq. (5.26).

3. Solve the pressure equation (Eq.(5.29)).

4. Apply the first correction to the velocity field (Eq. (5.28)).

5. Calculate $H(\tilde{u}_i^*)$ using the corrected velocities, then solve the second pressure equation to update the pressure field, and apply the second correction. This gives the corrected velocity field, $\tilde{u}_i^m$.

6. Solve for the transport equation for the resolved specific volume (Eq. (4.68)).

7. If the residuals in the momentum and the scalar equations become smaller than

the given error tolerans, terminate the iteration and assign them as the values at the new time step. Otherwise, repeat the iteration starting from the step 1.

5.2 PDF Solver

In the PDF method, the flow is represented by a large number of Lagrangian particles. Each particle carries the properties of the physical position, $\boldsymbol{X}(t)$, and the scalar values, $\boldsymbol{\phi}(t)$. The particle properties are evolved by Eqs. (4.64) and (4.65) which can be written in the general from as

$$dX_j^*(t) = D_j(X_j^*(t), t)dt + b(X_j^*(t), t)dW_j(t), \tag{5.30}$$

$$d\phi_\alpha^*(t) = A(X_j^*(t), \phi_\alpha^*(t), t)dt. \tag{5.31}$$

Equation (5.30) is an Ito stochastic differential equation (SDE) and the coefficients of D_j and b are the drift and scalar diffusion coefficients, respectively. Equation (5.31) is a random differential equation because of the randomness of the coefficient $A(X_j^*(t), \phi_\alpha^*(t), t)$. Equation (5.31) can be solved by a standard ordinary differential equation (ODE) solver. This section presents the numerical methods used to solve the coupled particle equations, i.e., Eqs. (4.64) and (4.65) in the general context of the hybrid LES/PDF method.

5.2.1 Time Stepping Method for the Particle Equations

The coupled particle equations, Eqs. (4.64) and (4.65), are solved using a fractional time stepping method in which a fractional time step is taken for each physical processes: Transport in physical space $\mathbb{T}$, mixing and molecular diffusion $\mathbb{M}$, and reaction $\mathbb{R}$. The three physical processes of $\mathbb{T}$, $\mathbb{M}$ and $\mathbb{R}$ are represented by following equations:

$$\mathbb{T} : dX_j^* = \left[\tilde{u}_j + \frac{1}{\bar{\rho}}\frac{\partial(\bar{\rho}\widetilde{D}_T)}{\partial x_j}\right]^* dt + \left[2\widetilde{D}_T^*\right]^{1/2} dW_j^*, \tag{5.32}$$

$$\mathbb{M} : d\phi_\alpha^* = -\Omega^*(\phi_\alpha^* - \tilde{\phi}_\alpha^*)dt + \left[\frac{1}{\bar{\rho}}\frac{\partial}{\partial x_j}\left(\bar{\rho}\widetilde{D}\frac{\partial\tilde{\phi}_\alpha}{\partial x_j}\right)\right]^* dt, \tag{5.33}$$

$$\mathbb{R} : d\phi_\alpha^* = S_\alpha(\boldsymbol{\phi}^*)dt. \tag{5.34}$$

The first order accurate fractional time stepping methods are commonly used to advance the particle properties from time level n to $n+1$ [30, 18, 72, 35, 3]. In a typical first order method, each fractional step is taken sequentially for the transport $\mathbb{T}$, mixing $\mathbb{M}$ and reaction $\mathbb{R}$ for a full time step Δt. This is called the $\mathbb{TMR}$ method.

In this study, we use the first order fractional time stepping scheme ($\mathbb{TMR}$) to integrate the particle equations (Eqs. (4.64) and (4.65)). We describe the method in detail below where the superscripts $(.)^n$ and $(.)^{n+1}$ denote the properties at time t_n and $t_n + \Delta t$, respectively.

1. At the beginning of the particle time step, the particles are moved in the physical space for a full time step Δt according to Eq. (5.32). The time integration is performed using the first-order Euler scheme [73] as

$$X_j^{*,n+1} = X_j^{*,n} + \left[\tilde{u}_j^n + \frac{1}{\bar{\rho}^n}\frac{\partial\bar{\rho}^n D_T^n}{\partial x_j}\right]^* \Delta t + \left(2D_T^n\Delta t\right)^{1/2}\eta_j^*, \tag{5.35}$$

   where $\boldsymbol{\eta}^*$ is a standardized Gaussian random variable. To control the numerical error introduced by this simple first-order scheme, and maintain numerical stability, time step for each particle is determined according to the particle Courant number defined as $C^* \equiv |\boldsymbol{u}^*|\,\Delta t^*/\mathcal{L}^e$ where $|\boldsymbol{u}^*|$ is the LES velocity at the particle location and $\mathcal{L}^e$ is a characteristic length of the e^{th} computational cell. The time step size is split into substeps when Δt^* is smaller than the time step used in the LES solver. In this study, we set the particle Courant number to a fixed value of $C^* = 0.1$.

2. For the calculation of mixing and molecular transport, we mainly follow the method developed by Viswanathan et al. [74]. At the new of particle positions $\boldsymbol{X^{*,n+1}}$, the particle compositions are updated due to the mixing and molec-

ular diffusion according to Eq. (5.33). In the mixing and molecular transport fractional step, the particle compositions evolve by

$$\mathbb{M} : d\phi_\alpha^* = -\Omega^*(\phi_\alpha^* - \tilde{\phi}_\alpha^*)dt + \left[\frac{1}{\bar{\rho}}\frac{\partial}{\partial x_j}\left(\bar{\rho}\widetilde{D}\frac{\partial\tilde{\phi}_\alpha}{\partial x_j}\right)\right]^* dt. \tag{5.36}$$

Time integration of Eq. (5.36) is achieved using a semi-analytical first-order scheme, i.e.,

$$\phi_\alpha^{*,k} = \phi_\alpha^{*,n} + c^{*,n}\left(\tilde{\phi}_\alpha^{*,n} - \phi_\alpha^{*,n}\right) + \Delta\tilde{\phi}_\alpha^{*,n} \tag{5.37}$$

where superscript $(.)^k$ denotes the intermediate step between the mixing and reaction and $c^{*,n} = 1 - exp\,(-\Omega^{*,n}\Delta t)$. The term $\tilde{\phi}_\alpha^{*,n}$ is the mean composition evaluated at the new position $\boldsymbol{X^{*,n+1}}$, and $\Delta\tilde{\phi}_\alpha$ is the mean drift term calculated on the LES grid as

$$\Delta\tilde{\phi}_\alpha^n = \left[\frac{1}{\bar{\rho}^n}\frac{\partial}{\partial x_j}\left(\bar{\rho}^n\widetilde{D}^n\frac{\partial\tilde{\phi}_\alpha^n}{\partial x_j}\right)\right]\Delta t, \tag{5.38}$$

where the terms in the angle brackets on the right hand side are first evaluated at the LES cell centers using the finite volume approach, are then interpolated at the cell vertices and finally onto the particle locations (that will be discussed in the next sections).

3. Using the particle composition $\phi_\alpha^{*,k}$ as the initial condition, the reaction fractional step is performed using the ISAT [1] package

$$\frac{d\boldsymbol{\phi}}{dt} = \boldsymbol{S}(\boldsymbol{\phi}). \tag{5.39}$$

The scheme described above is nominally first-order in time. However, several second order accurate fractional time stepping schemes have been also developed by Wang et al. [75]. A second-order fractional time stepping method usually involves a

combination of half-time fractional steps. For example, the $\mathbb{TMRMT}$ [75] scheme can be summarized as follows:

1. $\mathbb{T}$: Using a weakly second order time stepping scheme such as the scheme developed by Cao and Pope [73], the particle positions are advanced in the physical space by a half-time step according to Eq. (5.32).

2. $\mathbb{M}$: Evolve the particle compositions by a half-time step due to the mixing and molecular diffusion according to Eq. (5.33).

3. $\mathbb{R}$: Advance the particle compositions by a full-time step due to the chemical reactions according to Eq. (5.34).

4. $\mathbb{M}$: Repeat the step 2.

5. $\mathbb{T}$: Repeat the step 1.

The details of the second order $\mathbb{TMRMT}$ method can be found in [75]. Note that the LES fields used in the PDF solver are located at time of $t^{n+1/2} = t_n + 0.5\Delta t$. Additionally, to maintain the second-order accuracy in the $\mathbb{TMRMT}$, the transport equation as in the form of Eq. (5.32) should be integrated by using a second-order accurate time integration method. In the literature, various second-order accurate schemes have been proposed [73, 76, 77, 78] for the integration of the Ito SDE in the same form as Eq. (5.32).

Wang and Pope [3] have compared the performance of the first-order and the second-order time stepping methods using a turbulent jet diffusion flame as the test case. They have observed that the first order methods can perform as well as the second order accurate methods for the turbulent jet diffusion flame.

5.2.2 Parallel Particle Tracking Algorithm

In the PDF solver, the Lagrangian particles move in the physical space according to Eq. (5.32). For this purpose, the filtered velocity field as well as the turbulent

frequency and diffusivity must be interpolated onto the particle location from the vertices of the host cell in which the particle resides. Therefore, the cell containing a given particle should be known. The simplest but computationally expensive way is to search for all the computational cells in the domain. However, considering the large number of particles, this method is not feasible due to high computational cost required. Tracking the particles as they move from one cell to an other constitutes a computationally feasible alternative and remedies this deficiency. Although, the tracking the particles on structured grids can be performed easily, the tracking on unstructured grids is not a simple task and requires a special treatment. In this study, we use OpenFOAM's particle tracking libraries to track the Lagrangian particles in the PDF solver. The libraries use the algorithm proposed by MacPherson et al. [79]. Fos simplicity, the algorithm is explained here only for the 2D case but it can be extended to the 3D case straightforwardly. Consider a particle located at the position $\boldsymbol{A}$ in a given cell (host cell) and moves to a new position $\boldsymbol{B}$ as shown in Fig. 5.4. If the point $\boldsymbol{B}$ is within the same cell as the point $\boldsymbol{A}$, then $\boldsymbol{B}$ is assigned as the new position of particle at the new time step and this assignment completes the tracking for the current time step. However, if the particle intersects a face of the cell at a point $\boldsymbol{P}$ then it stops at $\boldsymbol{P}$ and changes its pointer for the cell to the neighboring cell, and then continues its motion within the neighboring cell until reaching the final destination of point $\boldsymbol{B}$. The intersection point $\boldsymbol{P}$ can be computed as

$$\boldsymbol{P} = \boldsymbol{A} + \lambda_f \left(\boldsymbol{B} - \boldsymbol{A}\right) \tag{5.40}$$

where λ_f is the fraction of the line segment $\boldsymbol{AP}$ to the segment $|\boldsymbol{AB}|$, and can be calculated as

$$\lambda_f = \frac{(\boldsymbol{C_f} - \boldsymbol{A}) \cdot \boldsymbol{S_f}}{(\boldsymbol{B} - \boldsymbol{A}) \cdot \boldsymbol{S_f}}, \tag{5.41}$$

where $\boldsymbol{C_f}$ is the center of the face and $\boldsymbol{S_f}$ is the face unit normal vector.

In the particle tracking, the parallel algorithm used in the current LES/PDF

method must be also taken into account since the particles cross the subdomain boundaries frequently. In the OpenFOAM, the parallelization is achieved by the conventional domain decomposition method in which the computational domain is divided into subdomains. Each subdomain is assigned to an individual processor, which performs the calculations on its own subdomain. The data transfer required between the processors is performed through the faces shared by the individual processors, called the inter-processors-faces. In the PDF solver, when a particle that is initially assigned to processor k, moves and hits an inter-processors-face shared by processors k and l, then the particle is transferred from processor k to l using the MPI communication. The tracking algorithm can be summarized as follows:

1. Label initially all the particles as "active".

2. For a given particle, calculate λ values for all the faces of the host cell.

3. Find the minimum value λ_{min} in the interval $0 \leq \lambda \leq 1$, among all the λ_f values. The face associated with λ_{min} is to be crossed by the particle.

4. If λ_{min} is equal to zero, then the final destination, the point $\boldsymbol{B}$, is inside the host cell, then move the particle directly to the point $\boldsymbol{B}$ and complete the tracking.

5. If λ_{min} is greater than zero, first move the particle until the point $\boldsymbol{P}$ at the interface, and reduce the particle's tracking time t^k_{track} as

$$t^{k+1}_{track} = t^k_{track} - \lambda \Delta t, \tag{5.42}$$

   where t^k_{track} denotes the remaining time of a particle to complete a time step. Note that $t_{track} = \Delta t$ at the beginning of the movement.

6. If the face crossed by the particle is an internal face (shared by two cells both in the same subdomain), then change the cell pointer of the particle to the neighboring cell.

7. If the face crossed by the particle is inter-processor-face between the host processor k and a neighboring processor l, then add the particle index into a particle transfer list holding the indices of the particles to be transferred from the processor k to l, and label the particle as "passive".

8. For all the "active" particles, repeat the steps from 2 to 7 until t^k_{track} of all "active" particle becomes zero.

9. Transfer all the particles in the particle transfer lists between processors via a MPI communication.

10. For all the particles having t^k_{track} bigger than zero, repeat the steps from 1 to 9 until the particle transfer list becomes empty. This ensures that the tracking time for all the particles is reduced to zero.

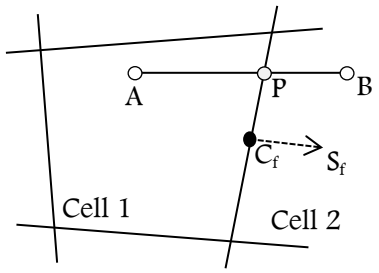

Figure 5.4: The schematic representation of the OpenFOAM particle tracking algorithm on an unstructured grid.

5.2.3 Mean Estimation From Particles

In the LES/PDF method, the mean particle fields obtained from the Lagrangian particles are required to evolve the particle composition due to mixing and molecular diffusion according to Eq. (5.33). Additionally, the some mean particles fields, i.e., mean temperature, specific volume, etc. are feedback from the PDF solver to the LES solver. Therefore estimation the mean properties from the Lagrangian particles

is one of the most important part of the LES/PDF methodology. The simplest way of estimating the means from the particles is to take an ensemble average over all the particles in a given cell. This is called the "particle-in-cell" (PIC) method. Although it is easy to implement, the mean fields obtained by the PIC exhibit discontinuities across the cell boundaries, which may results in reduction in numerical accuracy and even some numerical instability problems. A better method to estimate the mean properties can be formed by weighting the particles by linear basis functions. This is called the "cloud-in-cell" (CIC) method. The mean properties obtained by the CIC method are continuous across the computational cells. In this study, we follow the CIC method proposed by Zhang and Haworth [2] which is originated from the work by Dreeben and Pope [80]. In this approach, the mean values are evaluated at the cell vertecies. The mean at j^{th} vertex is obtained from the particles within the cells that share the j^{th} vertex (a set of cells, C_j). The mean at j^{th} vertex can be estimated as

$$\widetilde{\phi}_{(j)} = \frac{\sum_{k \in C_j} \sum_{i=1}^{N^{[k]}} \omega^{(i)} \phi^{(i)} b_\alpha(\zeta^{(i)})}{\sum_{k \in C_j} \sum_{i=1}^{N^{[k]}} \omega^{(i)} b_\alpha(\zeta^{(i)})}, \tag{5.43}$$

where $\omega^{(i)}$ is the weight of the individual particle (e.g., its mass), subscript α ($\alpha = 1, ..., 8$) is the local index corresponding to the j^{th} vertex, and b_α is the linear basis function of a given particle corresponding to the j^{th} vertex. Here the linear basis function b_α is based on the logical coordinates ζ_i of the particles within the computational cells. The logical coordinate system ζ_i is formed by transforming the physical coordinate system x_i in each cell. We use the isoparametric transformation of Zhang and Haworth [2] to define the local coordinates (also called the logical coordinates). Within a computational cell, the physical coordinates x_i are transformed into the logical coordinates ζ_i as shown in Fig. 5.5. As explained in [2], the logical coordinates of any point in a computational cell can be approximated using the heights of the

point from the faces of the cell as

$$\zeta_1 = \frac{h_1}{h_1 + h_2}, \zeta_2 = \frac{h_3}{h_3 + h_4}, \zeta_3 = \frac{h_5}{h_5 + h_6}, \tag{5.44}$$

where h_i is the height of the point from the i^{th} face of the cell as shown in Fig. 5.5. Then the linear basis functions for each vertex can be written as

$$\begin{aligned}
b_1 &= (1-\zeta_1)(1-\zeta_2)(1-\zeta_3), & b_2 &= \zeta_1(1-\zeta_2)(1-\zeta_3), \\
b_3 &= \zeta_1\zeta_2(1-\zeta_3), & b_4 &= (1-\zeta_1)\zeta_2(1-\zeta_3), \\
b_5 &= (1-\zeta_1)(1-\zeta_2)\zeta_3, & b_6 &= \zeta_1(1-\zeta_2)\zeta_3, \\
b_7 &= \zeta_1\zeta_2\zeta_3, & b_8 &= (1-\zeta_1)\zeta_2\zeta_3.
\end{aligned} \tag{5.45}$$

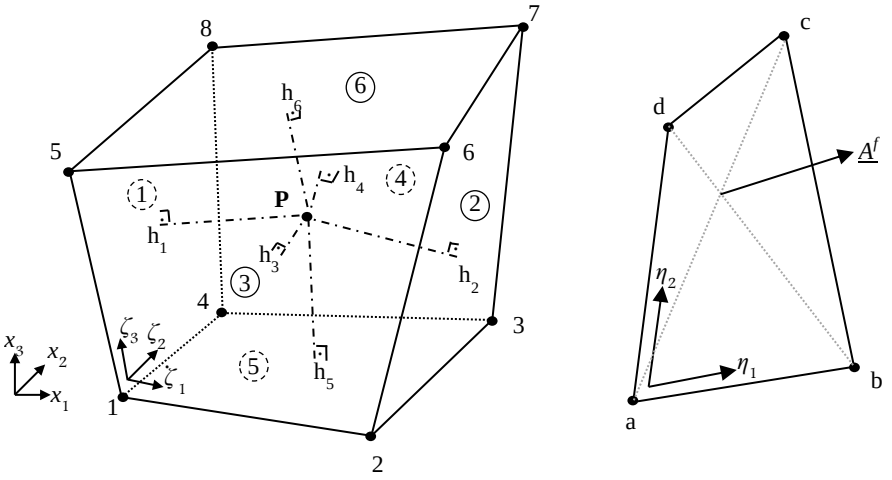

Figure 5.5: Isoparametric representation. The logical coordinates (ζ_1, ζ_2, ζ_3) (left). The logical coordinates (η_1, η_2) on a face of the cell (right).

5.2.4 Interpolation of the Mean Values Onto Particles

The mean estimation method described in the previous section calculates the mean properties at the cell vertices. Some mean properties such as mean composition are used in the particle equations, thus they need to be evaluated at the particle locations.

On the other hand, some of the mean properties from the particles, i.e., the mean specific volume and the mean temperature are needed in the LES solver, thus they are required to be evaluated at the cell centers. In addition, various mean fields are needed for the post processing purpose. Therefore, the mean properties at the cell vertices are interpolated onto the Lagrangian particle locations and also the cell center locations by using the linear basis functions presented in the previous section as

$$\widetilde{\phi}^{(i)} = \sum_{\alpha} \widetilde{\phi}_{(j)} b_{\alpha}(\zeta^{(i)}), \tag{5.46}$$

where $\widetilde{\phi}_{(j)}$ is the mean field at the j^{th} global vertex. ζ^i is the logical coordinate of i^{th} particle (or cell center of i^{th} cell) and j is the global index of the vertex and α is the local index in a cell of the j^{th} global index.

5.2.5 Interpolation of the Finite Volume Fields on Particle Positions

In the particle equations, $\tilde{u}_i$, Ω, $\bar{\rho}$, $\tilde{D}$, $\tilde{D}_T$ are required at the Lagrangian particle positions. Thus the LES fields need to be evaluated at the particle locations at each time step. The LES solver stores the LES fields at the cell centers. To evaluate the fields at the Lagrangian particle locations, they need to be interpolated from the cell centers onto the particle locations. For this purpose, the LES fields are first interpolated onto the cell vertices. After evaluating the LES fields at the cell vertices, they are interpolated onto the particle locations from the cell vertices in the same way as one for the interpolation of the particle mean properties in the previous section. The LES fields are first evaluated at the cell vertices from the cell centers as

$$\phi_{(j)} = \sum_{k \in C_j} b_{\alpha}(\zeta^k) \tilde{\phi^k} / \sum_{k \in C_j} b_{\alpha}(\zeta^k), \tag{5.47}$$

where C_j is a set of cells sharing the j^{th} vertex, $b_{\alpha}(\zeta^k)$ are the linear basis functions associated with the j^{th} vertex (α is the local index within the cell corresponding to the global index j), and $\tilde{\phi^k}$ is the LES fields located at the cell center of the k^{th} cell.

After evaluating the LES fields at the cell vertices, they are interpolated onto particle locations in the same way as explained in the previous section, i.e., Eq. (5.46).

5.2.6 Particle Number Control

The PDF solver is initialized with a nominal number of particles, N_p, in each FV cell. During a simulation, it is desired to keep the number of particles in each FV cell within a specified range. Here, we use a range of $\frac{\sqrt{2}N_p}{2} \leq N_p \leq \sqrt{2}N_p$. The particle control algorithm is designed to keep the number of particles within this range throughout the simulation. When the number of particle in a cell drops below the lower limit, the heaviest particle (based on the volume or mass) is determined in the cell and it is split into two by keeping the other properties the same but halving its volume and mass. This splitting process is repeated until the number of particles exceeds the lower limit. The split particles initially occupy the same location but drift from each other quickly due to the stochastic nature of Eq. (5.32). In the case of an excessive number of particles in a cell, we cluster the lightest particle in the cell (say, particle a) with the closest particle to it (in physical space) (say, particle b). The mean properties and the total mass and volume obtained from particles a and b are assigned to the particle b, and the particle a is deleted. This clustering process is repeated until the number of particles reduces below the upper limit.

5.2.7 Three-Stage Velocity Correction Method

The consistency condition in the hybrid LES/PDF method requires that the mean particle mass distribution in the PDF method should be consistent with the fluid mass distribution in the LES solver, and this consistency should be satisfied throughout the simulation. In the LES/PDF method, the equations solved by finite volume-LES method and the equations, solved by the Lagrangian Monte Carlo PDF algorithm are mathematically consistent. However, inconsistency may arise due to accumulation of numerical error. To satisfy this condition, various correction methods have been proposed in the literature [81, 28, 82, 83]. In this study, a three-stage velocity

correction method developed by Zhang and Haworth [2] is employed to enforce the consistency condition. The method can be applied to unstructured finite volume grids for complex geometries. The method consists of three stages:

- Stage 1: The cell centered velocity fields are first interpolated onto the cell vertices using Eq. (5.47), i.e.,

$$u_i^l = \sum_{k \in C_l} b_\alpha(\zeta^k) u_i^k / \sum_{k \in C_l} b_\alpha(\zeta^k), \tag{5.48}$$

  where C_l is the set of the cells that share the vertex l, $b_\alpha(\zeta^k)$ is the basis function associated with the k^{th} cell that contributes to the vertex l. Here index α is the local index within the cell corresponding to the global index l. Then the velocities are interpolated from the cell vertices onto the particle locations using Eq. (5.46) as

$$u_i^p = \sum_{\alpha} u_i^l b_\alpha(\zeta^p), \tag{5.49}$$

  where ζ^p is the logical coordinate of the particle location, $b_\alpha(\zeta^p)$ is the basis function associated with the vertex l, and u_i^l is the velocity at the l^{th} vertex.

- Stage 2: The mass flux from the k^{th} cell across the face f implied by the trilinear interpolation scheme for the velocity and density fields (e.g., Eq. (5.49)) is denoted by $Q^{k,f,TL}$ and can be written as

$$Q^{k,f,TL} = A^f \sum_{k \in f} b_\alpha(\zeta^p) \rho^k (u_1^k n_1^{k,f} + u_2^k n_2^{k,f} + u_3^k n_3^{k,f}), \tag{5.50}$$

  where A^f is the face area, $\boldsymbol{n}^{k,f} = (n_1^{k,f}, n_2^{k,f}, n_3^{k,f})$ is the outward-pointing unit normal vector of the face f, and ζ^p is the logical coordinate of the face center, $b_\alpha(\zeta^p)$ is the basis function associated with the vertex k where α is the local index within the cell corresponding to the global index k.

In general, the mass flux $Q^{k,f,TL}$ is not equal to the mass flux in the finite volume (LES) solver $Q^{k,f,FV}$. The main purpose in this stage is to introduce correction velocities at cell vertices in order to make $Q^{k,f,FV}$ and $Q^{k,f,TL}$ consistent. The correction fluxes can be written as

$$\begin{aligned}\hat{Q}^{k,f} &= Q^{k,f,FV} - Q^{k,f,TL} \\ &= A^f \sum_{k \in f} b_\alpha(\zeta^p)\rho^k(\hat{u}_1^{k,\nu} n_1^{k,f} + \hat{u}_2^{k,\nu} n_2^{k,f} + \hat{u}_3^{k,\nu} n_3^{k,f}),\end{aligned} \tag{5.51}$$

where the hat $\hat{.}$ is used to denote the correction mass fluxes and the correction velocities at the cell vertices. For each computational cell, there are 24 velocity components $\hat{u}_i^{k,f}$ to be determined (three velocity components for each of eight vertices ν). Although, there are 24 velocity components to be determined, only six equations exist, thus the linear system is underdetermined. To circumvent this problem, the normal components of the correction mass fluxes are assumed to be uniform across each of the six faces of the k^{th} cell. This requires that the normal components of the multiplication of the density and correction velocity at each vertices of a face f are equal. Therefore, we have additional three equations for each face as

$$\begin{aligned}\rho^{l_1}(\hat{u}_1^{k,\nu_1} n_1^{k,f} + \hat{u}_2^{k,\nu_1} n_2^{k,f} + \hat{u}_3^{k,\nu_1} n_3^{k,f}) &= \rho^{l_2}(\hat{u}_1^{k,\nu_2} n_1^{k,f} + \hat{u}_2^{k,\nu_2} n_2^{k,f} + \hat{u}_3^{k,\nu_2} n_3^{k,f}) \\ \rho^{l_1}(\hat{u}_1^{k,\nu_1} n_1^{k,f} + \hat{u}_2^{k,\nu_1} n_2^{k,f} + \hat{u}_3^{k,\nu_1} n_3^{k,f}) &= \rho^{l_3}(\hat{u}_1^{k,\nu_3} n_1^{k,f} + \hat{u}_2^{k,\nu_3} n_2^{k,f} + \hat{u}_3^{k,\nu_3} n_3^{k,f}), \\ \rho^{l_1}(\hat{u}_1^{k,\nu_1} n_1^{k,f} + \hat{u}_2^{k,\nu_1} n_2^{k,f} + \hat{u}_3^{k,\nu_1} n_3^{k,f}) &= \rho^{l_4}(\hat{u}_1^{k,\nu_4} n_1^{k,f} + \hat{u}_2^{k,\nu_4} n_2^{k,f} + \hat{u}_3^{k,\nu_4} n_3^{k,f}),\end{aligned} \tag{5.52}$$

where ν_1, ν_2, ν_3 and ν_4 denote the local indices for four the vertices of face f (correponding to the global vertices l_1, l_2, l_3 and l_4, respectively). Three equations for each face, thus eighteen additional equations in total can be used to form a complete set of the mass correction equations. For each computational cell, 24 velocity components of the correction velocity can be determined by solving a linear equation system. Note that the correction velocities at a vertex

shared by two neighboring cells may not be the same for the each cell.

- Stage 3: In this stage, the velocity correction is formulated in the same way as Stage 2, i.e.,

$$\hat{\hat{Q}}^{k,f} = A^f \sum_{k \in f} b_\alpha(\zeta^p)\rho^k(\hat{\hat{u}}_1^{k,\nu} n_1^{k,f} + \hat{\hat{u}}_2^{k,\nu} n_2^{k,f} + \hat{\hat{u}}_3^{k,\nu} n_3^{k,f}), \tag{5.53}$$

where $\hat{\hat{Q}}^{k,f}$ is the correction mass flowrate at cell k across face f, and $\hat{\hat{u}}_i$ is the correction velocity at i^{th} vertex. The Stage 3 aims to eliminate the time-scaled deviation between the fluid mass in the LES solver $m^{k,FV}$ and the particle mass in the PDF solver $m^{k,p}$ associated with the cell k. Here, the time-scaled deviation referred as mass residual, R^k, is defined as

$$R^k \equiv \frac{m^{k,FV} - m^{k,p}}{\tau_{S3}}, \tag{5.54}$$

where τ_{S3} is a relaxation time scale defined as $\tau_{S3} = \alpha \Delta t$ where α is a specified coefficient. The main purpose of this stage is to calculate mass flowrates $\hat{\hat{Q}}^{k,f}$ that satify

$$R^k = -\sum_{f \in k} \hat{\hat{Q}}^{k,f}. \tag{5.55}$$

Equation (5.55) is in the same form as the discretized pressure Poisson equation and can be solved using the same solver. The solution of Eq. (5.55) gives the stage 3 velocity correction $\hat{\hat{u}}_i$. The particle positions are advanced according to the Stage 3 velocity correction to enforce the mass consistency between the LES and the PDF solvers.

A summary of the three-stage-velocity correction algorithm is given as follow:

1. Interpolate the LES velocities from the cell centers to the cell vertices, referred as $\boldsymbol{U}_c^{S1}$ from Eqs. (5.48) and (5.49).

2. Calculate the Stage 2 correction velocity, $\boldsymbol{U}_c^{S2}$, at the cell vertices from Eq. (5.51).

3. Using the combined velocity, $\boldsymbol{U}_c^{S1} + \boldsymbol{U}_c^{S2}$, move the particles in the physical space according to Eq. (5.35).

4. Calculate the particle mass residual, R^k, for each cell.

5. Then, solve the linear equation system Eq. (5.55) for the Stage 3 velocity, $\boldsymbol{U}_c^{S3}$.

6. Advance the particle positions due to the Stage 3 velocity $\boldsymbol{U}_c^{S3}$ to enforce the mass consistency.

More details of the velocity correction method can be found in [2].

Chapter 6

THE PILOTED METHANE/AIR JET DIFFUSION FLAME

The new hyrid LES/PDF solver described in the previous chapters is first applied to a piloted methane/air jet diffusion flame (Sandia Flame D) [84]. In this chapter, we first present the experimental configuration and the computational setup for the Sandia Flame D. Then the consistency between the LES and the PDF solvers is examined using the one-way coupling method with a simple flamelet model. The details of the consistency conditions and the one-way coupling method are presented in this section. Then extensive simulations are performed using a detailed chemical mechanism and the results are compared with the experimental measurements as well as the previous LES/PDF simulations. Then the performance of the velocity correction method is demonstrated. For this purpose, the effects of each stage of the three-stage method are examined separately and all together. Finally, the performance of the LES/PDF solver is discussed for the computational efficiency.

6.1 Experimental Configuration

The schematic of the burner is shown in Fig. 6.1. The burner consists of a central fuel jet surrounded by a pilot nozzle. An air-coflow surronds both the pilot and fuel jets. The dimensions of the burner are summarized in Table 6.1. The fuel jet is a mixture of 25% methane and 75% air by volume. The pilot flame is a lean (the equivalence ratio, $\phi = 0.77$) mixture of C_2H_2, H_2, air, CO_2, and N_2 with the same nominal enthalpy and equilibrium composition as methane/air at this equivalence ratio. The jet bulk velocity is $U_j = 49.6$ m/s corresponding to a Reynolds number of $Re = 22400$, temperature is 294 K and pressure is 0.993 atm. The pilot and coflow

bulk velocities are 11.4 m/s and 0.9 m/s, respectively. More details about this flame are available in Barlow et al. [84].

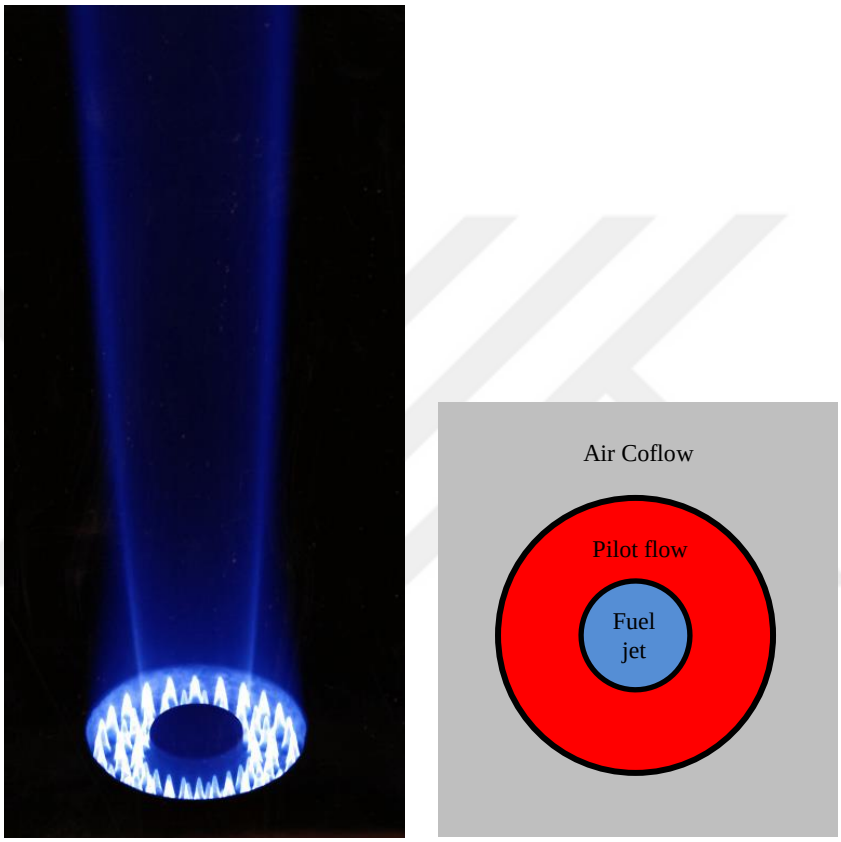

Figure 6.1: Schematic of the burner exits (right), and the pictures of the flame (left) [10]

6.2 Computational Setup

The computational domain is selected to be [0,60D]×[0,20D]×[0,2π] in the axial (x), radial (r) and azimuthal (θ) directions, respectively. The domain is discretized using a non-uniform 256×128×32 block structured cylindrical grid as shown in Fig. 6.2. The grid is concentrated near the nozzle in the axial and radial directions.

The instantaneous inlet velocities of the fuel jet are obtained from a separate LES turbulent pipe flow simulation. For this purpose, LES simulation is performed for a turbulent pipe flow with the same dimension as the fuel jet inlet. In the pipe flow

Table 6.1: Dimensions of the Sandia piloted jet flame burner

Main jet inner diameter, D	=	7.2 mm
Pilot annulus inner diameter	=	7.7 mm
Pilot annulus outer diameter	=	18.2 mm
Burner outer wall diameter	=	18.9 mm

simulation, flow is initialized to have the experimentally measured mean velocity profile at the fuel jet inlet with small random perturbations. The periodic boundary conditions are applied at the inlet and outlet, and no-slip boundary conditions are used at the wall of the pipe. The pipe flow simulation is first performed until the turbulent flow reaches a statistically stationary state, and then the flow velocities on a plane perpendicular to the pipe axial direction are stored in a file as time series with a specified time step size. Then the velocities stored in the file are retrieved and interpolated on the grid points in the fuel jet inlet during the LES/PDF simulations. The interpolation is performed using the cylindrical coordinates. Note that the interpolated velocities at the fuel jet inlet may not have the same mean and rms profiles as the experimental measurements at the fuel jet inlet. Therefore, instead of directly using the interpolated velocities following [85], we apply the turbulent inlet velocity at the fuel jet computed as

$$u_i^s(r,\theta,t) = \langle u_i(r)\rangle_m + \alpha_i(r)\left[u_i^l(r,\theta,t) - \left\langle u_i^l(r)\right\rangle\right] \tag{6.1}$$

where $\langle u_i(r)\rangle_m$ and $\left\langle u_i^l(r)\right\rangle$ are the mean values of the experimental and the interpolated velocities, respectively, and $u_i^l(r,\theta,t)$ is the interpolated instantaneous velocity while $u_i^s(r,\theta,t)$ is the scaled instantaneous velocity to be used at the fuel jet inlet. The scaling parameter $\alpha_i(r)$ is used to match the interpolated fluctuating velocities with the experimental fluctuating velocities, and it is computed as

$$\alpha_i(r) = \frac{\langle u_i'(r)\rangle_l}{\langle u_i'(r)\rangle_m}, \tag{6.2}$$

where $\langle u_i'(r)\rangle_m$ is the experimental measurement of the rms velocity and $\langle u_i'(r)\rangle_l$ is the rms of the interpolated velocity calculated as

$$\langle u_i'(r)\rangle_l = \sqrt{\langle u_i^l(r,\theta,t)^2\rangle - \langle u_i^l(r)\rangle^2}. \tag{6.3}$$

At the pilot nozzle exit, we use the experimental mean radial profile of the axial velocities as the inlet boundary conditions by neglecting the turbulent fluctuations The inlet velocity of the air-coflow is set to a value of 0.4 m/s. At the wall-lips between the fuel jet and pilot flame as well as between the pilot and the coflow, the slip boundary conditions are applied. At the outlet, the zero-gradient boundary conditions are used for all the fields. At the far fields, the slip boundary conditions are applied. In the PDF solver, about 20 particles per grid cell are used in all the results presented in this chapter.

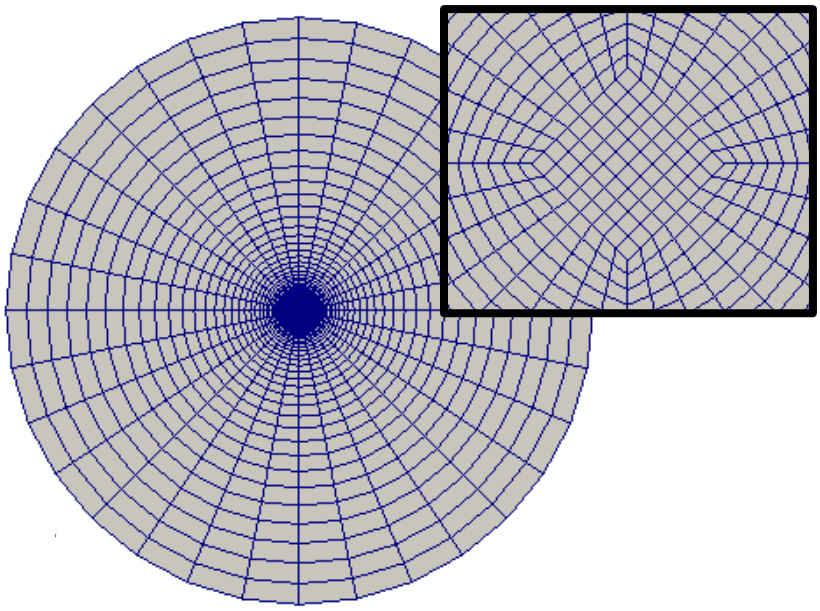

Figure 6.2: The block structured grid used in the simulations.

6.3 The Consistency Between LES and PDF Solvers

In this section, we first examine the numerical consistency between the LES and PDF solvers. For this purpose, we follow the one-way coupling methodology proposed by Wang and Pope [3]. In the one-way coupling methodology, the equations solved by the LES and the PDF solvers are mathematically consistent. Additionally the LES and the PDF solvers are coupled in a one-way fashion to isolate the numerical error regarding the fully coupled scheme. Since the equations solved by the LES and PDF solvers are equivalent at the level of the first and second moments and scalar fields are computed redundantly in the both solver, the one-way coupling method is very useful to examine the numerical consistency between the LES and the PDF solvers. In the remaining of this section, the details of the one-way coupling methodology are presented and then the numerical consistency between the LES and PDF solvers is demonstrated through comprehensive simulations.

6.3.1 The Moment Equations

In the one-way coupling, we first derive the transport equations for the first two moments of compositions directly from the modelled joint PDF evolution equation (Eq. (4.61)): The Favre-filtered transport equations of the first two moments of the compositions are given by [74]

$$\frac{\partial\left(\bar{\rho}\widetilde{\phi_\alpha}\right)}{\partial t}+\frac{\partial\left(\bar{\rho}\widetilde{u}_j\widetilde{\phi_\alpha}\right)}{\partial x_j}=\frac{\partial}{\partial x_j}\left(\bar{\rho}\left(\widetilde{D}+\widetilde{D}_T\right)\frac{\partial\widetilde{\phi_\alpha}}{\partial x_j}\right)+\bar{\rho}\tilde{S}, \tag{6.4}$$

$$\begin{aligned}\frac{\partial\left(\bar{\rho}\widetilde{\phi_\alpha^2}\right)}{\partial t}+\frac{\partial\left(\bar{\rho}\widetilde{u}_j\widetilde{\phi_\alpha^2}\right)}{\partial x_j}=&\frac{\partial}{\partial x_j}\left(\bar{\rho}\widetilde{D}_T\frac{\partial\widetilde{\phi_\alpha^2}}{\partial x_j}\right)+2\widetilde{\phi_\alpha}\frac{\partial}{\partial x_j}\left(\bar{\rho}\widetilde{D}\frac{\partial\widetilde{\phi_\alpha}}{\partial x_j}\right)\\&-2\bar{\rho}\Omega\left(\widetilde{\phi_\alpha^2}-\widetilde{\phi_\alpha}^2\right)+2\tilde{\rho}\widetilde{S_\alpha\phi_\alpha},\end{aligned} \tag{6.5}$$

where $\tilde{\phi}_\alpha$ and $\widetilde{\phi_\alpha^2}$ are the filtered mass fraction and mass fraction square of species α and $\tilde{S}$ and $\widetilde{S\phi}$ are the chemical source terms. The moment equations and the modeled transport equations for the joint-PDF are mathematically consistent at the level of

the first and second moments. This mathematical consistency is used here to verify the numerical consistency of the LES and the PDF solvers.

The solution of the moment equations by the LES solver is a challenging task due to the number of composition fields and the unclosed chemical source terms. To overcome this difficulty, we use a conservative scalar field (the mixture fraction field $\tilde{\xi}$) as the composition variable ($\tilde{\xi} = \tilde{\phi}$). Thus the moment equations simplify to be

$$\frac{\partial\left(\bar{\rho}\widetilde{\xi}\right)}{\partial t} + \frac{\partial\left(\bar{\rho}\widetilde{u}_j\widetilde{\xi}\right)}{\partial x_j} = \frac{\partial}{\partial x_j}\left(\bar{\rho}\left(\widetilde{D} + \widetilde{D}_T\right)\frac{\partial\widetilde{\xi}}{\partial x_j}\right), \tag{6.6}$$

$$\begin{aligned}\frac{\partial\left(\bar{\rho}\widetilde{\xi^2}\right)}{\partial t} + \frac{\partial\left(\bar{\rho}\widetilde{u}_j\widetilde{\xi^2}\right)}{\partial x_j} = &\frac{\partial}{\partial x_j}\left(\bar{\rho}\widetilde{D}_T\frac{\partial\widetilde{\xi^2}}{\partial x_j}\right) + 2\widetilde{\xi}\frac{\partial}{\partial x_j}\left(\bar{\rho}\widetilde{D}\frac{\partial\widetilde{\xi}}{\partial x_j}\right) \\ &- 2\bar{\rho}\Omega\left(\widetilde{\xi^2} - \tilde{\xi}^2\right).\end{aligned} \tag{6.7}$$

Here, we note that the chemical source terms disappeared since the mixture fraction is a conserved scalar. These two scalar equations can be solved by the LES method numerically using the numerical methods as discussed in Section 5.

Additionally, in the PDF solver, the particle equations are solved only for a single composition of mixture fraction (ξ). Then the resolved fields of mixture fraction and square of mixture fraction are obtained from the particles by

$$\tilde{\xi}_{PDF} = \frac{\langle m^*\xi^*\rangle}{\langle m^*\rangle}, \tag{6.8}$$

$$\tilde{\xi^2}_{PDF} = \frac{\left\langle m^*{\xi^*}^2\right\rangle}{\langle m^*\rangle}, \tag{6.9}$$

where m^* and ξ^* are the particle mass and mixture fraction, respectively.

6.3.2 The One-way Coupling Methodology

Although the equations solved by the LES and the PDF solvers are mathematically consistent, the numerical inconsistency may arise due to the accumulation of numerical errors and the different numerical solution methodologies used in the LES

and PDF solvers. Here, we investigate the consistency between the LES and the PDF fields at the numerical solution level. To avoid the numerical error due to the coupling method described in Section 4, we use the one-way coupling methodology developed by Wang and Pope [3].

In the one-way coupling methodology, as its name implies, the data transfer occurs only in the one direction, from the LES solver to the PDF solver. The fields calculated by the PDF solver are used only for the output purpose, i.e., there is no feedback from the PDF solver to the LES solver as schematically shown in Fig. 6.3. The LES algorithm solves the filtered equations for the mixture fraction and the square of the mixture fraction fully coupled with the filtered flow equations. In the PDF solver, the particle equations (Eqs. (4.64) and (4.65)) are solved only for a single composition of the mixture fraction (ξ) using the fields $\tilde{u}_i$, $\bar{\rho}$, Ω, D and D_T taken from the LES solver.

In the LES solver, the chemistry is represented by a single laminar flamelet profile obtained by FlameMaster [86] software using GRI 2.11 mechanism [40] by specifying a nominal strain rate of $a_n = 100\ s^{-1}$. The resolved species mass fraction, $\tilde{Y}$, temperature, $\tilde{T}$, and density, $\bar{\rho}$, are pretabulated with the resolved mixture fraction, $\tilde{\xi}$, and the square of mixture fraction, $\widetilde{\xi^2}$. Once $\tilde{\xi}$ and $\widetilde{\xi^2}$ are computed from Eqs. (6.6) and (6.7), then the resolved density $\bar{\rho}$ is obtained from the tabulation table as a function of $\tilde{\xi}$ and $\widetilde{\xi^2}$.

At each time step, the PDF solver receives the fields $\tilde{u}_i$, $\bar{\rho}$, Ω, $\tilde{D}$ and $\tilde{D}_T$ from the LES solver, then solves the particle equations (Eqs. (4.64) and (4.65)) with a single composition of mixture fraction (ξ).

6.3.3 Results

In the one-way coupled LES/PDF simulation, the fields of the resolved mixture fraction, $\tilde{\xi}$, square of mixture fraction, $\tilde{\xi^2}$, and temperature, $\tilde{T}$, are computed redundantly by the LES and PDF solvers. To compare the numerical results from the LES and PDF solvers with each other as well as with the experimental data, we take time

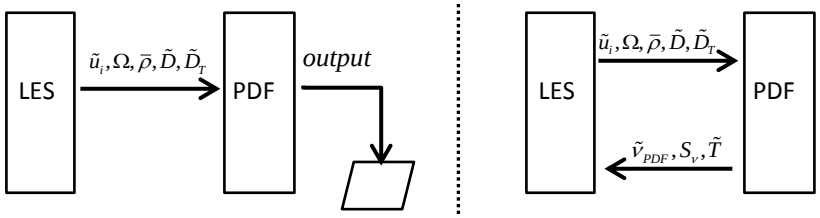

Figure 6.3: Schematic representation of one-way coupled (left) and two-way coupled (right) LES/PDF solver.

average of the resolved fields denoted by $\langle\cdot\rangle$. We first present radial profiles of the time-averaged resolved velocity $\langle\tilde{u}_i\rangle$ and resolved axial turbulence intensity $\langle u''\rangle$ to show that the flow fields are well captured in the simulations. Then the time-averaged LES and PDF results of the resolved mixture fraction, $\langle\tilde{\xi}\rangle$, and resolved temperature, $\langle\tilde{T}\rangle$, as well as the rms of mixture fraction $\langle\tilde{\xi''}\rangle = (\langle(\tilde{\xi})^2\rangle - \langle\tilde{\xi}\rangle^2)^{1/2}$ and the rms of temperature, $\langle\tilde{T''}\rangle$, are plotted to demonstrate the numerical consistency. Figure 6.4 shows the time-averaged profiles of the LES and PDF fields with the experiment measurements at four axial locations of x/D =7.5, 15, 30 and 45. As can be seen in this figure, the mean axial velocity and turbulence intensity are in good agreement with the experimental data, showing that the flow fields are well captured. The time-averaged resolved mixture fraction $\langle\tilde{\xi}\rangle$ and the rms of mixture fraction $\langle\tilde{\xi''}\rangle$ from the LES and PDF solvers are compared. The numerical results from the two solvers are in excellent agreement, demonstrating that the LES and PDF solvers are consistent at the level of numerical solution. Additionally this consistency indicates very good performance of the calculations in the PDF solver, i.e., the particle tracking, mean estimation and interpolation. The time-averaged resolved temperature $\langle\tilde{T}\rangle$ from the LES and the PDF solvers are almost identical while very slight discrepancies occur in the rms of the temperature $\langle\tilde{T''}\rangle$ fields obtained by the two solvers. Consequently, the excellent agreement between the numerical results from the LES and the PDF solvers show that the two solvers have high level of consistency at the numerical solution level. Although, a simple flamelet model is used in the simulations, the agreement with the experimental data is also very good.

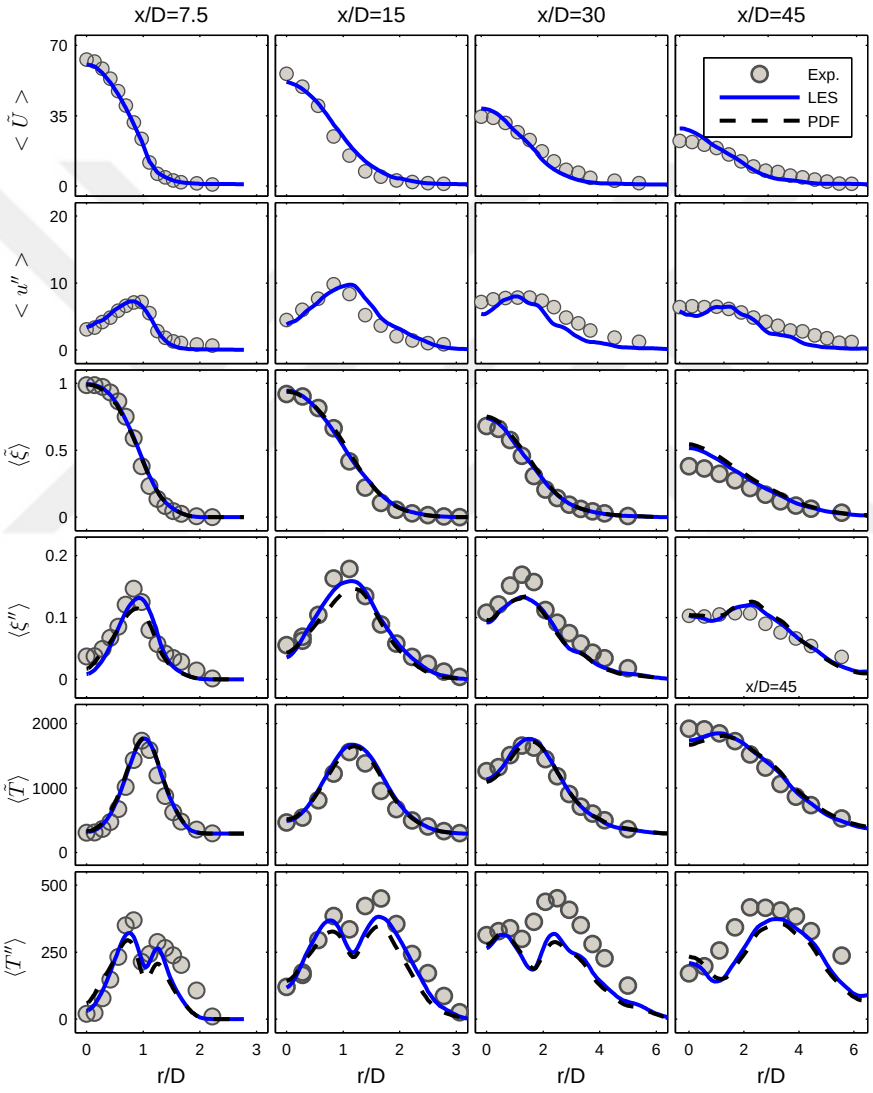

Figure 6.4: The one-way coupling. The radial profiles of time-averaged resolved axial velocity, the resolved turbulence intensity, resolved mixture fraction, the rms of mixture fraction, resolved temperature and the rms of temperature, from top to bottom at four axial location of x/D =7.5, 15, 30 and 45 from left to right. Symbols, the experimental data; blue line, the LES results; black dashed line, the PDF results.

6.4 Detailed Chemistry Calculations

The detailed chemistry simulations are performed using the augmented reduced mechanism (ARM1) that includes 16-species and 12-reactions [4]. The chemical species and the elementary reactions are given in Table 6.2. The rates of the elementary reactions are obtained dynamically from the GRI 2.11 mechanism [40]. In the PDF solver, each particle carries the mass fractions of chemical species and the enthalpy. Figure 6.5 shows the computational modules used in the detailed chemistry calculations. The LES algorithm solves the filtered mass and momentum equations, and then the PDF solver performs the step 1 and 2 in the $\mathbb{TMR}$ fractional time stepping method while the third step is performed by the ISAT module to evolve the particles in the composition space due to the chemical reactions. The simulations are performed for ten flow-through times based on jet bulk velocity to reach a statistically stationary state, then an additional ten flow-through times are performed to collect the statistics from the instantenous resolved fields. For instance, the instantenous resolved temperature field is shown in Fig. 6.6.

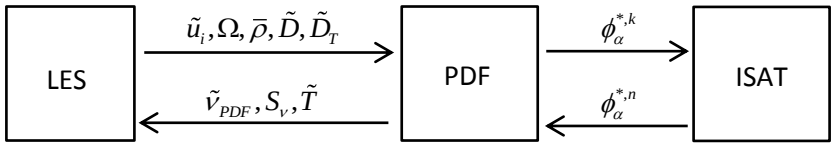

Figure 6.5: The computational modules used in the detailed chemistry calculations.

Figure 6.7 presents the time-averaged radial profiles of the resolved temperature, $\langle\tilde{T}\rangle$, and resolved species mass fractions, $\langle\tilde{Y}\rangle$, of CO_2, CO, O_2 and CH_4 at four axial locations of x/D =7.5, 15, 30 and 45. The numerical results are compared with the experimental data as well as with the results from a previous LES/PDF simulations [87] at the locations where they are available. At the locations of $x/D = 7.5$ and 15, the results are in very good agreement with the experimental data and at the location of $x/D = 15$ the results produced in the present study are closer to the experimental data than those from the previous LES/PDF simulations. At the location of $x/D =$

Table 6.2: The augmented reduced mechanism for the methane/air combustion including 16 species - 12 reactions (ARM1) [4].

ELEMENTS
H O C N
SPECIES
H_2 O_2 OH HO_2 H_2O_2 HO_2 H CO CO_2 C_2H_2 C_2H_4 C_2H_6 CH_2O CH_4 CH_3 N_2
END
REACTIONS
1 $O_2 + 2\ CO = 2\ CO_2$
2 $H + O_2 + CO = OH + CO_2$
3 $H_2 + O_2 + CO = H + OH + CO_2$
4 $HO_2 + CO = OH + CO_2$
5 $O_2 + H_2O_2 + CO = OH + HO_2 + CO_2$
6 $O_2 + 0.50\ C_2H_2 = H + CO_2$
7 $O_2 + CH_3 + CO + C_2H_4 = CH_4 + CO_2 + CH_2O + 0.50\ C_2H_2$
8 $O_2 + 2CH_3 = H_2 + CH_4 + CO_2$
9 $O_2 + 2CH_3 + CO = CH_4 + CO_2 + CH_2O$
10 $O_2 + CH_3 + CO = H + CO_2 + CH_2O$
11 $O_2 + CO + C2H_6 = CH_4 + CO_2 + CH_2O$
12 $H + OH = H_2O$
END

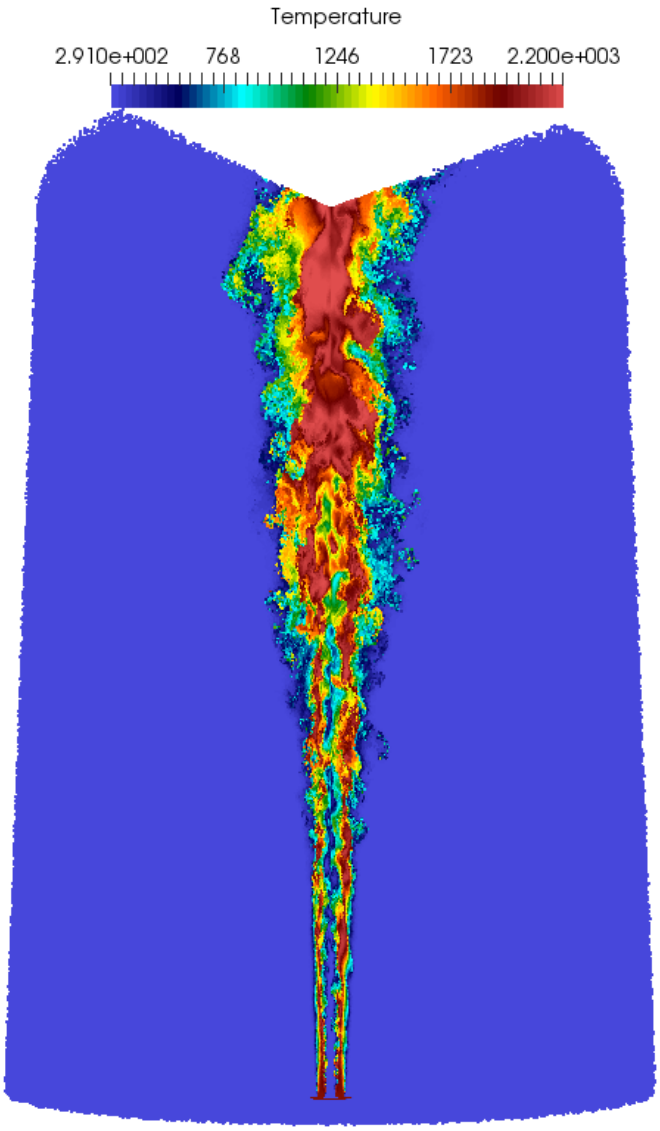

Figure 6.6: Lagrangian particles used in the Sandia Flame D simulations that are colored by the instantaneous resolved temperature at a time step after reaching a statistically stationary state.

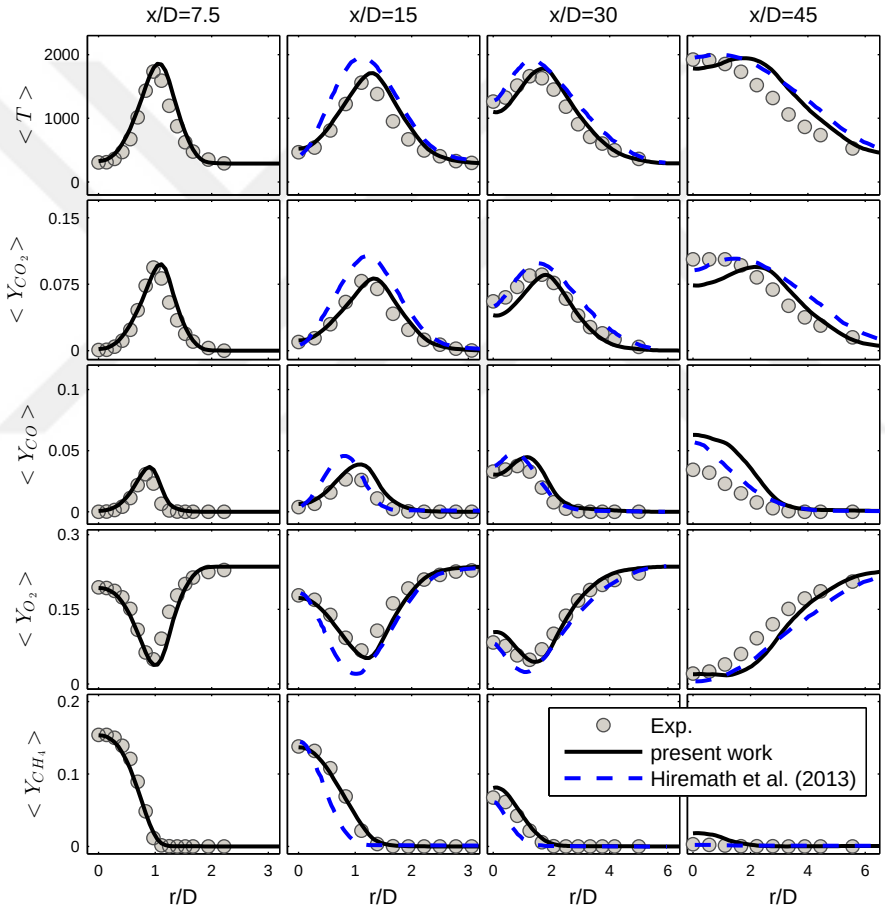

Figure 6.7: Radial profiles of time-averaged resolved temperature T and resolved species mass fractions of CO_2, CO, O_2 and CH_4 from top to bottom, at axial locations $x/D = 7.5$, 15, 30 and 45, from left to right. Symbols, the experimental data; black line, the present LES/PDF simulation; blue dashed line, the previous LES/PDF simulation.

30, the experimental data are reproduced with a slight discrepancy close to the center line. However, the trend in the results is consistent with the trend observed in the previous LES/PDF simulations. At the location of $x/D = 45$, although the trends are similar in the present and the previous LES/PDF simulations, the discrepancy between experimental data and the numerical results is visible.

Figure 6.8 shows the rms of temperature, $\langle T'' \rangle$, and species mass fractions, $\langle Y'' \rangle$, of CO_2, CO, O_2 and CH_4 together with the experimental data and the results from the previous LES/PDF simulations. Similar observations can be made for the rms values. At the locations of $x/D = 7.5$ and 15, the present LES/PDF results are in good agreement with the experimental data and markedly better than the previous LES/PDF simulations of Hiremath et al. [87]. At locations of $x/D = 30$ and 45, the rms values of the present and previous LES/PDF simulations have very similar trends: They both produced the rms values slightly smaller than those of experimental measurements.

6.5 Performance of the Velocity Correction Method

In this section, we investigate performance of the three-stage velocity correction algorithm in enforcing the consistency between the particle mass density, ρ_P^k, defined as the total particle mass in the k^{th} cell divided by the volume of the cell, and the finite volume density, ρ_{FV}^k, at the numerical solution level. In this thesis, the three-stage velocity correction method is incorporated into the LES/PDF solver for the block structured grids but it can be readily extended to the unstructured grids to perform simulations in more complex geometries such as the gas turbine combustors. It is emphasized here that this is the first study that the three-stage velocity correction method is incorporated into an LES/PDF solver for the complex geometries. Its performance is assessed through extensive simulations of a turbulent piloted jet diffusion flame (Sandia Flame D) using the fully coupled LES/PDF solver. First, performance of the each stage is examined separately and then performance of the three-stages is demonstrated. The key parameter used in the assessment of the performance of

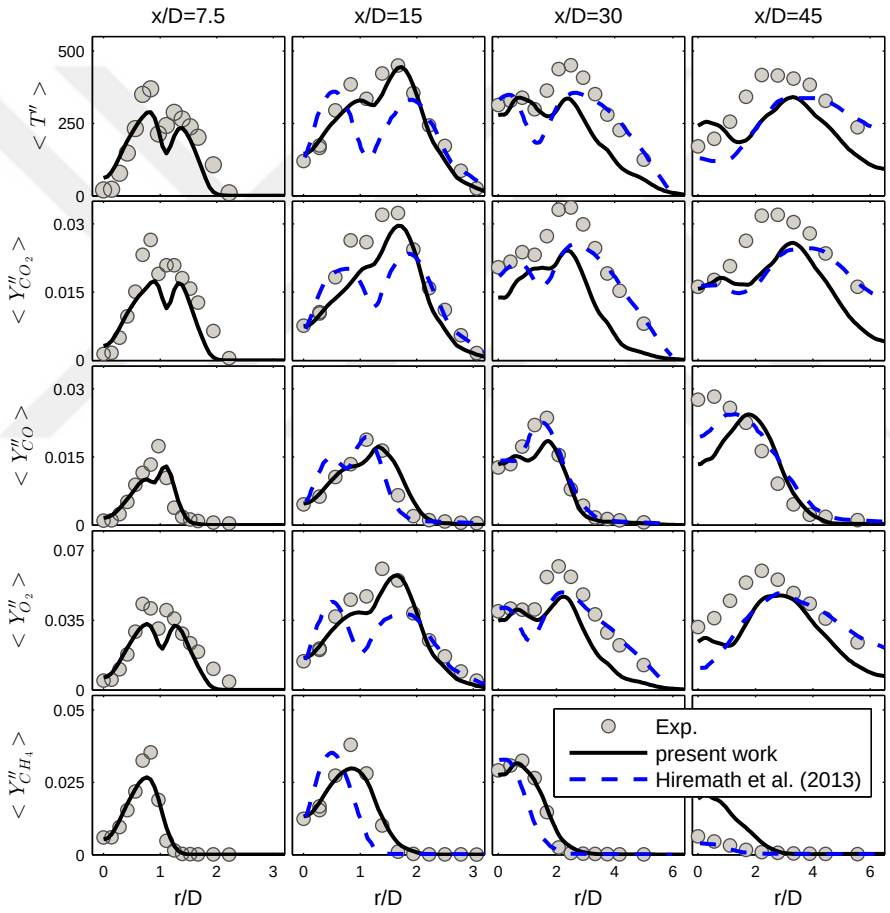

Figure 6.8: Radial profiles of time-averaged the rms of temperature and the rms of species mass fractions of CO_2, CO, O_2 and CH_4 from top to bottom, at axial locations x/D = 7.5, 15, 30 and 45, from left to right. Symbols, the experimental data; black line, the present LES/PDF simulation; blue dashed line, the previous LES/PDF simulation.

the three-stage velocity correction method is the deviation between the particle mass density, ρ_P, and the finite volume density, ρ_{FV}, defined for the k^{th} cell as [2]

$$d\rho^k \equiv \frac{\rho_P^k - \rho_{FV}^k}{\rho_{FV}^k}. \tag{6.10}$$

A global indicator can then be derived from the deviation between the particle and FV densities by taking the root-mean-square value of $d\rho^k$ over the computational domain as [2]

$$\rho_{RMS} \equiv \left(\frac{\sum_{k=1}^{N_E} \left(d\rho^k\right)^2}{N_E} \right)^{1/2}, \tag{6.11}$$

where N_E is the total number of grid cells used in the simulation.

Figure 6.9 shows the contour plot of the instantaneous deviations between particle mass and FV densities on the whole computational domain. The simulations are repeated using no correction (Stage 1), the first-level correction (Stage 1 and 2), and the second level correction (Stage 1-3) with two different relaxation time parameter of $\alpha = 25$ and $\alpha = 100$. The time relaxation parameter α is used to relax the corrections for the mass residual $R^k = (m^{k,FV} - m^{k,P})/(\alpha \Delta t)$ where Δt is the time step used in the simulation. In the simulations with no correction (Stage 1), the deviations between the particle mass and FV densities are very large. The deviations are significantly reduced in the simulations with the first-level correction (Stage 1 and 2). The improvement in the particle mass distribution with Stage 1 and 2 shows that the interpolated velocities used in the particle transport have a significant role in the consistency between the PDF and the LES solvers. Although the first-level correction reduces the deviations, there is considerable level of deviations between particle mass and FV densities. The second-level correction (Stage 1-3) further eliminates the deviations and results in very good consistency between two density fields. The two figures on the right hand side of Fig. 6.9 show the deviations in the simulations using the second-level correction with two different time relaxation parameters of α =25 and 100. The relaxation parameter is expected to be critically important in maintaining

numerical stability of the LES/PDF simulations. To determine its influence on the numerical stability and the satisfaction of the consistency condition, simulations are repeated using α =1, 10, 25 and 100. It is found that a numerical instability arises for the cases of α =1 and α =10 due to excessive correction velocities that become as large as the jet velocity at the inlet. Therefore the simulations are completed only for the values of α =25 and 100. The results are shown in Fig. 6.9. As can be seen in this figure, the deviations in the density fields in the simulations using α = 25 are smaller than those compared with α = 100. As expected, using a short relaxation time scale results in a better consistency between the particle mass and FV density fields. On the other hand, a short relaxation time scale tends to result in a numerical instability due to the excessive corrections. Therefore there is a trade off between the consistency and numerical stability, and the relaxation time scale should be selected carefully such that the consistency condition is effectively enforced while the numerical stability and robustness are maintained even in severe cases.

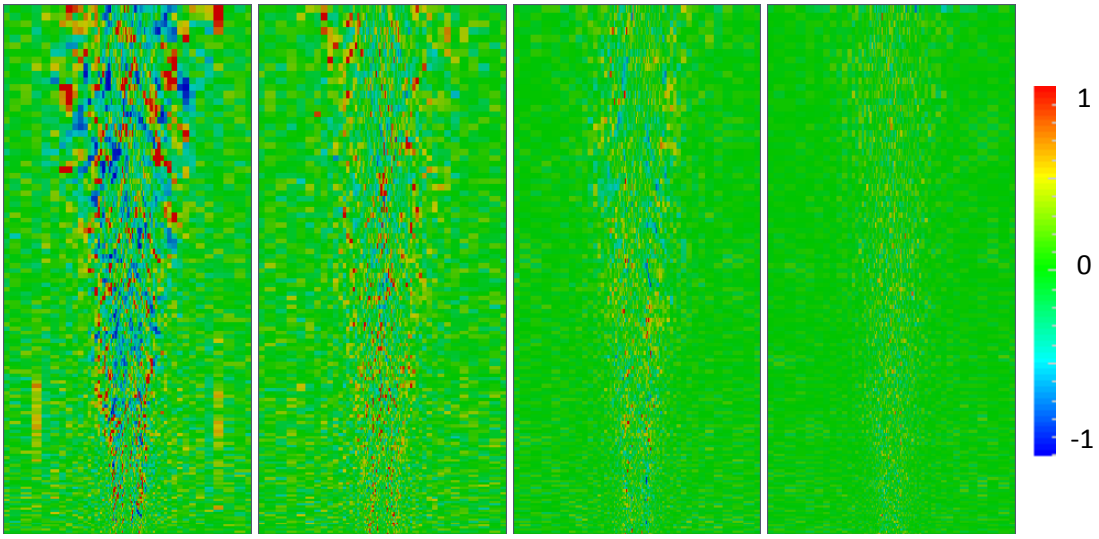

Figure 6.9: The deviation between particle mass density and FV density fields computed using (from left to right) no correction (Stage 1), the first-level correction (Stage 1 and 2), and the second-level correction (Stage 1-3) with time relaxation parameter of α=100, and the second-level correction (Stage 1-3) with time relaxation parameter of α=25.

Figure 6.10 shows the time evolution of the root-mean-square of the deviation between particle mass and FV densities in the simulations with (i) no correction (Stage 1), (ii) the first-level correction (Stage 1 and 2), (iii) the second-level correction (Stage 1-3) with time relaxation parameter of $\alpha = 25$, and (iv) the second-level correction (Stage 1-3) with time relaxation parameter of $\alpha = 100$. The simulation with no correction results in the highest deviation with about $\rho_{RMS} = 0.4$. Moreover ρ_{RMS} continues to increase slightly as simulation proceeds. The first-level correction (Stage 1 and 2) reduces the value of ρ_{RMS} by 25% compared to the case of no correction applied. Additionally, ρ_{RMS} does not seem to increase during the simulation in the case of the first-level correction. The second-level corrections (Stage 1-3) with both values of $\alpha = 25$ and $\alpha = 100$, ρ_{RMS} is reduced below 0.2. It can be also seen that the second-level correction with α =25 results in a smaller ρ_{RMS} than that with α =100. Moreover, ρ_{RMS} does not increase during the simulations in both cases of $\alpha = 25$ and $\alpha = 100$.

The performance of the three-stage correction algorithm is also investigated through the one-way coupling methodology. For this purpose, the three-stage velocity correction method is incorporated into the one-way coupled LES/PDF solver and simulations are performed for the Sandia Flame D case using various stages of the three-stage velocity correction algorithm. In particular, one-way coupled simulations are carried out using (i) no correction (Stage 1), (ii) the first-level correction (Stage 1 and 2), (iii) the second-level correction (Stage 1-3) with time relaxation parameter $\alpha = 25$, and (iv) the second-level correction (Stage 1-3) with time relaxation parameter $\alpha = 100$ and the results are compared for the consistency between the LES and particle fields. The level of consistency between the results from the LES and the PDF solvers using different stages of the three-stage velocity correction method shows the effects of each stage separately. The time-averaged resolved mixture fraction is compared first along the centerline, and then at the axial locations of $x/D = 30$ and 45. Figure 6.11 shows the time-averaged resolved mixture fraction computed by the LES and PDF solvers along the centerline. As it can be seen in this figure, the results obtained by the PDF

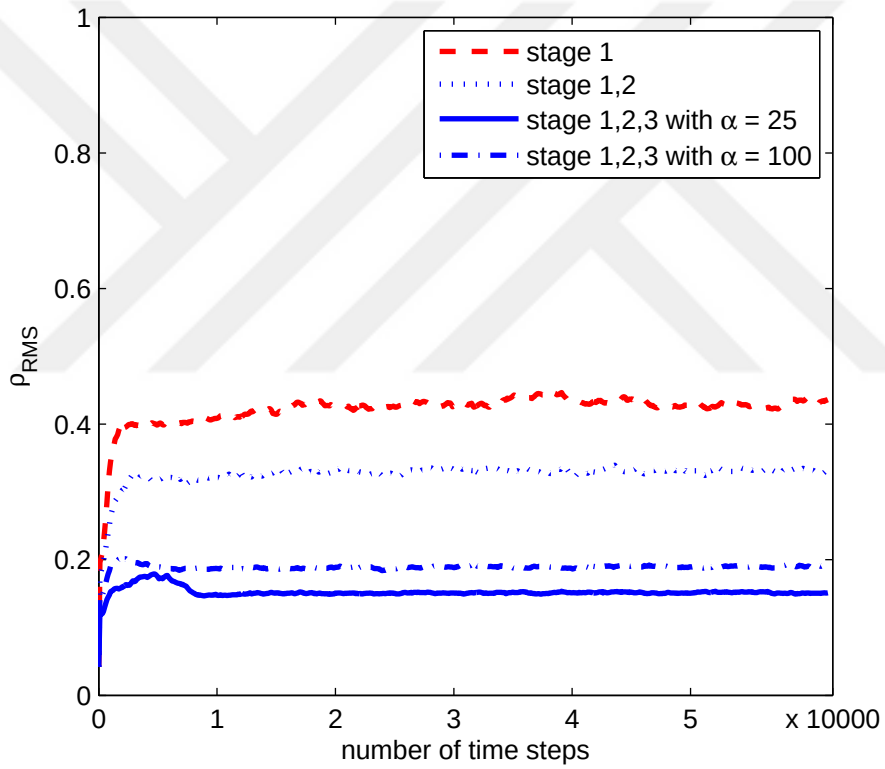

Figure 6.10: The time evolution of the rms of deviation between particle mass and FV densities ρ_{RMS}. Red dashed line, no correction (Stage 1); blue dashed line, the first-level correction (Stage 1 and 2); blue dashed dot line, the second-level correction (Stage 1-3) with α =100; blue solid line, the second-level correction (Stage 1-3) with α =25.

solver with no correction (Stage 1) significantly deviate from the result calculated by the LES solver. The first-level correction (Stage 1 and 2) greatly improves the consistency between the LES and PDF results, but very slight discrepancies appear at the axial locations of x/D =15 and 30. These discrepancies are completely removed when the second-level correction (Stage 1-3) with α =25 is applied yielding excellent agreement between the LES and PDF fields. To show the effects of the relaxation time scale parameter α, simulations are also performed for $\alpha = 25$ and $\alpha = 100$, and the results are compared in Fig. 6.12. This figure shows that the second-level correction with α =100 yields overall good consistency between the LES and PDF solutions. However the discrepancy slightly increases as α increases from $\alpha = 25$ to $\alpha = 100$.

The radial profiles of the time-averaged resolved mixture fraction $\left\langle \tilde{\xi} \right\rangle$ from the LES solver and the PDF solver using different levels of correction are plotted in Fig. 6.13. In addition, Fig. 6.12 also shows that results from the PDF solver using the second-level correction (Stage 1-3) with $\alpha = 25$ are found to be in excellent agreement with the results from the LES solver at both of the axial locations. The results from the PDF solver using the first-level correction (Stage 1 and 2) are in very good agreement with the results from the LES solver. At the axial location of $x/D = 30$, the PDF results are slightly smaller than those from the LES solver close to the centerline. The results from the PDF solver using no correction (Stage 1) generally follow the trend in the results from the LES solver. However, there are significant discrepancies between the LES and PDF results in this case.

In conclusion, the first-level (Stage 1 and 2) and the second-level (Stage 1-3) corrections significantly improve the consistency between the LES and the PDF solvers. For the Sandia flame D case, the second level correction results in about 50% less error compared to the first level correction in terms of the rms of deviations between the particle and FV density fields. The one-way coupled LES/PDF simulations of the Sandia flame D performed using the first-level and the second-level corrections indicate that both levels yield good consistency between the LES and PDF fields.

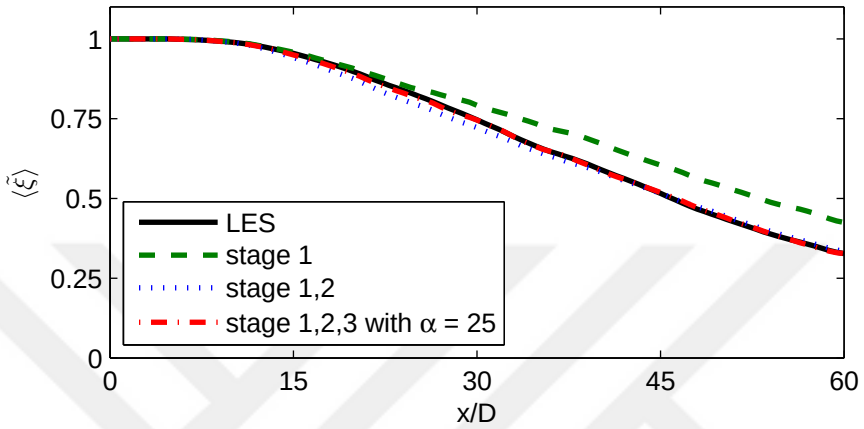

Figure 6.11: The LES and PDF results of the time-averaged resolved mixture fraction along the centerline for the Sandia Flame D. Solid line, LES; dashed line, PDF with no correction (Stage 1), dotted line, PDF with the first-level correction (Stage1 and 2), dotdash line, PDF with the second-level correction (Stage 1-3) with $\alpha = 25$.

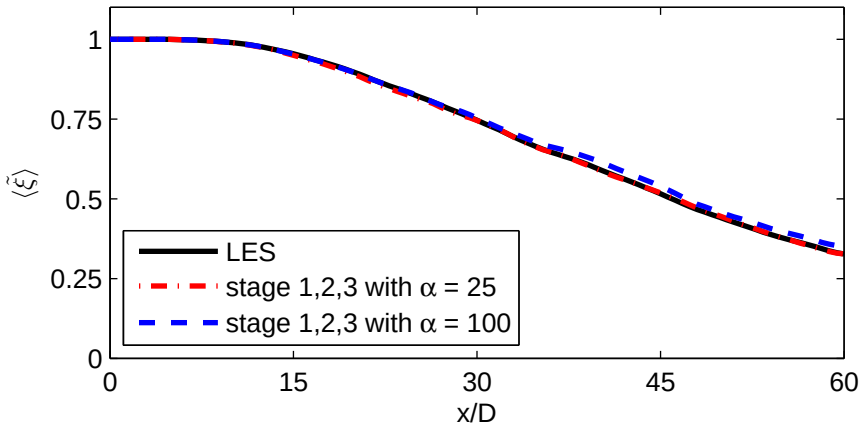

Figure 6.12: The LES and PDF results of the time-averaged resolved mixture fraction along the centerline for the Sandia Flame D. Solid line, LES; dashed line: PDF with the second-level correction (Stage 1-3) with $\alpha = 100$; dotdash line, PDF with the second-level correction (Stage 1-3) with $\alpha = 25$.

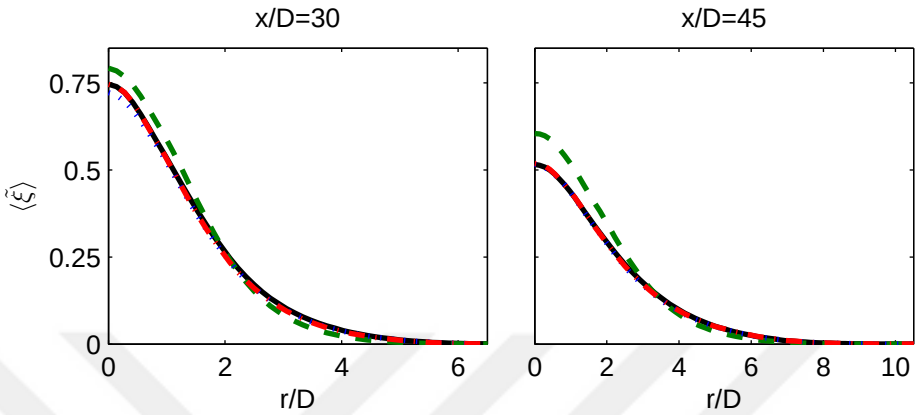

Figure 6.13: The LES and PDF results of the radial profiles of the time-averaged resolved mixture fraction at two different axial locations, left: x/D=30 and right: x/D=45 for the Sandia Flame D. Solid line, LES; dashed line, PDF with no correction (Stage 1), dotted line, PDF with the first-level correction (Stage 1 and 2), dotdash line, PDF with the second-level correction (Stage 1-3) with $\alpha = 25$.

However, the simulation with the second-level correction results in a slightly better consistency than the results computed using only the first-level correction.

6.6 Computational Cost

In this study, the simulations are performed using a 256×128×32 cylindrical-type block structured grid as shown in Fig. 6.2 with about 20 particles per cell. The computational domain is decomposed into 96 subdomains and simulations are performed using 48 CPUs of 2.40GHz Intel Xeon with multithreading technique (96 threads in total). The simulations are carried out for ten flow-through times based on the fuel jet bulk velocity to reach a statistically stationary state, and then an additional ten flow-through times were performed to collect the statistics. In total, about 100,000 time steps are marched in each simulation and the simulations are completed in 12 days wall-clock time. The relative computational cost of each component of the LES/PDF simulations is presented in Fig. 6.14. As can be seen in this figure, about 85% of the total computational time is consumed by the PDF solver. Additionally, 85% of the

computational time of the PDF solver is consumed by the three main processes of transport $\mathbb{T}$, mixing $\mathbb{M}$ and reaction $\mathbb{R}$. The reaction module of the PDF solver consumes about 30% of the total computational time whereas the mixing and transport processes consume about 20% and 22% of the total computational time, respectively. The LES solver consumes only 15% of the total computational time. The computational time elapsed by the new LES/PDF solver is of the same order of those reported in the previous LES/PDF simulations [[3, 32, 33]].

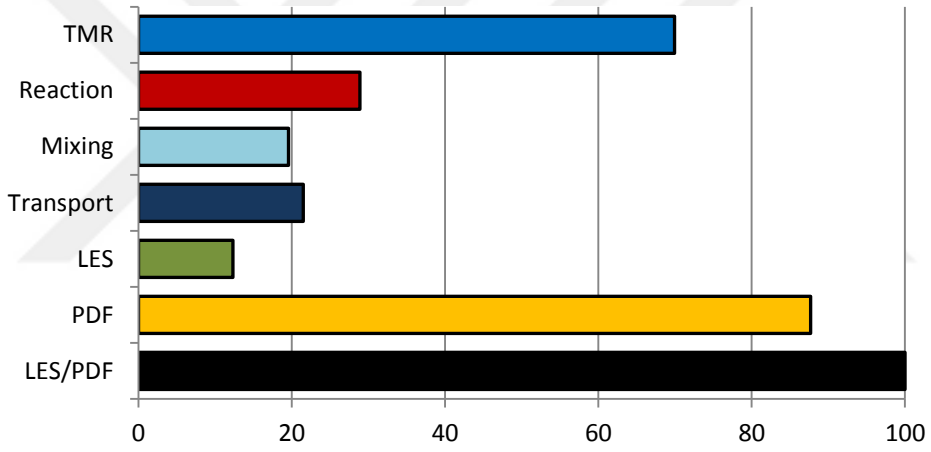

Figure 6.14: The percentage of computational cost of LES and PDF solver as well as the transport $\mathbb{T}$, mixing $\mathbb{M}$ and reaction $\mathbb{R}$ calculations in PDF solver. $\mathbb{TMR}$ represent the total percentage of elapsed time of transport, mixing and reaction in PDF solver.

In this section, we also examine the computational cost of the three-stage velocity correction method. The computational cost required by each stage in the method is investigated separately. Here, we first define the computational cost of using each stage of the velocity correction method, and then give relative cost of each stage. The cost for Stage 1 consists of the cost of interpolation of the LES velocities first from the cell centers to the cell vertices and then from cell vertices onto the particle locations, and the cost of tracking particles in the computational domain. The cost of using the Stage 2 correction is equal to the cost of solving a linear system of equations for each cell to calculate the Stage 2 velocity corrections at cell vertices. Finally

Stage 3 requires solving an equation similar to the discrete pressure Poisson equation to obtain the Stage 3 velocity corrections at the cell centers, and then moving the particles with this correction velocity using the Stage 1 and 2. In Fig. 6.15, the time consumed by each stage is presented. As seen, the Stage 1 requires a considerable amount of time since it performs the tracking of the particles in the computational domain. The additional cost for using the Stage 2 correction is about 8% of the cost of the Stage 1. However, using the Stage 3 correction requires more than the total cost of Stage 1 and 2.

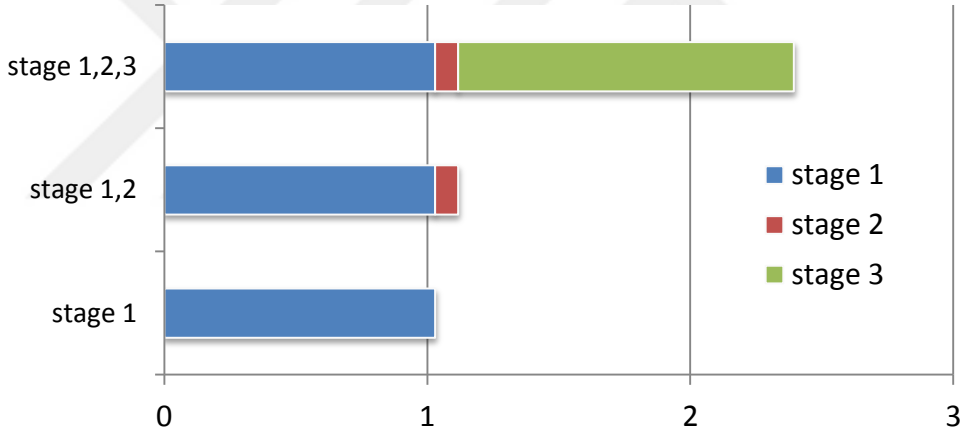

Figure 6.15: The elapsed time by the particle transport module in the PDF solver per time step in seconds. The blue bar, the time elapsed by the Stage 1; the red bar, the time elapsed by the Stage 2 and the green bar, the time elapsed by the Stage 3.

Chapter 7

THE CAMBRIDGE STRATIFIED FLAMES

In many practical combustion devices, the combustion occurs in a stratified regime in which the fuel concentration varies in the physical space. This stratification could be due to the design constraints or insufficient time to mix the fuel and oxidizer completely. On the other hand, the stratification could be created intentionally to increase the flame stabilization in the lean combustion. Haworth et al. [88] and Jimenez et al. [89] have described the main characteristics of a stratified flame. The schematic in Fig. 7.1 shows the main characteristics of a stratified flame. A primary premixed flame front propagates into reactants whose concentrations vary in space. Behind the flame front, the fuel-rich reactant results in hot products and fuel fragments whereas the fuel-lean reactant produces hot products and O_2. Thus behind the primary flame front, the hot fuel fragments and O_2 create the secondary flame zone.

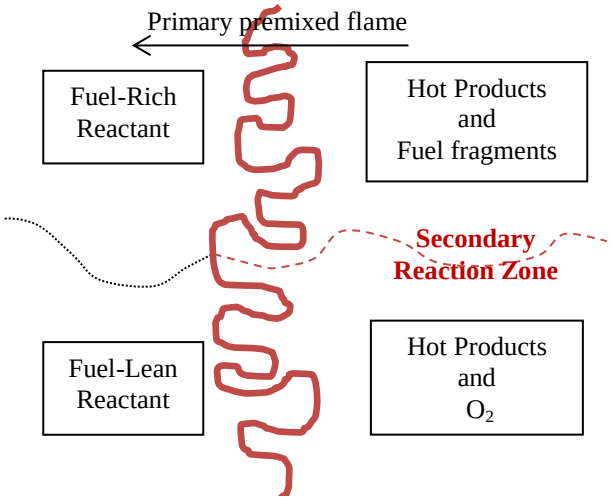

Figure 7.1: A schematic of turbulent flame propagation into a stratified fuel concentration.

In the literature, the turbulent combustion models have been developed mainly for the two canonical regimes: i) non-premixed combustion in which the fuel and oxidizer are completely segregated before reaction takes place, and ii) premixed combustion in which the fuel and oxidizer are perfectly mixed beforehand. Common occurrence in practical devices and the potential benefits to increase the stability in the lean combustion have increased the motivation for modeling the stratified turbulent flames. Generally the models for the stratified combustion are developed by extending the existing models for the premixed combustion. Proch and Kempf [90] developed an artificially thickened flame method with a tabulated chemistry and Nambully et al. [91, 92] have developed a model based on the mixture fraction and a progress variable. The two methods were successful to predict the main properties in the turbulent reacting flow.

The PDF method is a regime independent method since the chemical reaction source term is in the closed form. Therefore the PDF method has a great potential to successfully model the premixed, nonpremixed and stratified turbulent flames without requiring any modifications. We apply the new LES/PDF solver to a bluff-body burner from the Cambridge Stratified Flame series. We first describe the experimental configuration briefly and then present the LES/PDF simulation results.

7.1 Experimental Configuration

The schematic of burner is shown in Fig. 7.2. The burner consists of a central bluff body surrounded by two annular fuel jets, i.e., the inner and the outer jets. In the most annulus, air-coflow is supplied to prevent entrainment of the ambient air. The dimensions of the burner are summarized in Table 7.1. The concentrations of the fuel from the inner and the outer jets are varied systematically to investigate the effects of the stratification. The fuel concentration configurations are given in Table 7.2. The bulk velocity at the inlets are given in Table 7.3. The flames are stabilized by a recirculation behind the bluff body. More details about this flame are available in Sweeney et al. [5, 93].

Table 7.1: Dimensions of the stratified bluff body burner.

Bluff body diameter	=	12.7 mm
Inner jet annulus diameter	=	23.6 mm (wall thickness = 0.9 mm)
Outer jet annulus diameter	=	34.8 mm (wall thickness = 0.9 mm)

Table 7.2: The equivalence ratio in the inner and the outer fuel jets in the stratified bluff body burner [5].

Case	ϕ_i	ϕ_o
SwB1	0.75	0.75
SwB5	1.0	0.5
SwB9	1.125	0.375

Table 7.3: Bulk velocities at the inlets and corresponding reynolds numbers [5].

	U_{bulk}	Corresponding Reynolds number
inner fuel jet	8.31	5960
outer fuel jet	18.7	11500
air coflow	0.4	-

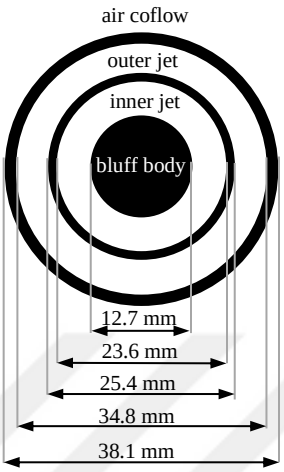

Figure 7.2: A schematic of the stratified bluff body burner [5].

7.2 Computational Setup

The computational domain is selected to be [200mm]×[100mm]×[0,2π] in the axial (x), radial (r) and azimuthal (θ) directions, respectively. The domain is discretized using a non-uniform 192×96×32 block structured cylindrical-type grid. The grid is concentrated near the nozzle in axial direction and in the shear region between the fuel jets in the radial direction.

In the fuel jets, the instantaneous inlet velocities are obtained from two separate turbulent pipe flow simulations. We use the same method as explained in the previous chapter to interpolate the inlet velocities from the turbulent pipe flow simulations. The inlet velocity of the air-coflow is set to a value of 0.4 m/s. At the bluff body and wall-lips, the slip boundary conditions are applied. At the outlet, the zero-gradient boundary conditions are imposed for all the fields while the slip boundary conditions are used at the far field, i.e., on the lateral surface. In the PDF solver, about 40 particles per cell are used due to the complex flow fields of recirculation behind the bluff body.

7.3 Results

The numerical results from the simulation with the detailed chemistry calculations are presented in this section. For the methane/air combustion, the ARM1 [4] chemistry mechanism is used. Figure 7.3 presents the time-averaged radial profiles of resolved axial velocity $\left\langle \tilde{U} \right\rangle$ and the rms of the resolved axial velocity $\left\langle \tilde{u''} \right\rangle$ at four axial locations of x = 2, 10, 30 and 50 mm. The mean axial velocity profiles are in good agreement with the experimental measurements at the locations of x = 2, 10, 30 mm. Close to the centerline the numerical results are slightly bigger than the experimental measurements for all the three locations. At the axial location of x = 50 mm, the numerical results are evidently bigger than the experimental data. The rms of the resolved axial velocity is in good agreement at the locations of x = 2 mm and 10 mm. The trend of the rms velocity is similar to the trend in the experimental data but the numerical results significantly overpredict the experimental measurements, especially in the downstream locations of x = 30 mm and 50 mm .

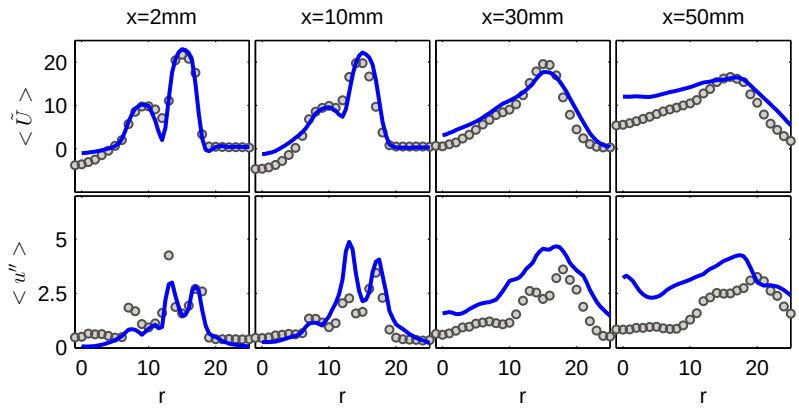

Figure 7.3: The radial profiles of time-averaged resolved axial velocity (top), resolved turbulence intensity (bottom) at four axial location of x =2, 10, 30 and 50 mm. The symbols: The experimental data; solid line: The LES/PDF results.

Figure 7.4 shows the time-averaged radial profiles of the resolved temperature $\left\langle \tilde{T} \right\rangle$ at the axial locations of x = 10, 20, 30, 40 and 50 mm. At the axial locations

of $x = 10$, 20 mm, the radial profiles of the mean temperature match well with the experimental data. At the axial location of $x = 30$ mm, the radial profile of mean temperature is in agreement with the experimental data but slight discrepancy appears in the gradient of the mean temperature. At the axial location of $x = 40$ and 50 mm the trend in the radial profiles of the mean temperature is similar to the experimental data but the peak temperatures are underestimated and also the gradients of the mean temperature in the radial profiles are not reproduced well in the numerical results. The radial profiles of the rms temperature are shown in Fig. 7.5. The peak of the rms temperature in the radial profiles are lower than the peak of the experimental measurements at all the axial locations. The width of the rms temperature profiles at the locations of $x = 30$, 40 and 50 mm are larger than that in the experimental data which is consistent with the discrepancy observed in the gradient of the mean temperature radial profiles at these locations.

The time-averaged radial proles of mass fractions of $\left\langle \tilde{Y}_{CO_2} \right\rangle$ and $\left\langle \tilde{Y}_{CO} \right\rangle$ are plotted in Fig. 7.4. The observations for the mean $\tilde{Y}_{CO_2}$ profiles are very similar to the observations for the mean temperature profiles. However the peak of the radial profiles of mean $\tilde{Y}_{CO_2}$ are smaller than the experimental data. At the axial locations of $x = 10$ mm, 20 mm, the results are in good agreement with the experimental measurement while at the locations $x = 30$, 40 and 50 mm discrepancies in the gradient of the radial profiles appear as in the case of the mean temperature. The maximum value of the radial profiles of the mean $\tilde{Y}_{CO}$ are in good agreement with the maximum values of the experimental data. At the locations of $x = 10$, 20 mm, the radial profiles match with the experimental data very well, however, at locations of $x = 30$, 40 and 50 mm, the width of the radial profiles is larger than that of the experimental data as was also the case of the rms temperature profiles. The rms of the mass fraction of $\left\langle \tilde{Y''}_{CO_2} \right\rangle$ and $\left\langle \tilde{Y''}_{CO} \right\rangle$ are presented in Fig. 7.5. As observed in the rms temperature profiles, the rms mass fraction profiles are wider than the profiles of the experimental data. Additionally, the maximum values of the rms of the mass fraction profiles are smaller than those of the experimental data.

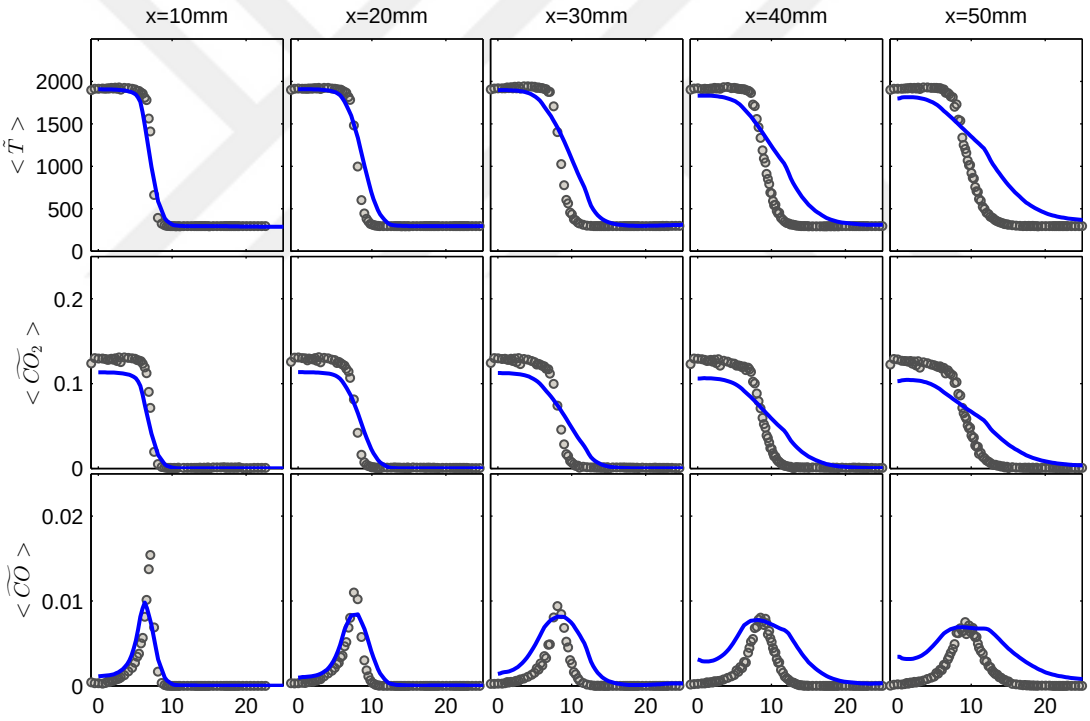

Figure 7.4: The radial profiles of the time-averaged resolved temperature and the resolved mass fractions of CO_2 and CO at four axial location of x=10, 20, 30 and 50 mm. The symbols: The experimental data; The solid line: The LES/PDF results.

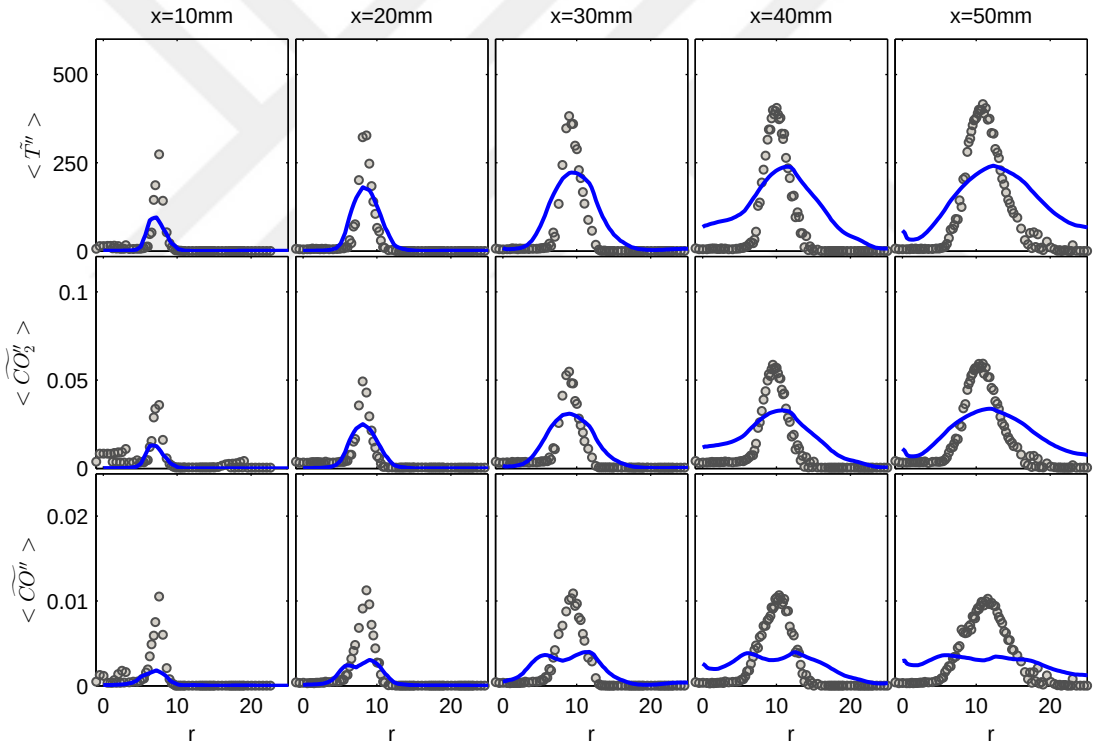

Figure 7.5: The radial profiles of the time-averaged rms of temperature and the rms of mass fraction of CO2 and CO at four axial location of x=2, 10, 30 and 50 mm. The symbols: The experimental data; The solid line: The LES/PDF results.

Chapter 8

CONCLUSIONS AND FUTURE DIRECTION

8.1 Conclusions

The PDF method has been shown to be superior model for the prediction of turbulent reacting flows. In this thesis, a general purpose LES/PDF methodology is developed for the simulations of turbulent reacting flows in complex geometries. The LES/PDF solver consists of two components (i) a finite volume method based LES solver, and (ii) a Lagrangian Monte Carlo method based PDF solver. The two components of the hybrid LES/PDF solver are developed entirely within the OpenFOAM framework. In literature, this is the first general purpose LES/PDF solver developed entirely within an open-source library. The OpenFOAM library is chosen as a working platform due to its large range of physical modules such as soot formation and evaporation. The new LES/PDF solver has the capability of performing the detailed chemistry calculations. In situ adaptive tabulation (ISAT) method developed by Pope [1] is incorporated to accelerate the detailed chemical kinetics calculations. The three-stage velocity correction method [2] is also incorporated into the LES/PDF solver for the block structured grids. This is the first time that the three-stage velocity correction is implemented and truly tested in the LES/PDF methodology in the block structured grids.

The accuracy and the numerical consistency of the LES and the PDF solvers are examined through the one-way coupling method [3]. For this purpose, a turbulent piloted methane/air jet diffusion flame (Sandia Flame-D) simulations are performed using a simple flamelet chemistry model. The fields of the resolved mixture fraction and temperature calculated by the LES and the PDF solvers are compared. The results from the two solvers are in very good agreement demonstrating the accuracy

of the numerical methods in the LES and the PDF solvers as well as their consistency. The performance of the three-stage velocity correction method is examined to show the effects of the each stage on the numerical accuracy and the consistency of the two solvers. The first-level correction is found to be very efficient in reducing the numerical error and enforcing the consistency between the LES and the PDF solvers. Furthermore, the second-level correction is found to be very effective in eliminating any deviation between the mass densities of the LES and the PDF solvers, which mat crucially important especially in the case of complex flows involving swirling and recirculation regions. Additionally, the computational cost required by each stage is also investigated. The computational cost of the first-level correction is defined as the time required to solve the linear equation system to determine the first-level velocity correction. It is found that the first-level correction increases the computational time consumed by the particle tracking algorithm only by 8%. However, the second-level correction increases the computational cost of the particle tracking by two folds. Because the second-level correction solves an equation in the same form as the discrete pressure equation, and then the Stage 1 and 2 are used again to move the particles with the second-level correction velocities.

The Sandia Flame-D simulations are performed using the new LES/PDF solver with the detailed chemistry representation. The ISAT method is employed in the detailed chemical kinetics calculations. The methane/air combustion is described with an augmented reduced mechanism (ARM1) consisting of 12 steps and 16 species [4]. It is found that the numerical results are in very good agreement with the experimental measurements. The statistical moments of the key chemical species are also predicted quite accurately. The results from the new LES/PDF solver match with the experimental measurements better than those from the previous LES/PDF simulations [87]. The improvement in the numerical results can be attributed to the performance of the particle tracking and the velocity correction methods used in the present PDF solver.

The computational cost of the new LES/PDF solver on block structured grid

is also examined. The PDF component of the LES/PDF solver consumes 85% of the total computational time consumed by the LES/PDF solver. The ratio of the computational cost of the PDF component to the cost of the LES/PDF solver is in the same order of the ratio of the previous PDF solver [33]. This indicates that the new PDF solver on a block structured grid, and employing the three-stage velocity correction can be computationally as efficient as the previous PDF solver of Wang and Pope [3] on a simple structured grid without any velocity correction algorithm.

Finally, the new LES/PDF solver with the detailed chemistry representation is applied to study a turbulent premixed flame from the Cambridge turbulent stratified flame series [5]. The methane/air combustion is described using the ARM1 chemical mechanism as used in the Sandia Flame-D simulations. The results are found to be in reasonably good agreement with the experimental data. The recirculation zone, and the temperature profiles are predicted accurately at the upstream locations close to bluff body. However, some discrepancies are apparent between the numerical results and the experimental data at the downstream locations. This could be attributed to the fact that the model coefficient used in the IEM mixing model is not optimal.

8.2 Recommendations for Future Work

The general purpose LES/PDF solver on a block structured grid for a complex geometry is found to be very efficient in the simulations of the turbulent reacting flows. Moreover, its predictive capability and the order of accuracy of the numerical schemes used can be further improved by conducting some future work as summarized below:

1. The new LES/PDF solver is developed for turbulent combustion simulations in complex geometries using block structured hexahedral computational cells. The solver can be straightforwardly extendable to unstructured grids. Then the performance of the solver on unstructured grid should be tested in the future.

2. In this work we used unity Lewis number assumption for all the chemical species, thus the differential diffusivity effects are neglected. Barlow [94] has reported

that the differential diffusivity of species has strong effect on the recirculation zones, thus the differential diffusivity should be considered in the simulations of flows dominated by recirculation region. In the LES/PDF solver, the differential diffusivity can be implemented by following the work by McDermott and Pope [60].

3. In the PDF solver, the particle equations are solved by the first order time stepping method. Although Wang and Pope [3] have reported that the first order method performs as well as the second order methods, Popov and Pope [83] have reported that the second order particle transport methods increase the consistency between the PDF and LES solvers. Wang et al. [75] have presented various second order particle tracking methods. In terms of computational efficiency, the method developed by Cao and Pope [73] can be implemented on the unstructured grids while the others increase the computational cost significantly. As a future work, the second order time stepping method, namely $\mathbb{TMRMT}$, can be implimented to achieve the second order accuracy in the present LES/PDF method.

4. The parallelization in the present LES/PDF method is performed by decomposition of the computational domain such that each subdomain has about the same number computational cell (thus the same order of number of particles). This significantly balances the load in the LES solver and the particle transport and mixing in PDF solver. However, the load due to chemical reactions in the PDF solver performed by the ISAT module may not be optimized since some regions may include stiff chemical reactions (for example subdomains including the flame sheat between pilot flame and fuel jet) but in some regions chemical reactions may not take place at all (for example in a subdomain including only air-coflow). Dynamic load balancing can be done to optimize the computational load in all subdomains.

BIBLIOGRAPHY

[1] S. Pope, Computationally efficient implementation of combustion chemistry using In Situ Adaptive Tabulation, Combustion Theory and Modelling 1 (1997) 41–63.

[2] Y. Z. Zhang, D. C. Haworth, A general mass consistency algorithm for hybrid particle/finite-volume PDF methods, Journal of Computational Physics 194 (2004) 156–193.

[3] H. Wang, S. Pope, Large eddy simulation/probability density function modeling of a turbulent $CH_4/H_2/N_2$ jet flame, Proceedings of the Combustion Institute 33 (2011) 1319–1330.

[4] C. J. Sung, C. K. Law, J. Y. Chen, An augmented reduced mechanism for methane oxidation with comprehensive global parametric validation, Proceedings of the Combustion Institute 27 (1998) 295–304.

[5] M. S. Sweeney, S. Hochgreb, M. J. Dunn, R. S. Barlow, The structure of turbulent stratified and premixed methane/air flames i: Non-swirling flows, Combustion and Flame 159 (2012) 2896–2911.

[6] H. P. Miller, R. Mitchell, M. Smooke, R. Kee, Towards a comprehensive chemical kinetic mechanism for the oxidation of acetylene: comparison of model predictions with results from flame and shock tube experiments, 19th Symp. (Int.) on Combustion, The Combustion Institute, Pittsburgh 19 (1982) 181–196.

[7] R. S. Cant, E. Mastorakos (Eds.), An introduction to turbulent reacting flows, Imperial College Press, London, 2008.

[8] T. Poinsot, D. Veynante (Eds.), Theoretical and Numerical Combustion, Edwards Press, Philadelphia., 2005.

[9] S. Pope, PDF methods for turbulent reactive flows, Progress in Energy and Combustion Science 11 (1985) 119–192.

[10] W. Meier, R. S. Barlow, Y.-L. Chen, J.-Y. Chen, Raman/ Rayleigh/ LIF measurements in a turbulent $CH_4/ H_2/N_2$ jet diffusion flame: Experimental techniques and turbulence-chemistry interaction, Combustion and Flame 123 (2000) 326–343.

[11] S. R. Turns (Ed.), An Introduction To Combustion, Concepts and Applications, M Graw Hill, Singapure, 2000.

[12] S. B. Pope (Ed.), Turbulent Flows, Cambridge University Press, Cambridge, 2000.

[13] H. Pitsch, Large-eddy simulation of turbulent combustion, Annual Review of Fluid Mechanics 38 (2006) 453–482.

[14] A. N. Kolmogorov (Ed.), The local structure of turbulence in incompressible viscous fluid for very large Reynolds numbers, SSSR, Dokl. Akad. Nauk, 1941.

[15] P. Moin, J. Kim, Numerical investigation of turbulent channel flow, Journal of Fluid Mechanics 118 (1982) 341–371.

[16] K. Akselvoll, P. Moin, Large eddy simulation of a backward facing step flow, Engineering Turbulence Modeling and Experiments 6 (1993) 303313.

[17] H. Pitsch, O. Desjardins, G. Balarac, M. Ihme, Large-eddy simulation of turbulent reacting flows, 46th AIAA Aerospace Sciences Meeting and Exhibit 7 (2008) 303313.

[18] V. Raman, H. Pitsch, A consistent LES/filtered-density function formulation for the simulation of turbulent flames with detailed chemistry, Proceedings of the Combustion Institute 31 (2007) 1711–1719.

[19] H. Pitsch, Improved pollutant predictions in large-eddy simulations of turbulent non-premixed combustion by considering scalar dissipation rate fluctuations, Proceedings of the Combustion Institute 29 (2002) 1971–1978.

[20] A. W. Cook, J. J. Riley, G. Kosaly, A laminar flamelet approach to subgrid-scale chemistry in turbulent flows, Combustion and Flame 109 (1997) 332–341.

[21] S. Navarro-Martinez, A. Kronenburg, Conditional moment closure for large eddy simulations, Flow, Turbulence and Combustion 75 (2005) 245–274.

[22] S. H. Kim, H. Pitsch, Conditional filtering method for large-eddy simulation of turbulent nonpremixed combustion, Flow, Turbulence and Combustion 17 (10).

[23] C. Pierce, Progress-variable approach for large-eddy simulation of turbulent combustion, Ph.D. thesis, Stanford University (2001).

[24] S. Pope, Computations of turbulent combustion: Progress and challenges, Proceedings of the Combustion Institute 23 (1990) 591–612.

[25] D. Veynantea, L. Vervisch, Turbulent combustion modeling, Progress in Energy and Combustion Science 28 (2002) 193–266.

[26] J. Xu, S. Pope, Assessment of numerical accuracy of PDF/Monte Carlo methods for turbulent reacting flows, Journal of Computational Physics 152 (1999) 192–230.

[27] J. Xu, S. Pope, PDF calculations of turbulent nonpremixed flames with local extinction, Combustion and Flame 123 (2000) 281–307.

[28] M. Muradoglu, S. B. Pope, D. A. Caughey, The hybrid method for the pdf equations of turbulent reactive flows: consistency conditions and correction algorithms, Journal of Computational Physics 172 (2001) 841–878.

[29] P. Colucci, F. Jaberi, P. Givi, S. Pope, Filtered density function for large eddy simulation of turbulent reacting flows, Pyhsics of Fluids 10 (1998) 499–515.

[30] V. Raman, H. Pitsch, R. O. Fox, Hybrid large-eddy simulation/Lagrangian filtered-density-function approach for simulating turbulent combustion, Combustion and Flame 143 (2005) 56–78.

[31] Y. Yang, H. Wang, S. Pope, J. Chen, Large-eddy simulation/probability density function modeling of a non-premixed CO/H_2 temporally evolving jet flame, Proceedings of the Combustion Institute 34 (2012) 1241–1249.

[32] R. Tirunagari, S. B. Pope, An investigation of turbulent premixed counterflow flames using large-eddy simulations and probability density function methods, Combustion and Flame 166 (2016) 229–242.

[33] J. Kim, S. Pope, Effects of combined dimension reduction and tabulation on the simulations of a turbulent premixed flame using a large-eddy simulation/probability density function method, Combustion Theory and Modelling 18 (3) (2014) 388–413.

[34] F. Jaberi, P. Colucci, S. James, P. Givi, S. Pope, Filtered mass density function for large-eddy simulation of turbulent reacting flows, Journal of Fluid Mechanics 401 (1999) 85–121.

[35] M. Sheikhi, T. Drozda, P. Givi, S. Pope, Velocity-scalar filtered density function for large eddy simulation of turbulent flows, Physics of Fluids 15 (2003) 2321–2337.

[36] N. Ansari, G. M. Goldin, M. R. H. Sheikhi, P. Givi, Filtered density function simulator on unstructured meshes, Journal of Computational Physics 230 (2011) 7132–7150.

[37] A. Gupta, Large-eddy simulation of turbulent flames with radiation heat transfer, Ph.D. thesis, The Pennsylvania State University (2011).

[38] OpenFOAM, The open source CFD toolbox, OpenFOAM, http://www.openfoam.com/ (2004–2015).

[39] C. Celis, L. F. F. Silva, Study of mass consistency les/fdf techniques for chemically reacting flows, Combustion Theory and Modelling 19 (2015) 465–494.

[40] C. T. Bowman, R. K. Hanson, D. F. Davidson, et al., GRI Mechanism 2.1, http://www.me.berkeley.edu./grimech.

[41] L. F. Richardson (Ed.), Weather Prediction by Numerical Process, Cambridge University Press, Cambridge, 1922.

[42] A. N. Kolmogorov, A refinement of previous hypotheses concerning the local structure of turbulence in a viscous incompressible fluid at high reynolds number, Journal of Fluid Mechanics 13 (1962) 82–85.

[43] J. Chen, Petascale direct numerical simulation of turbulent combustion fundamental insights towards predictive models, Proceedings of the Combustion Institute 33 (2011) 99–123.

[44] R. Grout, A. Gruber, C. Yoo, J. Chen, Direct numerical simulation of flame stabilization downstream of a transverse fuel jet in cross-flow, Proceedings of the Combustion Institute 33 (2011) 1629–1637.

[45] C. Yoo, Z. Luo, T. Lu, H. Kim, J. Chen, A dns study of ignition characteristics of a lean iso-octane/air mixture under hcci and saci conditions, Proceedings of the Combustion Institute 34 (2013) 2985–2993.

[46] P. R. Spalart, S. R. Allmaras, A one-equation turbulence model for aerodynamic flows, AIAA JOURNAL 92 (0439).

[47] W. P. Jones, B. E. Launder, The prediction of laminarization with a two-equation model of turbulence, International Journal of Heat and Mass Transfer 15 (1972) 301–314.

[48] D. C. Wilcox, Formulation of the k turbulence model revisited, International Journal of Heat and Mass Transfer 46 (2008) 2823–2838.

[49] F. R. Menter, Two-equation eddy-viscosity turbulence models for engineering applications, AIAA Journal 32 (1994) 1598–1605.

[50] F. R. Menter, The turbulent burning velocity for large-scale and small-scale turbulence, Journal of Fluid Mechanics 384 (1999) 107–132.

[51] D. B. Spalding, Development of the eddy-break-up model of turbulent combustion, The Combustion Institute, 384 (1976) 1657–1663.

[52] B. F. Magnussen, B. H. Mjertager, On mathematical modeling of turbulent combustion, The Combustion Institute 384 (1976) 719–727.

[53] D. Haworth, Progress in probability density function methods for turbulent reacting flows, Progress in Energy and Combustion Science 36 (2010) 168–259.

[54] S. Subramaniam, S. B. Pope, A mixing model for turbulent reactive flows based on euclidean minimum spanning trees, Combustion and Flame 11 (1998) 487–514.

[55] R. O. Fox, On velocity-conditioned scalar mixing in homogeneous turbulence, Pyhsics of Fluids 8 (1996) 2678–2692.

[56] S. B. Pope, A model for turbulent mixing based on shadow-position conditioning, Pyhsics of Fluids 25 (110803).

[57] J. Villermaux, J. C. Devillon, Representation de la coalescence et de la redispersion des domaines de segregation dans un fluide par un modele dinteraction phenomenologique, Proceedings of the 2nd International Symposium on Chemical Reaction Engineering 1 (1972) 1–13.

[58] M. Muradoglu, S. Pope, D. Caughey, The hybrid method for the PDF equations of turbulent reactive flows: Consistency conditions and correction algorithms, Journal of Computational Physics 172 (2001) 841–878.

[59] D. C. Haworth, S. B. Pope, A generalized langevin model for turbulent flows, Physics of Fluids 29 (1986) 387–405.

[60] M. R., S. Pope, A particle formulation for treating differential diffusion in filtered density function methods, Journal of Computational Physics 226 (2007) 947–993.

[61] J. Boussinesq, Essai sur la thorie des eaux courantes, Mmoires prsents par divers savants l'Acadmie des Sciences 23 (1887) 1–680.

[62] P. Moin, K. Squires, W. Cabot, S. Lee, A dynamic subgridscale model for compressible turbulence and scalar transport, Physics of Fluids A 3 (1991) 2746–2757.

[63] J. Smagorinsky, General circulation experiments with the primitive equations, i. the basic experiment, General circulation experiments with the primitive equations, i. the basic experiment 91 (1963) 99–164.

[64] A. Leonard, Energy cascade in large-eddy simulations of turbulent fluid flows, Energy Cascade in Large-Eddy Simulations of Turbulent Fluid Flows 18 (1975) 237–248.

[65] C. Meneveau, T. Lund, W. Cabot, Lagrangian dynamic subgrid-scale model of turbulence, Journal of Computational Physics 319 (1996) 353–385.

[66] H. Pitsch, H. Steiner, Large-eddy simulation of a turbulent piloted methane/air diffusion flame (Sandia Flame D), Physics of Fluids 12 (10).

[67] P. Popov, H. Wang, S. Pope, Specific volume coupling and convergence properties in hybrid particle/finite volume algorithms for turbulent reactive flows, Journal of Computational Physics 294 (2015) 110–126.

[68] J. H., Error analysis and estimation for the finite volume method with applications to fluid flows, Ph.D. thesis, Imperial College, London, UK (1996).

[69] J. H. Ferziger, M. Peric (Eds.), Computational Methods for Fluid Dynamics, Springer-Verlag, Berlin, 2002.

[70] R. Issa, Solution of the implicitly discretized fluid flow equation by operator splitting, Journal of Computational Physics 62 (1986) 40–65.

[71] E. Kaasschieter, Preconditioned conjugate gradients for solving singular systems, Journal of Computational and Applied Mathematics 24 (1988) 265–275.

[72] M. Sheikhi, T. Drozda, P. Givi, F. Jaberi, S. Pope, Large eddy simulation of a turbulent nonpremixed piloted methane jet flame (Sandia Flame D), Proceedings of the Combustion Institute 30 (2005) 549–556.

[73] R. Cao, S. B. Pope, Numerical integration of stochastic differential equations: Weak second-order mid-point scheme for application in the composition PDF method, Journal of Computational Physics 184 (2003) 194–212.

[74] S. Viswanathan, H. Wang, S. Pope, Numerical implementation of mixing and molecular transport in LES/PDF studies of turbulent reacting flows, Journal of Computational Physics 230 (2011) 6916–6957.

[75] H. Wang, P. Popov, S. Pope, Weak second order splitting schemes for Lagrangian Monte Carlo particle methods for the composition PDF/FDF transport equations, Journal of Computational Physics 229 (2010) 1852–1878.

[76] E. Kloeden, P., E. Platen (Eds.), Numerical Solution of Stochastic Differential Equations, Springer-Verlag, Berlin, 1992.

[77] E. Platen, On weak implicit and predictor-corrector methods, Mathematics and Computers in Simulation 38 (1995) 69–76.

[78] A. Tocino, J. Vigo-Aguiar, Weak second order conditions for stochastic runge–kutta methods, SIAM Journal on Scientific Computing 24(2) (2002) 507–523.

[79] G. B. Macpherson, N. Nordin, H. G. Weller, Particle tracking in unstructured, arbitrary polyhedral meshes for use in CFD and molecular dynamics, Communications in Numerical Methods in Engineering 25 (2008) 263–273.

[80] T. D. Dreeben, S. B. Pope, Nonparametric estimation of mean fields with application to particle probability density function model for turbulent flows, Tech. rep., Sibley School of Mechanical and Aerospace Engineering, Cornell University, Ithaca New York (1992).

[81] R. McDermott, S. B. Pope, The parabolic edge reconstruction method (PERM) for lagrangian particle advection, Journal of Computational Physics 227 (2008) 5447–5491.

[82] P. Jenny, S. B. Pope, M. Muradoglu, D. A. Caughey, A hybrid algorithm for the joint pdf equation for turbulent reactive flows, Journal of Computational Physics 166 (2001) 281–252.

[83] P. P. Popov, S. B. Pope, Implicit and explicit schemes for mass consistency preservation in hybrid particle/finite-volume algorithms for turbulent reactive flows, Journal of Computational Physics 257 (2014) 352–373.

[84] R. Barlow, J. Frank, Effects of turbulence on species mass fractions in methane/air jet flames, Proceedings of the Combustion Institute 27 (1998) 1087–1095.

[85] R. Tirunagari, M. Pettit, A. Kempf, S. Pope, On mathematical modeling of turbulent combustion, Flow, Turbulence and Combustion 98 (2017) 131–153.

[86] H. Pitsch, Flamemaster: A C++ computer program for 0D combustion and 1D laminar flame calculations, http://www.itv.rwth-aachen.de/downloads/flamemaster (1998).

[87] V. Hiremath, S. Lantz, H. Wang, S. Pope, Computationally-efficient and scalable parallel implementation of chemistry in simulations of turbulent combustion, Combustion and Flame 159 (2012) 3096–3109.

[88] D. C. Haworth, R. J. Blint, B. Cuenot, T. J. Poinsot, Numerical simulation of turbulent propane-air combustion with nonhomogeneous reactants, Combustion and Flame 121 (2000) 395–417.

[89] C. Jimenez, B. Cuenot, T. J. Poinsot, D. C. Haworth, Numerical simulation and modeling for lean stratified propane-air flames, Combustion and Flame 128 (2002) 1–21.

[90] F. Proch, M. Kempfa, Numerical analysis of the cambridge stratified flame series using artificial thickened flame les with tabulated premixed flame chemistry, Combustion and Flame 161 (2014) 2627–2646.

[91] S. Nambully, P. Domingo, V. Moureau, L. Vervisch, A filtered-laminar-flame pdf sub-grid scale closure for les of premixed turbulent flames. part i: Formalism and application to a bluff-body burner with differential diffusion, Combustion and Flame 161 (2014) 1756–1774.

[92] S. Nambully, P. Domingo, V. Moureau, L. Vervisch, A filtered-laminar-flame pdf sub-grid-scale closure for les of premixed turbulent flames: Ii. application to a stratified bluff-body burner, Combustion and Flame 161 (2014) 1775–1791.

[93] M. S. Sweeney, S. Hochgreb, M. J. Dunn, R. S. Barlow, The structure of turbulent stratified and premixed methane/air flames ii: Swirling flows, Combustion and Flame 159 (2012) 2912–2929.

[94] R. S. Barlow, M. J. Dunn, M. S. Sweeney, S. Hochgreb, Effects of preferential transport in turbulent bluff-body-stabilized lean premixed ch4/air flames, Combustion and Flame 159 (2012) 2563–2575.

VITA

Hasret Turkeri was born in Istanbul on Jule 5, 1983. He received his B.Sc. degree in Mathematical Engineering in 2007 and M.Sc. Computational Science and Engineering in 2011 from Istanbul Technical University. He received the Ph.D. in Mechanical Engineering from Koc University in 2017. His worked as Research Assistant in Istanbul Technical University from 2009 to 2011, and in Koc University from 2011 to 2017. He will continue his academic career as a post doctoral associate position with Prof. Xinyu Zhao in the Department of Mechanical Engineering at University of Connecticut, USA.